Spectroscopic diagnostics of the elemental composition of the solar corona

Natalia Zambrana Prado

université
PARIS-SACLAY

Diagnostics spectroscopiques de la composition élémentaire de la couronne solaire

Spectroscopic diagnostics of the elemental composition of the solar corona

Thèse de doctorat de l'université Paris-Saclay

École doctorale n° 572, Ondes et Matière (EDOM)
Spécialité : Physique des plasmas
Unité de recherche : Université Paris-Saclay, CNRS, Institut d'astrophysique spatiale, 91405, Orsay, France
Référent : Faculté des sciences d'Orsay

Thèse présentée et soutenue à Paris-Saclay, le 25/11/2020, par

Natalia ZAMBRANA PRADO

Composition du jury :

Karine BOCCHIALINI Pr., IAS, Université Paris-Saclay	Présidente
Lidia VAN DRIEL-GESZTELYI Pr., MSSL, University College London	Rapportrice & Examinatrice
Peter YOUNG Dr. (HDR), NASA Goddard Space Flight Center	Rapporteur & Examinateur
Maria MADJARSKA Dr., Max Planck Institute for Solar System Research	Examinatrice

Direction de la thèse :

Éric BUCHLIN Dr., IAS, Université Paris-Saclay	Directeur de thèse

Thèse de doctorat

NNT: 2020UPASP063

ACKNOWLEDGEMENTS

I apologize in advance for how corny, sappy and lengthy these next pages will be. Every step I have ever taken, every fail and every accomplishment, all my growth has come from being surrounded by wonderful people. It is not often that one gets the chance to pour one's feelings in a written format and I appreciate greatly this incredible opportunity to show my gratefulness.

Je veux tout d'abord remercier infiniment mon directeur de thèse. Éric, merci tellement pour tout ! Ces trois dernières années ont été incroyables. Tu m'as appris tellement de choses mais tu m'as aussi laissée grandir. Tu as toujours été là quand j'avais des questions, même si c'était trois fois la même, tu as enduré dès le jour zéro toutes les galères administratives avec moi et tu as toujours été patient et encourageant. Merci pour ta gentillesse, ta compréhension et surtout pour ton soutien car jamais je ne me suis sentie abandonnée. Je ne regrette aucune seconde passée pendant cette thèse et c'est en grande partie grâce à toi.

I would then like to thank my jury for agreeing to review my work. Lidia and Peter, thank you for the time and care you took reading my manuscript, for your comments, your questions, your insight, it was all so helpful and will make improve my work moving forward. Maria, thank you for your insightful questions and your kind words of encouragement. Karine, merci d'avoir accepté de faire partie de mon jury, c'était un honneur pour moi. Merci de m'avoir fait découvrir l'USBY gym, ça a fait partie intégrante de mon succès. Merci aussi d'avoir été une inspiration, j'ai beaucoup de respect et d'admiration pour toi.

I would also like to thank all the people I had the chance to exchange with and that I collaborated with. In particular, I would like to thank Susanna Parenti. Si cette thèse a pris le chemin qu'elle a pris c'est grâce à toi. Merci pour nos dicussions, merci pour tes encouragements et merci pour ta gentillesse. J'ai tellement appris en travaillant sur le projet ISSI. I would also like to thank all the participants of the ISSI team who helped me understand so much about solar physics in general, our discussions made me grow and learn and being a part of this team effort made me a better scientist. My thanks to Hardi Peter as well who invited me to work at MPS for a few very enriching weeks, back when going places was still a thing.

Merci à l'équipe Solaire et Stellaire avec qui ça a été un bonheur total de passer ces trois dernières années, je n'aurais pas pu demander mieux comme environnement. Tout va me manquer de vous et je ne garde que de bons souvenirs du temps passé au quatrième étage de ce merveilleux laboratoire. Merci Charlie, Fred M., Jacques, Jacques, Jean-Claude et Thierry. Merci Joao non seulement pour m'avoir accueillie dans l'équipe enseignante de Phys 292 avec Fred P., c'était une superbe expérience, mais aussi pour avoir intégré l'équipe des bleus avec moi; merci Fred A. pour avoir été encourageant et pour m'avoir fait suffisamment confiance pour que je vienne faire de la vulga dans la classe de Nicolas; merci Fred B. pour m'avoir incluse dans les séances d'astro-œnologie mais aussi pour les expériences que j'ai eues avec le SAS, la vulga m'a donné un répit nécessaire et surtout m'aide à trouver du sens dans notre métier; merci Patrick pour ta bonne humeur et ta gentillesse, c'était super d'être ta voisine de bureau et merci pour nous avoir fait confiance pour redesigner une salle entière; merci John pour être aussi gentil et pour me demander toujours si ça boom, ça rendait toujours mes journées meilleures; et merci Miho, non seulement pour le yoga et nos aventures à Tokyo, mais aussi pour toujours m'apporter un sourire, tu es géniale.

Merci Florian et Barbara pour votre amitié et pour toutes les pauses café/thé passées ensemble. Merci Barbara pour notre temps (même s'il a été un peu court) à la comédie musicale et pour avoir une si belle âme. Merci Flo pour avoir fait des manœuvres de malade avec un énorme camion et d'avoir comploté avec Louis et m'avoir fait le meilleur cadeau d'anniversaire du monde, je me remettrais jamais. Louis, merci d'avoir partagé le bureau avec moi ces trois années. J'ai tellement de chance de t'avoir rencontré au Magistère et de maintenant après tout ce temps être ton amie. Merci pour toutes les plantes qu'on a fait pousser ensemble. Merci de m'avoir aidée avec mes galères de python et pour tous les rires qu'on a partagés. Mais surtout merci de m'avoir écoutée et d'être venu à mon secours quand je me battais contre mon propre cerveau. Gabriel, je n'ai pas de mots pour te dire à quel point je suis heureuse de t'avoir dans ma vie. Notre temps ensemble au labo n'a fait que renforcer notre lien d'amitié. Merci pour les petites et grandes aventures qu'on a vécu ensemble mais plus encore pour les petits moments du quotidien qu'on a partagés, pour toutes nos dicussions, pour toutes les fois où on est parti en perdant nos ceintures pour aller chercher à manger, pour nos longs appels une fois que tu étais en Belgique et pour continûment m'apprendre des choses. Tout simplement, je t'adore.

Merci aux personnes qui font de l'IAS un si bel endroit où travailler. Merci à l'équipe administrative, en particulier merci Véronique, Patricia et Laurence. Merci aussi aux informaticiens. Merci aux collègues des autres équipes avec qui j'ai partagé de belles discussions, surtout autour des pots de thèse, certes. Merci Émilie pour avoir fait le suivi de ma thèse tout le long. Merci Alain, enseigner a été une expérience super

enrichissante pour moi et tu as toujours été très à l'écoute et très bienveillant. Merci aux thésards de l'IAS sans qui ces années n'auraient pas du tout été aussi agréables. Merci en particulier à Aurélien et Thibaut, fellow alcoriens; à Édouard, surtout pour savoir donner de supers câlins et pour être dans ma vie depuis la L3; à Louis L. avec qui c'est toujours un plaisir de discuter; à Dany qui est une si belle personne, une si belle amie y que me permite hablar en español cuando más lo necesito, gracias bella; et à Pierre qui est si important, non seulement pour moi mais pour tant de personnes que tu as aidé et inspiré, tu as toujours été là avec le bon conseil et un enthousiasme incomparable, merci pour notre temps passé à ALCOR, merci de m'avoir invitée à assister à la plus belle journée de ta vie, vous étiez si beaux, et merci pour ton amitié, elle compte énormément pour moi.

I would like next to thank the rest of the people who have willingly given me a place in their lifes, otherwise known as friends.

Primero quisiera agradecer a las personas que conocí en el Franco. Fueron catorce años de mi vida que pasé en ese colegio, ahí aprendí a amar el fútbol, el rugby, el canto y sobre todo la astronomía (gracias William, Marie-Paule y Olivier por haber fundado el club y haberme dado la oportunidad de dar mi primera conferencia a los 16 años). Estoy infinitamente agradecida de allí haber conocido a mi Ghis con quien espero cruzarme pronto y a quien agradezco haber sido tan amable con Gaylor; gracias a mis sueltos Wicho, Robi y gracias Robi por habernos hecho conocer a Dani B., jamás olvidaré todas las risas, las locuras y sobre todo los secuestros; gracias Dani G. por todas nuestras charlas pero sobre todo por seguir en mi vida y venir a visitarnos a las parisinas; gracias Niky por haber sido la sargento y por habernos cruzado después de tantos años y saber que el cariño y la amistad siguen ahí, más fuertes que nunca; gracias Fafa, eres mi familia, lo sabes, estoy tan orgullosa de ti y me encanta verte crecer y lograr siempre más cosas, seguir tu sueño, gracias por Praga y gracias a tu familia por siempre haberme acogido; gracias a mi otra mitad, Caro querida, no hay palabras para expresar lo que tú significas para mí, nadie tiene el largo adecuado como tú, nadie me hacer leerle filosofía mientras la tatúan como tú, pero sobre todo nadie tiene un pedazo de mi corazón de por vida como tú, nunca nos hemos alejado a pesar de la distancia y siempre estaré ahí cuando me necesites.

J'aimerais adresser un merci aussi à la ville de Clermont-Ferrand qui m'a accueillie les deux premières années de cette aventure en France. Là bas j'ai eu le privilège de rencontrer Sarah et Anaïs avec qui je suis ravie d'avoir gardé contact; Maëlle qui non seulement m'a invitée passer mon premier noël en France avec sa famille mais que je continue à avoir dans ma vie; Loïc avec qui j'adore avoir pleuré en regardant le tombeau des lucioles et d'avoir parlé pendant des heures et des heures de tout et de

rien, merci d'avoir toujours gardé une place dans ta vie pour moi; Nadège qui est une lumière dans ma vie, merci à toi et à ta famille de m'avoir accueillie tant de fois, je suis incroyablement reconnaissante envers l'univers de t'avoir mise dans mon chemin, merci de partager ta musique et ton art avec le monde et d'être une des personnes les plus fortes et les plus courageuses que je connais, tu es toujours dans mon coeur.

Je veux remercier les villes d'Orsay, Antony et Massy où j'ai passé la plupart des six dernières années et qui ont mis dans mon chemin des gens merveilleux. Merci Marta, Mario, Julie, Francis, Louise, Émeline et Éric. Merci aussi au M2 astro sans quoi je ne verrais pas Jordan et Raphaël une fois par an et je n'aurais pas rencontré Daniel. Merci Tess, Arnaud et Dimitri avec qui j'ai eu l'honneur de partager mon adresse pendant une super année. Merci Fabrice et MC qui ont amené au monde le plus beau des Gabriels. Merci Clémence pour être une aussi belle personne et savoir à quel point j'adore les bêtises. Merci Julien pour représenter la Bolivie avec moi et pour toutes nos discussions, avec ou sans singani à la main. Merci Manon, tu as su comme par télépathie que nous allions au même endroit dans le RER B et je sais maintenant à quel point c'était une chance de t'avoir rencontrée si tôt dans cette aventure, merci d'avoir fait des TPs, des rituels payens, de la cuisine végane et mille autres choses avec moi, j'aime le poivre toujours autant. Merci Lucas, ta présence m'apporte toujours un sourire, ton amitié compte énormément pour moi et je suis tellement heureuse de te voir heureux, au passage merci Caro, ça fait pas si longtemps qu'on se connaît et pourtant je me sens si proche de toi, merci d'être autant à l'écoute et j'espère que nous aurons plein de bouts de chemin à faire ensemble. Merci Loïc pour toutes nos siestes, nos dîners, même ceux qui étaient infernaux, mais surtout de ne pas avoir fui quand je t'ai dit que j'étais bizarre la première fois que tu m'as vue, ça valait la peine d'endurer la vie à la pacat puisque c'est là qu'est née notre amitié. I would also like to thank Henrik, I'm so glad we met in Spain, thank you for our adventures in Tokyo, and for keeping in touch, it means a lot.

Aprovecho ahora para agradecer a mi hermosa familia, la que me escogió como la que no. Gracias desde el fondo de mi corazón porque mis logros son sus logros y sin ustedes yo no sería quien soy. Gracias Silvia y Clau por su hermandad para con mi mami y por todos los pies de limón y los chocolates que hicimos. Gracias a los bros por ser tan bello grupo de tíos y tías y por haber tenido tantos hijos e hijas tan hermosos e inteligentes, gracias por todas las parrilladas, las guitarreadas, los viajes y las navidades, gracias por quererme tanto y por su apoyo incondicional. Gracias tío Tachi, tío Maco, tía Bea y Clau, su cariño me llena el corazón. Gracias tío Enrique y gracias tía Ceci y tío Javier, los amo infinitamente. Gracias a mi querida Vity que es una fuerza de energía positiva en el mundo, te pienso y me acuerdo instantáneamente de cuan importante es sonreír y ser una buena persona, me inspiras. Gracias Mich Y

Nikki por haber crecido conmigo a pesar de la distancia, son mis hermanitas y estoy muy orgullosa de las mujeres que son. Cuando éramos niñas, lo que esperaba con más ansias era que ustedes vengan a visitarnos y eso nunca va a cambiar. Las amo y las extraño. Un gracias muy especial a mis abus queridas que son una luz infinita, son las personas más amorosas que conozco y me siento súper orgullosa de ser su nieta. Ustedes tienen unos corazones inmensos, jamás me cansaré de abrazarlas y de decirles cuanto las quiero. A pesar de que ya no estén con nosotros, quiero agradecer a mi tía Chichi que siempre fue tan cariñosa y quiero agradecer a mis abuelos Papico y Enrique, su hijita lo logró y sé que hubieran estado felices por mí. Gracias Rodri y Ale, hermanos queridos son ustedes mis compañeros, los amo y los adoro, estoy tan orgullosa de ustedes y nada me hace más feliz que ser su hermana y gracias Julie por hacer feliz a mi hermanito y por haber estado presente el día de mi defensa. Jamás podré agradecer suficientemente a mis padres. Ma y Pa, espero que sepan que yo he hecho este camino porque ustedes me han dado la libertad de creer en mí, la fuerza de perseverar siempre y el apoyo para saber como mejorar y volverme a levantar cuando fallo. Donde sea que voy, ustedes están conmigo y a pesar de que estar lejos es a veces muy difícil, jamás dejo de sentir su presencia. Gracias por haber sido un ejemplo, por amarnos tanto a nosotros tres y por haberme abierto tantas puertas desde el principio. Gracias por sus consejos, por escucharme cuando necesito hablar y por no dejarme cargar mi maleta cuando aterrizo. Agradezco infinitamente al universo por ser su hija.

Je veux enfin remercier Gaylor. Ta famille m'a si chaleureusement acceuillie, merci à tes parents et à tes sœurs. Merci de m'avoir fait découvrir Bagneux, Toulouse, Moulins et Grenoble. Le trajet a été long et parfois le terrain très accidenté. Chaque fois que j'ai eu peur, chaque fois que je ne sentais pas être assez, pas être à la hauteur, tu m'as fait respirer, tu m'as rassurée et tu m'as montré que je pouvais le faire. J'ai failli abandonner mille fois, et mille fois tu m'as aidé à me reconstruire. Tu ne m'as jamais laissée tomber et tu t'es toujours battu pour moi, souvent contre moi d'ailleurs. Et tu avais raison. Je veux que tu saches que sans ton support je ne serais pas arrivée aussi loin. J'ai plein d'autres choses pour lesquelles je veux te remercier mais je crois que j'ai perdu ma chaussure.

ABSTRACT

Linking solar activity on the surface and in the corona to the inner heliosphere is one of the main goals of Solar Orbiter. Its unique combination of in-situ and remote sensing instruments can be used to shed light on this difficult task by, e.g., determining the source region of the solar wind measured in-situ at the spacecraft position. A key element in this are data on the elemental composition. Indeed, different structures on the Sun have different abundances as a consequence of the FIP (First Ionization Potential) effect. Comparing in-situ and remote sensing composition data, coupled with modeling, will allow us to trace back the source of heliospheric plasma.

During my thesis, I developed a new method for measuring relative abundances of the solar corona using UV spectroscopy, the Linear Combination Ratio (LCR) method. This method can be telemetry efficient while remaining reliable; it is based on optimized linear combinations of spectral lines. This method has been tested on synthetic spectra and on spectroscopic observation data. Using a Bayesian approach, I then developed a way to determine the uncertainties related to the measurements obtained with the LCR method.

One of the applications of the method was to provide reliable measurements of elemental composition in the framework of a collaboration whose goal is to find the characteristics of the plasma and the source region of a jet, a jet whose propagation in the corona and in the heliospheric medium will then be modeled to determine its composition in situ and whether it has reached 1 AU.

All the methods and tools necessary for the thesis work have been developed with the Solar Orbiter mission (launched in February 2020) in mind. I have modeled the noise that we will obtain in the SPICE observations and I have provided three sets of spectral lines that could in principle be used to make composition measurements and that will be used to design optimal SPICE studies for abundance maps.

RÉSUMÉ

Un des objectifs principaux de la mission Solar Orbiter est d'établir un lien entre l'activité à la surface du Soleil et l'évolution de la couronne et de l'héliosphère interne. Le satellite emporte à cette fin une combinaison unique d'instruments permettant de faire tant des mesures in situ du plasma héliosphérique que des observations à distance du Soleil. Ces mesures nous permettront par exemple de déterminer la région source du vent solaire mesuré in-situ au niveau du satellite. Un outil essentiel pour établir un tel lien sont les mesures de composition. En effet, différentes structures solaires sont caractérisées par des abondances d'éléments chimiques différentes, en raison de l'effet FIP (premier potentient d'ionisation). Comparer les mesures de composition in situ et à distance, en lien avec la modélisation de l'effet FIP, nous permettra de déterminer les sources du plasma héliosphérique.

Lors de la thèse, j'ai développé une nouvelle méthode de mesure d'abondances relatives de la couronne solaire grâce à la spectroscopie UV, la Linear Combination Ratio (LCR) method. Cette méthode peut être peu coûteuse en télémétrie tout en restant fiable ; elle se base sur des combinaisons linéaires optimisées de raies spectrales. Cette méthode a été testée sur des spectres synthétiques et sur des données d'observations spectroscopiques. Grâce à une approche bayésienne, j'ai ensuite développé une manière de déterminer les incertitudes liées aux mesures obtenues avec la méthode LCR.

Une des applications de la méthode fut de fournir des mesures de composition élémentaire fiables dans le cadre d'une collaboration dont le but est de trouver les caractéristiques du plasma et la région source d'un jet. La propagation dans la couronne et dans le milieu héliosphérique du jet a été ensuite modélisée pour déterminer sa composition in situ et s'il a atteint 1 UA.

L'ensemble des méthodes et des outils nécessaires au travail de la thèse ont été développés avec la mission Solar Orbiter (lancée en février 2020) en tête. J'ai modélisé le bruit que nous obtiendrons dans les observations de SPICE et j'ai fourni trois ensembles de raies spectrales qui pourront être utilisés pour faire des mesures de composition. Ces trois ensembles seront utilisés pour concevoir des observations optimales de SPICE pour la production de cartes d'abondance coronales.

CONTENTS

LIST OF FIGURES

LIST OF TABLES

1

INTRODUCTION

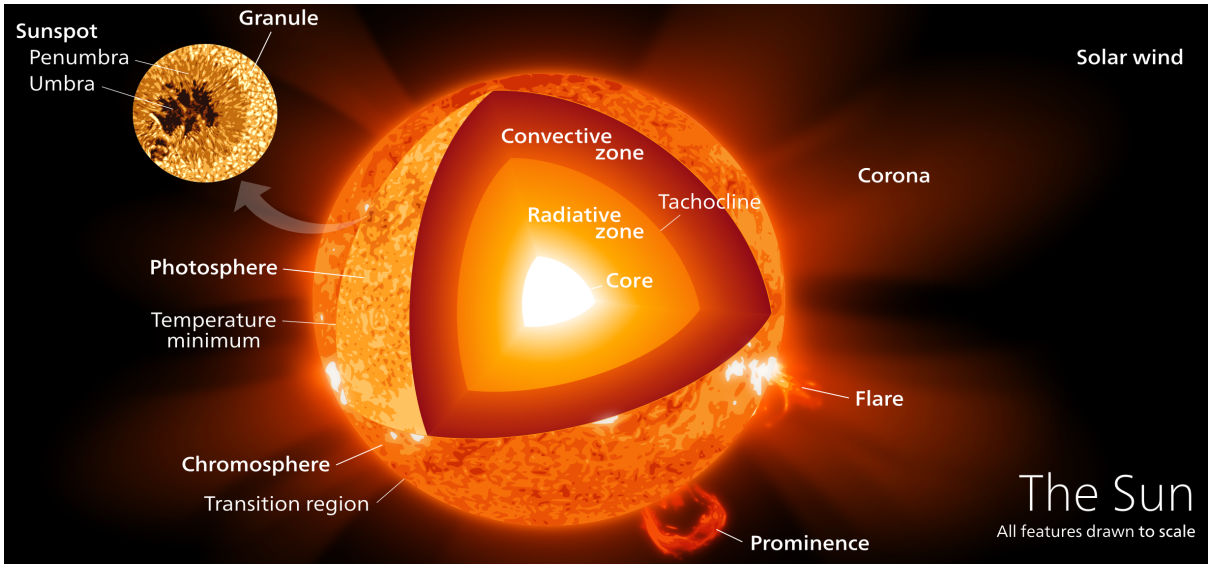

Figure 1.1: Scheme to scale of the different inner layers of the Sun and its 4-layered atmosphere. Source: Kelvin Ma, Wikimedia Commons, licence CC BY-SA 3.0.

1.1 AN UNEXPECTED JOURNEY

A single photon's adventure of a life-time starts at the center of our star. She is born at the Sun's core. This is the first internal layer of the Sun which encompasses around 25 percent of its radius ($R_\odot$). Here, because the pressure is so high, hydrogen atoms will come together. This process is called nuclear fusion and it is the Sun's fuel. Four protons will become a Helium-4 nucleus and in the process give birth to our photon. She will spend anywhere from a few thousand to a few hundreds of thousands of years randomly walking [Mitalas and Sills, 1992], being reabsorbed and re-emitted by the extremely hot plasma of the core first and the radiative zone next. This second layer of the Sun extends from 0.25 $R_\odot$ to 0.7 $R_\odot$. Carrying her energy with every step, colliding every few millimeters and more often than not changing directions, she makes her way to the convective zone. Density and temperature drop, it doesn't feel

so crowded anymore. The convective zone, composing only 0.3 $R_\odot$, is a completely new environment for her. She feels the convection currents carrying ions and atoms from the top of the radiative zone upwards and transporting cold plasma downwards from higher up. She is able to move more and more freely. She encounters fewer particles and her steps get longer and longer, it only takes her a few days to travel to the surface of the Sun.

She realizes she's reached the surface, the photosphere, as the medium has become pretty much transparent. The surrounding plasma has become suddenly optically thin and she's no longer being constantly forced to switch paths to avoid cumbersome ions. She can finally escape towards the interplanetary medium as fast as she wants. She doesn't do so without first inspecting the star she has now freed herself from. She notices that the photosphere is a 400 km thick layer at 6 000K. This is what we, humans, see when we look at the Sun with our eyes. She sees dark spots on the surface, sunspots. Inside these huge structures that can last for more than a month, the plasma lies lower, is cooler and the intensity of the magnetic field is several orders of magnitude higher than anywhere else at the solar surface. It is an amazing spectacle and the first look humans had into solar activity and how it changes through time. Looking more closely at the quieter and more uniform areas, she notices that the surface is not so smooth after all. She recognizes how the convection cells underneath shape the surface into a pattern of bright granules where material is rising up delimited by dark narrow lanes of sinking plasma.

Traveling a little bit further, she reaches the chromosphere, which feels a little bit cooler, at least at first. The chromosphere is about 5 times thicker than the layer right below it. Here, she distinguishes a number of new structures. Above the sunspots that appear dark in visible light as well as in radio and infrared observations, the plasma shines bright in ultraviolet light. Quite similarly to the granules observed below, she distinguishes brighter cells surrounded by darker regions. At this height, the entire Sun seems to be covered in fiery grass, these short-lived jets are called spicules. As our photon continues to make her way upwards, she feels the temperature starting to go up again and then a sudden drop in density and jump in temperature whilst traversing a very thin layer of the solar atmosphere, the transition region.

She has now reached the uppermost layer of the Sun's atmospheric envelope, the corona. The sunspot, which we will call an active region (AR), looks completely different from up here, specially in ultra-violet (UV) and X-ray light. It shines very bright and has a very complicated magnetic configuration. The striking curved

structures coming out of it catch her attention. These coronal loops appear as arcs that have their feet rooted in the sunspot and rise higher and higher. She realizes that the ions and the magnetic field have switched roles. In the solar interior, magnetic field lines where curved and pushed around by the plasma flows. Here, in the external layers of the solar atmosphere, the magnetic field lines form a path around which charged particles will gyrate, the magnetic field now leads the way. She notices a cold snake-like structure of cold plasma sitting quietly above a hotter structure, we call them prominences or filaments. A little bit further, another one of these filaments detaches and causes a very energetic eruption.

Above the ensembles of loops forming ARs overlies a large cap-like structure with a pointy end. This is called a helmet streamer. Looking around she sees two darker areas, one at each pole. These are the polar coronal holes (CH) where the magnetic field lines are open and plasma is not confined as in the loops. She sees another smaller, much thinner CH lying at the boundary of the AR she was just looking at. Finally, she arrives to the top of the corona and prepares for interplanetary travel.

She notices that bunches of ions and electrons are transported around her, in the same way as water flows in currents. It is the solar wind (SW), particles escaping from the corona and filling the entire solar system, from Mercury to the very edge of our solar system. This humongous bubble that the Sun continuously loads with this stream is the heliosphere. She cannot wait to get to the very edges of it.

As she continues her way, she wonders, is everything I have witnessed linked? Is this what the Sun looks like always? How different would it have appeared if I had left the interior earlier in the decade, or later? How does the sun create and control the heliosphere and how does solar activity change with time?

As the environment around her thins out and as she leaves the Sun behind, she sees a pale blue dot in the distance. It seems to get bigger and bigger. Suddenly, everything comes to a halt. Fade to black. Our photon has inadvertently hit the heat shield of Solar Orbiter and been absorbed.

1.2 OUR NEIGHBOUR INTI [1]

The Sun has a very complex structure: as our dear photon has shown us, it is a dynamic star and many things can be happening at once from the core to the top layer of its atmosphere. Unfortunately, she disappeared not knowing that she had crashed precisely on a spacecraft whose sole purpose is to bring some answers to

[1] name of the ancient inca sun god

her many questions. Linking solar activity on the surface and in the corona to the inner heliosphere is one of Solar Orbiter's main goals. Solar Orbiter will, for example, provide elemental composition data. As we will see, these data can allow us to trace back the source region of the SW. But let us not get too ahead of ourselves. In this introductory chapter we will rewind a little bit and talk about the solar corona, the solar wind and how we can link them.

1.2.1 *The Solar Corona*

The Corona is the external layer of the Sun's atmosphere. Fig. 1.2 shows a composite image of the Corona acquired by the Atmospheric Imaging Assembly (AIA; Lemen et al. [2012]) instrument on board the Solar Dynamic Observatory (SDO; Pesnell et al. [2012]).

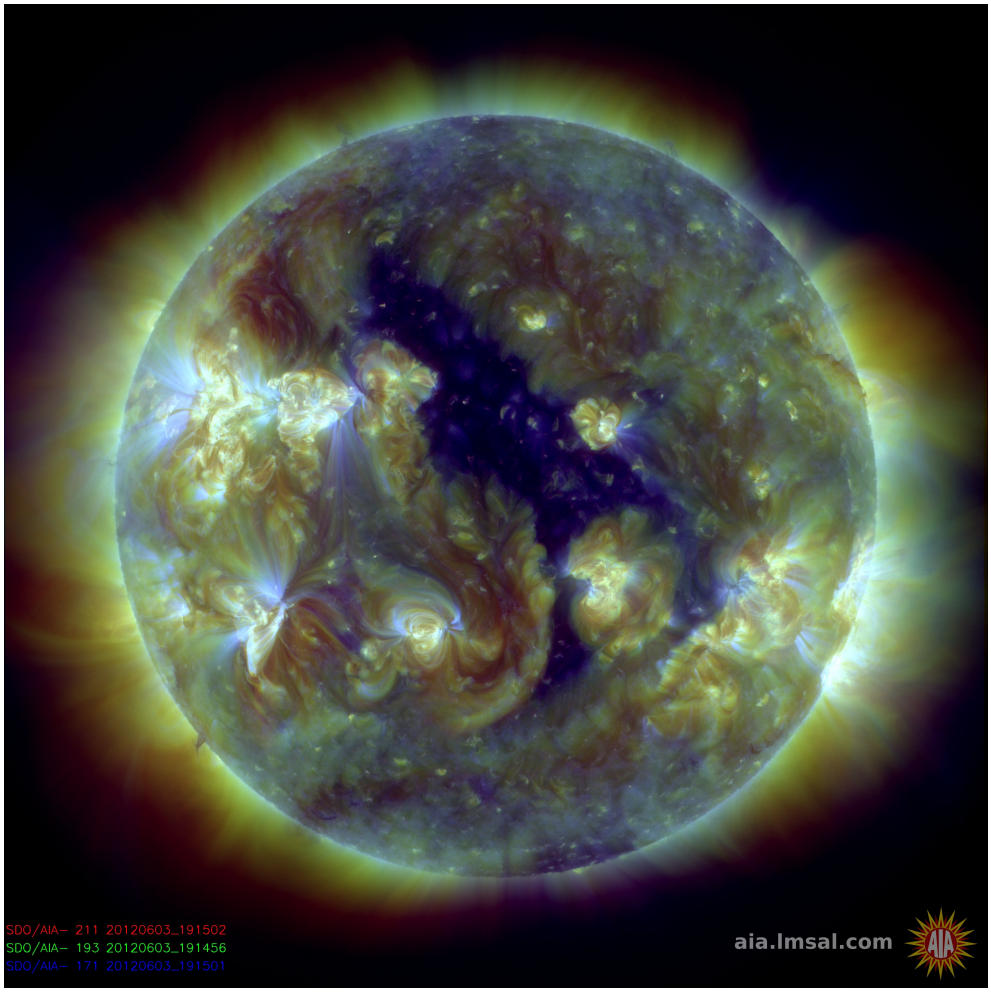

Figure 1.2: Composite image of observations of the Solar Corona made on June 3rd 2012 using the 211 Å, 193 Å and 171 Å channels of the AIA instrument aboard SDO.

These images have been taken in extreme UV (EUV) light. The ions emitting these EUV lines are strongly ionized, for example, AIA's 193 Å channel contains emission lines of the ion Fe XII, iron ionized 11 times, and even higher. In order for iron to lose these many electrons, the corona has to be at extremely high temperatures of the order of 10^6 to 10^7 K. The first astrophysicist that understood that coronal plasma reached such temperatures was B. Edlén in 1943 [Edlén, 1943, Swings, 1943]. The detection of spectral lines of highly ionized atoms in EUV and X-rays challenged the scientific community.

The corona is a low density, almost fully ionized hot plasma. Contrary to what we would expect from the laws of thermodynamics, the corona is hotter than the surface of the Sun. Getting further away from the core of the Sun, instead of decreasing constantly, the temperature increases. Fig. 1.3 shows the evolution of density and temperature as a function of height above the surface.

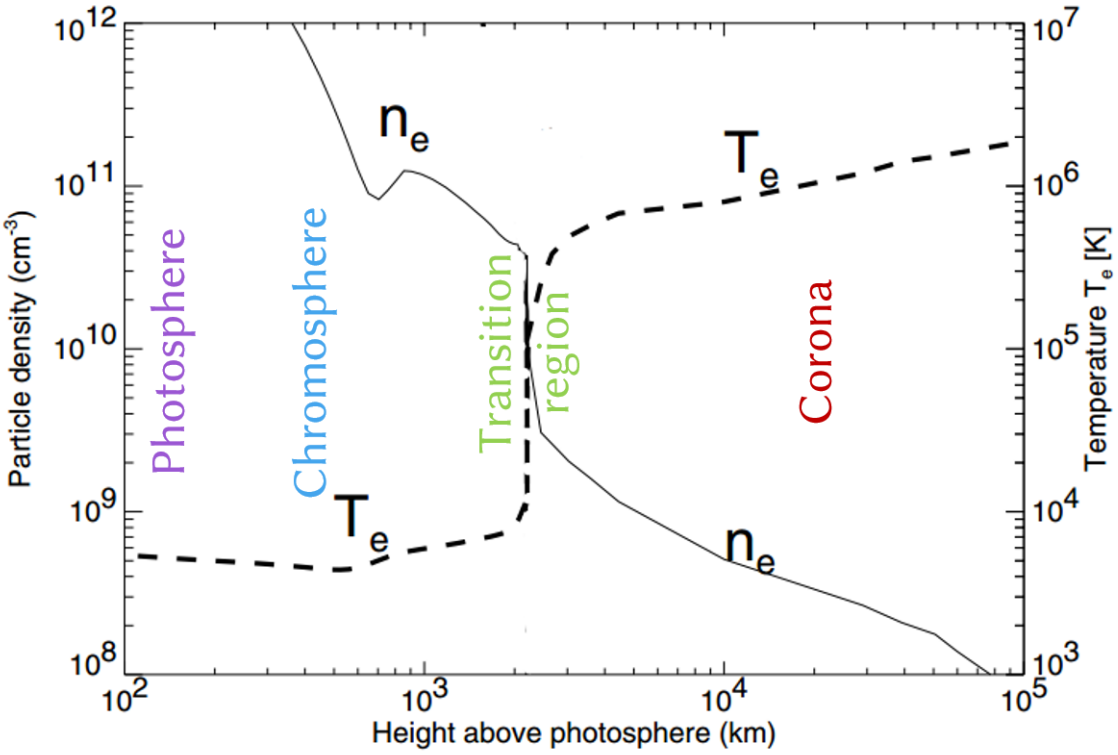

Figure 1.3: Evolution of the temperature and the density in the solar atmosphere with height, adapted from Aschwanden [2004].

As we get further from the photosphere, the temperature decreases until it reaches a minimum of 4 400 K at 800 km from the surface. It then increases to 20 000 K at roughly 2 000 km into the chromosphere. Simultaneously, the density is decreasing. When we reach the transition region, the temperature and density gradients increase suddenly. We reach 10^6 K after a two order of magnitude increase and, similarly,

we lose two orders of magnitude in density. This is surprising and counter-intuitive. If we only take into account thermal transfer processes, radiative and conductive losses would cool down the corona, it wouldn't be able to stay at 1 000 000 K. We need additional physical mechanisms to bring in energy to the corona in order to heat it so it constantly remains at these temperatures.

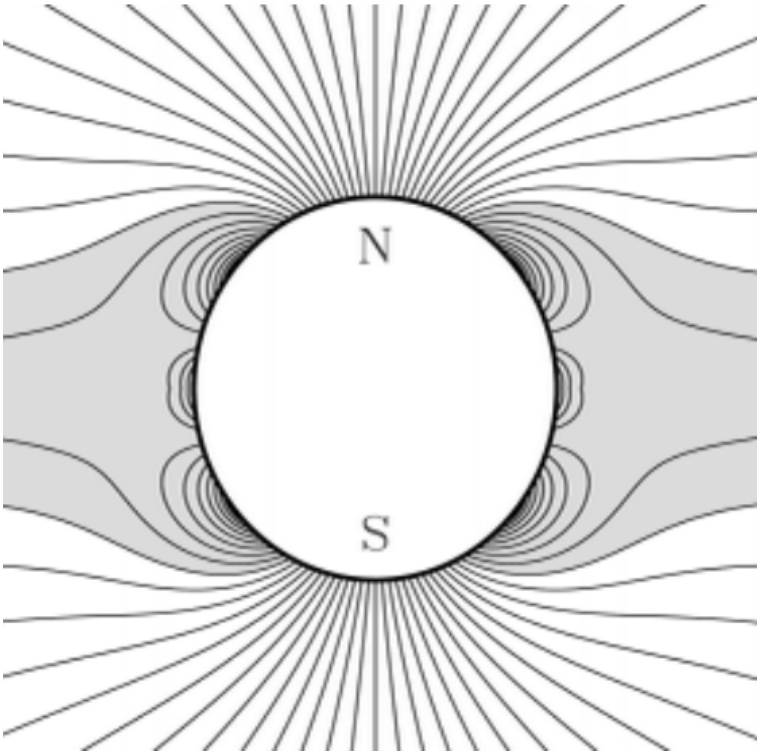

Figure 1.4: Depiction of the magnetic field lines of the solar atmosphere using the semi-empirical model of Banaszkiewicz et al. [1998], [Aschwanden, 2004].

The dynamics of the solar corona depend strongly on the Sun's magnetic field. We can see a simple scheme of the its configuration in Fig. 1.4 during solar minimum conditions. We can distinguish two general types of magnetic structures:

- **Closed magnetic field:** The grey area encloses a region where the magnetic field lines are locked in a loop-like configuration.
- **Open magnetic field:** The remaining white area corresponds to the regions where the magnetic field lines are open towards the heliosphere. In this kind of regions, temperature and density are lower than in the previously described regions. These are the north and south polar coronal holes.

During the less active years, the Sun will rarely show a blemish on its surface. Its magnetic field can then be approximated by an azimuthal current sheet in the equatorial plane and an axisymmetric field encompassing both a dipole and a quadrupole components [Banaszkiewicz et al., 1998]. The topological configuration of the solar

magnetic field is however not always as neat as this simple analytic model. Magnetic activity will vary during the 11 year solar cycle. In the more active years however this simple configuration dishevels. Within the closed field region, within the so-called activity belt, ARs emerge and start breaking apart the neatness of solar minimums. They are rooted in the photosphere and can reach heights of several thousands of kilometers. As shown in Fig. 1.2, many magnetic structures can develop. We can observe different bright ARs which are the white-yellowish areas. We also see an equatorial coronal hole which is the big purple structure in the middle of the image. We can also see other structures such as various coronal loops. All of these structures are tightly linked to magnetic field. The ARs, as we have seen throughout our photon's journey, lie above sunspots which are areas with a strong concentration of magnetic field. These ARs are a closed magnetic structure. Coronal loops are arches structured by closed magnetic flux tubes. Their feet are anchored at the solar surface and the plasma that we see shine in EUV light is trapped within them. Coronal holes are open magnetic structures. Coronal plasma can escape by following the magnetic field lines of these structures thus filling the heliosphere with the solar wind (SW). The SW is usually described as having two speeds, we have fast solar wind and slow solar wind. Whereas it is certain that the fast SW originates at the polar coronal holes, the origin of the slow SW remains an unanswered question in solar physics. The upcoming section describes its different possible source regions.

1.2.2 *The slow wind rises*

Charged particles continuously stream from the Sun to the outskirts of our solar system. Protons, electrons α particles, as well as a small fraction of heavy ions compose the so called solar wind. At the beginning of their interplanetary journey, the solar wind ions will pass through the corona where the density will decrease. These ions will follow the open field lines that span throughout the heliosphere. These flows are dynamic and will have different properties at different times in the solar cycle. Much like in the corona, where the SW originates, they can be highly structured and dynamic. Schwenn [2006] divides the SW in four different categories. We will start by describing the first two basic streams. It has been established for a number of decades now that, during solar minimum, two components of this wind can be clearly identified a fast-speed wind and a slow-speed one [McComas et al., 1998]. The faster streams originate from coronal holes [Hassler et al., 1999], its characteristics do not vary much from stream to stream meaning that its final speed, density and helium content for example are stable. By grouping the solar wind from multiple solar wind streams over a range of time periods, we can derive additional general properties for

both winds and determine what differentiates them [Abbo et al., 2016]. The slow wind has higher proton density, lower proton temperature, higher electron temperature, larger temporal variability, higher heavy ion ionization states, and, an enhancement in the abundance of low first ionization potential (FIP) elements.

A clear separation between both winds and where they might come from is not evident throughout the solar cycle. When the Sun is more active, a third type of wind would be a slow-speed wind that emerges from active regions that emerge in the activity belt. This wind can bear signatures more commonly related to the fast wind. Zhao et al. [2009] and D'Amicis and Bruno [2015] found such indicators through in situ measurements. This type of wind has a much higher helium abundance than the slow SW during solar minimum. Thus, clearly speed is not the only indicator for the origin of solar wind. As a fourth type of wind, Schwenn [2006] considers the plasma that are ejected during a coronal mass ejection (CME).

When trying to understand which are the main slow-speed SW sources and their formation mechanisms, they are often classified in three different scenarios (e.g. Abbo et al. [2016]):

- Slow SW escapes through open magnetic field regions, just as the fast SW, but in areas with a higher field line curvature and/or a larger expansion factor. In this case, the wind plasma that our spacecrafts would could sample should carry signatures of the physical processes taking place in the coronal hole it comes from.

- The second scenario involves plasma escaping thanks to interchange reconnection. Magnetic reconnection is a physical process that reconfigurates the magnetic topology of the plasma [Kopp and Pneuman, 1976]. Closed magnetic loops break and reconnect with the surrounding open field lines. The in-situ measurements in the heliosphere would thus reveal properties related to the closed-loop region the plasma comes from just outside of the coronal hole boundary.

- Finally, slow SW would be linked to events describing a sporadic and highly fluctuating emission plasma. This plasma would be released through pinching at the streamer cusp. As the magnetic field is weaker in these areas, material in the underlying closed-field regions can escape through magnetic reconnection, diffusion or thermal instabilities.

The data our community has collected so far is consistent with these three scenarios [Abbo et al., 2016], however, it does not allow us to determine how much each contributes to the bulk of the slow SW. This means that our understanding of solar winds and their sources is not complete yet. These three types of mechanisms could also all be happening simultaneously. Thus one of the questions that prompted the

work done in this thesis, and a major objective of the Solar Orbiter mission, remains: what are the source regions of the solar wind?

1.3 LINKING THE SUN TO THE HELIOSPHERE

The Sun's mass and electromagnetic emissions strongly influence a region of space that we call the heliosphere. It extends to a distance of about 100 AU. All astronomical bodies of our solar system are prisoners of its gravity and at the mercy of its mood swings. Every star's activity will shape its neighbourhood. We now know for example that low mass planets living around young stars can undergo a complete wipe out of their gaseous envelopes due to the high magnetic activity of their host stars [Poppenhaeger et al., 2020].

With the Sun being the closest star to us, it presents itself as the best candidate for in depth studies. Even though the solar environment stands as one of the most studied plasma systems, it continues to challenge us. Thanks to the fleet of instruments that different space agencies have sent into space, we have decades of in-situ and remote-sensing observations of the heliospace. These instrumental efforts combined with theory and modeling allow us to understand the physical processes involved in the various phenomena that take place in the heliosphere. The consequences that the Sun and its activity can have on our solar system are many, here we list only a few as examples:

- The Sun continuously releases magnetized plasma (the SW) and Solar Energetic Particles (SEPs) into the interplanetary medium. Combined with the electromagnetic radiation from the Sun, they can interact with the planets and their moons, particularly with their envelopes which might be neutral and/or charged fluids. The interactions between the SW and the magnetospheres of planets can eventuate in aurorae for example and it can even change the properties of a planet's magnetosphere [Griton and Pantellini, 2020].

- The solar wind fills the heliosphere and thus also interacts with the latter's outer boundaries and the local interstellar medium. Cosmic rays, relativistic particles, can be of galactic origin. These particles enter the heliosphere and can interact with the SW. Solar eruptions can enhance the magnetic field of the interplanetary medium and thus deflect galactic cosmic rays.

- In its moodier days, more energetic phenomena can take place. Sometimes, due to magnetic instabilities, filaments (or prominences) expand and erupt and a CME will take place. CMEs can have an impact on the Earth's magnetosphere. The most intense geomagnetic storms result from this phenomenon. Weaker storms

can be produced by high-speed SW. Another type of energetic events are flares which are a very sudden release of energy and appear as a short bright flashes, particularly in UV light. Often, CMEs accompany flares. Flares can produce short-term ionospheric disturbances. They can affect radio communication and navigation. SEPs are potentially hazardous to space-based technological systems and humans in space.

For decades now scientists have tried to determine which mechanisms prompt these kinds of events. One of the main goals in space weather physics is predicting these various phenomena. Knowing what physical phenomena can happen at the Sun itself, how the interstellar medium interacts with our solar system, as well as what the consequences of the phenomena listed above are in the heliosphere are all important pieces of this puzzling endeavour. Understanding how the Sun works and how its activity changes is then key. A comprehensive understanding of the solar magnetic cycle, for example, would require detailed modeling of the solar interior. This can be done through helioseismology, a review of the current advances on retrieving a 3D view of the Sun is presented in Gizon et al. [2009]. These models can help understand the solar cycle and the impact that large scale flows and the solar dynamo have on our star, but also how magnetic flux emergence connects the convective zone and the photosphere. We have to also analyse the effects our solar system has in its environment and vice-versa. McComas et al. [2009] provided an overview of the Interstellar Boundary EXplorer (IBEX) mission and some of the early results from its first all-sky maps. This mission allows us to study the interaction between the interstellar medium and the heliosphere. Through imaging, these authors found a bright ribbon of emission that was not predicted by any prior models or theories. We will describe next in a little more detail a few attempts at connecting the Sun to the heliosphere by looking at two solar phenomena and their impact on their environment.

1.3.1 *Solar storm chasers*

CMEs are sporadic events that release large quantities of matter and electromagnetic radiation into the interplanetary medium. The ejected magnetized plasma travels through the solar system and can impact the planets living within it. They are the most important cause of magnetic storms at the Earth's magnetosphere. During solar eruptions, the ejected material will travel in the interplanetary medium, often faster than the surrounding SW. This can create a shock. Through the analysis of observations coupled with in-situ data, we now have an understanding of their shapes and orientations [Janvier et al., 2014]. Linking CMEs to its consequences on Earth is not an easy task. As shown in Temmer et al. [2017], it requires the combination

of remote-sending images of the Sun (on and off-disk), tracking its temporal and spatial evolution through modeling and in-situ observations. Bocchialini et al. [2018] performed a statistical analysis of 32 magnetic storms that took place on Earth during 2002 and related them to their sources at the Sun. They found that a great majority of them were related to CMEs. Efforts to follow such chains of events require the collaboration of scientists of many different fields. After the detection of the magnetic storms at Earth, it is necessary to connect them to the process in the solar wind that originated it, whether it be an interplanetary coronal mass ejection (ICME) accompanied by a magnetic cloud (MC), an ICME without a MC, a corotating or a stream interaction region for example. This is done by characterizing, at L_1, the solar-wind structure that follows the shock associated with the magnetic storm first. Then they looked for possible events that took place at the Sun that could be linked to the phenomena measured at L_1 and thus to every magnetic storm. After identifying the structures leaving the Sun and their possible interactions through white-light and radio observations, they took the propagation of these events into consideration. This was done through a ballistic model first and then using the drag-based-model of Vršnak et al. [2013]. They then looked for signatures of acceleration processes linked to solar sources in radio emissions. Finally, in the case of magnetic clouds, they determined if the chirality of the flux rope observed at L_1 is compatible with the location of the solar source. This study provided statistics regarding the geoeffectiveness of different types of events, the role that the angle of impact of a CME can play in causing or not a magnetic storm, and a comprehensive methodology to analyse the full chain between Sun and Earth. Their analysis underlines also the importance of multi-wavelength observations and interdisciplinary efforts but also the difficulty of finding parameters that could be measured remotely that would allow an accurate forecast of the likelihood of a CME to impact Earth and how long it would take it to reach Earth as well as issues with the propagation tools used. These studies allow us to follow the chain of events from the Sun to Earth of big energetic events, what if we wanted to follow smaller structures?

1.3.2 *The FIP effect*

In order to understand the interactions between the Sun and the heliosphere and their impact on the celestial bodies living within the latter, we need to study the properties and the origin of the solar wind (SW), which shapes the heliosphere. The problem of mapping back to the Sun heliospheric plasma structures is often addressed using elemental abundances. This is because the ionic charge states and elemental abundances are largely fixed below 10 $R_\odot$. It is not the case for density and

temperature which change dynamically during the transit in the heliosphere. This means that when measuring plasma properties in-situ, the heavy ion charge state and elemental compositions are most intimately related to the properties in the SW source region [Baker et al., 2019]. Changes in abundance in a given region of the solar corona should be reflected in the plasma that escapes from it. Variations in coronal plasma abundances can be found in different types of structures such as active regions [Baker et al., 2013], jets, plumes [Guennou et al., 2015], and loops. The chemical composition of coronal plasma (the abundances of the different elements) can thus vary from structure to structure but it can also do so in time [Feldman and Widing, 2003]. As it becomes fixed at low heights in the corona, the determination of the composition of the different structures would allow us to pinpoint the source of the SW by comparing and linking remote-sensing abundance measurements to in situ analysis.

The variations in abundances are linked to the First Ionization Potential [FIP; Saba, 1995] of the different elements. Typically, in magnetically closed structures, the coronal abundances of elements that have a low FIP (< 10 eV) are enhanced in comparison to their photospheric abundances. This is not the case for elements with a higher FIP (for these elements the coronal and photospheric abundances are about the same). This anomaly is called the FIP effect [Pottasch, 1964a,b], and it can be quantified by measuring the ratio of the coronal to photospheric abundance (the abundance bias, also referred to as FIP bias as it is FIP-dependent) of different elements. These anomalies do not only occur in the corona of the Sun but also in other stellar coronas, and an 'inverse FIP effect' has even been detected in some of them [Laming, 2015].

The FIP effect is linked to a variation in the abundance of elements between the corona and the photosphere. The abundance of an element is defined as:

$$A_X^{\text{region}} = \frac{N(X)}{N(H)}, \tag{1.1}$$

where $N(X)$ is the total number density of element X and $N(H)$ the total number density of hydrogen, both measured in a certain region.

The FIP effect is quantified through the FIP bias f which is the ratio between the coronal A_X^C and the photospheric A_X^P abundance of an element:

$$f_X = \frac{A_X^C}{A_X^P}. \tag{1.2}$$

In Fig. 1.5 we can see the measurement of the FIP bias as a function of the FIP of different elements. These measurements where carried out within the solar wind. We can see an enhancement of a factor 3 to 4 for most low FIP elements.

This threshold at 10 eV corresponds to the temperature of the upper chromosphere meaning that this is where the fractionation is taking place. The FIP effect impacts

ionized elements and is mass independent. Any physical process responsible for this fractionation should account for this mass independence and result in an variation of the FIP bias. Different models have been developed in order to explain the FIP fractionation. Marsch et al. [1995] and Peter [1996] considered a fractionation which occurs beneath the base of large loops, they suggested that photoionization would be responsible of ionizing low FIP elements and separate them from the neutrals. Schwadron et al. [1999] suggests that the FIP effect takes place within AR loops, which would explain why only in slow wind we see an enhancement. Coronal ion cyclotron waves propagating down a loop would heat chromospheric ions only. This mechanism results in no fractionation in open field lines as there is a stronger imbalance between upward and downward propagating MHD waves. Geiss [1985] and Widing and Feldman [2001] suggest separation of ions and neutrals in the chromosphere and then diffusion perpendicular to the magnetic field.

More recently, Laming [2004] suggested that the FIP effect is a consequence of the ponderomotive force. The interaction between Alfvén waves that reflect on the upper layers of the chromosphere result in an acceleration of the ionized material. The ponderomotive acceleration is strong only in a small range of heights, thus thermal transport or diffusion processes have to continuously provide this small region of material to ionize. The combination of these two processes results in a change on coronal loop composition in a timescale of days, which is comparable to the observations [Widing and Feldman, 2001]. This model has the advantage of also explaining the inverse FIP effect observed in other stars and extremely rarely on the Sun. The FIP effect appears to be closely linked to the heating mechanisms [Laming, 2015, Baker et al., 2013] which is why studying it and being able to measure it accurately is important.

If we are able to determine the photospheric and the coronal abundances of an element X, we can easily evaluate the FIP bias for this element. Different methods exist to determine the photospheric abundance, this can actually be done with remarkable accuracy [Asplund et al., 2009, Caffau et al., 2011, Grevesse et al., 2015, Scott et al., 2015b,a]. We will consider in this work that photospheric abundances are well known. On the other hand, coronal abundances are much more difficult to measure accurately. Schmelz et al. [2012] show the discrepancies between different measurements of these abundances that were taken as a reference by the solar community.

Being able to measure the FIP effect by remote sensing and comparing it to the in situ abundance diagnostics of the SW [von Steiger et al., 1997] can therefore allow us to constrain the origin of the particles that arrive at a spacecraft [Brooks and Warren, 2011]. Having abundance maps produced systematically from all adequate UV observations would then help to obtain a better idea of how the solar wind is

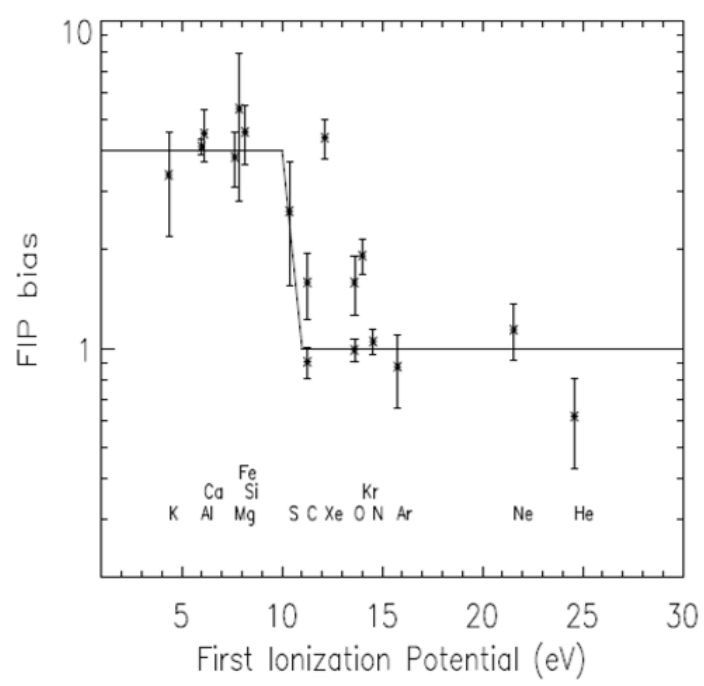

Figure 1.5: FIP bias as a function of FIP for different ions as measurured in-situ in the slow solar wind, von Steiger et al. [1997]

formed and how it unfolds in the interplanetary medium although this is evidently not enough [Stansby et al., 2020]. Accurate plasma diagnostics of the SW and the corona will need to be combined with precise modelling of the solar magnetic field and plasma flows in the interplanetary medium is crucial when trying to determine the source regions of the SW [Peleikis et al., 2017].

1.4 OUTLINE OF THE THESIS

Understanding how stars work and how they influence their environments is a crucial concern of the astrophysics community, whether it be on the quest to find habitable exoplanets or simply to protect ourselves and our technology from the occasional angry outburst. But in order to understand what the relationships between all these different phenomena are, we need to be able to have ways to link them. During my thesis, I focused particularly on developing a method to perform relative abundance spectroscopic diagnostics of the solar corona because knowing what the physical properties of the objects we are studying is crucial. They can be of great use when trying to answer some of the fundamental questions our poor photon was asking herself before meeting her demise.

In order to understand how to measure the coronal abundances and therefore the FIP effect, we first have to understand the information that the electromagnetic

radiation can give us, which Chapter 2 will tell us all about. In Chapter 3 I will present a new method, developed with the aim to provide optimal determination of the abundance biases in the corona from a spectroscopic observation, even when the DEM cannot be precisely determined. Chapter 4 provides a numerical protocol based on a statistical approach to determine the uncertainties linked to our method. In Chapter 5 we provide relative FIP bias measurements of different regions of an AR at different temperature ranges as part of the joint effort of ISSI team n.418 "Linking the Sun to the Heliosphere using Composition Data and Modelling" led by Susanna Parenti in linking remote sensing observations of an AR jet to in-situ measurements at 1 AU. In Chapter 6 we simulate the noise we will face when observing with SPICE. We suggest three sets of spectral lines to be observed with SPICE and we test them using not only the methods described previously but but also using numeric simulations results. Chapter 7 discusses the implications of the work presented in this thesis both from observational and methodological perspectives and suggests improvements and developments for future work.

2

THEORETICAL BACKGROUND OF FIP BIAS MEASUREMENTS IN THE CORONA

The Sun is a plasma ball mostly composed of hydrogen and helium but also of small amounts of other heavier elements. These elements tell a story, they give us information about the history of the solar system and about the different mechanisms that take place within the different layers of our star. It is on the information these heavier elements provide that our analysis will be based upon, more specifically, on their EUV emission.

In this chapter, we will describe the mechanisms that take part on the formation of spectral EUV lines in the corona and how we extract physical information from observing them.

2.1 THE EUV LIGHT EMITTED BY THE CORONA

Given how tenuous and hot the corona is, hydrogen and helium are completely ionized, and heavier elements are at least partially ionised. This gives rise to emission in extreme UV light and X-rays through both the continuum and emission lines. As we have mentioned in the previous chapter, we are interested in the FIP effect which, as we will see, we can probe through spectral lines. We will not concern ourselves with the continuum and we will talk solely about emission lines and the information we will retrieve from them. It is important to know however that when analyzing the solar spectrum in these wavelengths, we will have to separate the continuum from these lines.

In the solar atmosphere, atoms lose their electrons mainly through collisional ionization and auto-ionization and recombine through radiative recombination or dielectric recombination [Aschwanden, 2004]. These processes change the ion content of the solar corona at different temperatures. Electrons get excited through collisional excitation from electrons and from protons and through stimulated absorption. They decay through collisional de-excitation with electrons and protons, stimulated emission and spontaneous emission [Aschwanden, 2004]. These processes participate in populating and de-populating the excited states of atoms and ions in the corona.

In order to introduce the formalism we will use in the rest of this thesis, we will consider in this chapter the very simple case of a two level ion and we will place ourselves in the so-called coronal approximation. We do the following assumptions:

- The plasma is optically thin, photons can travel freely.
- The corona is in a stationary state and free of dust.
- The coronal plasma is in ionization equilibrium: a balance between the ionization rate from an ionization stage of an element (e.g. X^{+m}, where +m the ion's charge) with the recombination rate from the ionization stage X^{+m+1}.
- The population of excited states occurs primarily by collisional excitation by electrons from the ground state and the de-population of excited states occurs primarily by spontaneous emission.

One of the main assumptions that we make is that ionization/recombination can be decoupled from excitation/de-excitation processes. Given that excitation/de-excitation takes place in shorter time scales than ionization/recombination, this approximation is usually accurate in the solar atmosphere [Mariska, 1992].

We consider that de-excitation of an ion, and therefore emission of a EUV photon, comes purely from spontaneous emission as the radiance is low enough so stimulated emission is negligible. Under these circumstances, the radiance of an optically thin spectral line corresponding to the transition $i \rightarrow j$ in the ions X^{+m} can be written as:

$$I_{ij} = \frac{1}{4\pi} \int N(X_j^{+m}) A_{ij} h\nu_{ij} dz, \tag{2.1}$$

where ν_{ij} is the frequency, A_{ij} the Einstein coefficient for spontaneous emission, and $N(X_j^{+m})$ is the density of emitters. The integration is over the line of sight.

This equation is rather simple in comparison to what we would have obtained if coronal plasma was optically thick, or if other processes such as stimulated emission were major contributors to the line formation. Nonetheless, $N(X_j^{+m})$ can't be measured directly from observations and there is still the problem of the integration along the line-of-sight. We cannot know for sure if the emission our instruments measure is coming exclusively from the structure we want to study or if this emission comes also from the plasma that lies above and underneath the structure.

Even though we cannot measure $N(X_j^{+m})$ directly, we can measure several ratios of different physical quantities. We can rewrite Eq. (2.1) as:

$$I_{ij} = \int \frac{h\nu_{ij}}{4\pi} \frac{N(X_j^{+m})}{N(X^{+m})} \frac{A_{ij}}{N_e} \frac{N(X^{+m})}{N(X)} \frac{N(X)}{N(H)} \frac{N(H)}{N_e} N_e^2 dz, \tag{2.2}$$

where

- $N(X_j^{+m})$ / $N(X^{+m})$ is the ratio between the number density of X^{+m} ions in the energy level j and the number density of X^{+m} ions (at any energy level), or the relative level population,
- $N(X^{+m})$ / $N(X)$ is the ionization ratio of the ion X^{+m} relative to the total number density of element X, or the relative ion population,
- $N(X)$ / $N(H) = A_X$ is the elemental abundance relative to hydrogen, this is the quantity we are interested in when measuring the FIP bias as seen in Eqs. (1.1) and (1.2)
- $N(H)$ / $N_e \sim 0.83$ for $T > 10^5 K$ is the abundance of hydrogen relative to the free electron density.

Usually, all atomic physics parameters are combined under the so-called *contribution function* $C(T, \lambda_{ij}, N_e)$ and, assuming the abundances are uniform along the line-of-sight, we can rewrite equation (2.1) as follows:

$$I_{ij} = A_X \int C(T, \lambda_{ij}, N_e)\, N_e^2 dz, \tag{2.3}$$

where our contribution function is defined as

$$C(T, \lambda_{ij}, N_e) = \frac{h\nu_{ij}}{4\pi} \frac{N(X_j^{+m})}{N(X^{+m})} \frac{A_{ij}}{N_e} \frac{N(X^{+m})}{N(X)} \frac{N(H)}{N_e}. \tag{2.4}$$

There are alternative definitions of the contribution function in literature. Some include the abundance, others do not include the factor $1/4\pi$ or assume a fixed value for the hydrogen ratio to the free electron density. This contribution function is at the core of our method as we will see later.

In order to determine the abundance A_X for every chemical element in the corona, we could simply divide the intensity of the line I_{ij} by the integral $\int C(T, \lambda_{ij}, N_e)\, N_e^2 dz$. This task is not as simple as it seems. In the following two sections, we will take a look at the two components of this integral. One thing we can already bring up is that N_e^2 does not depend on any specific spectral line, the square of the electron density is the same for all lines. This will not be the case for the contribution functions.

2.2 THE CONTRIBUTION FUNCTION

The contribution function contains all the parameters of atomic physics that play a role in line formation. Under the hypotheses stated in Sect. 2.1, $C(T, \lambda_{ij}, N_e)$ can actually be computed using atomic databases that provide energy levels, transitions,

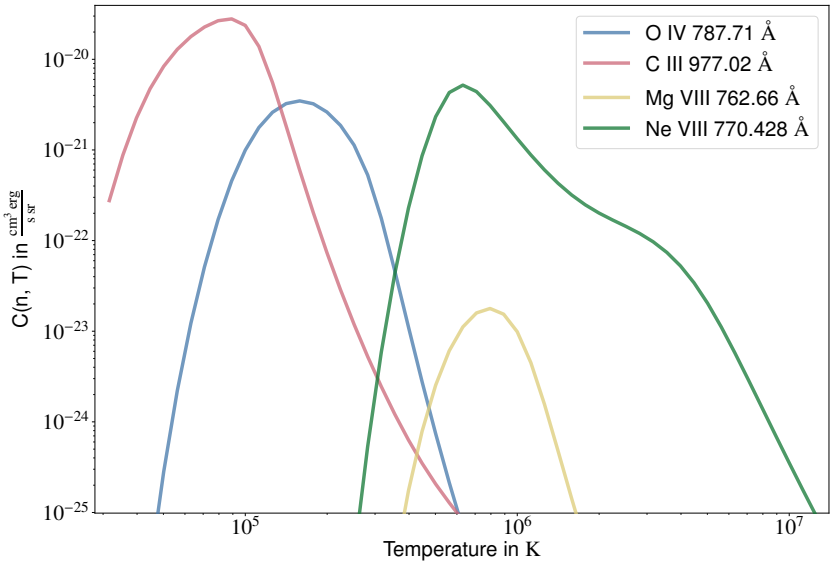

Figure 2.1: Examples of contribution functions in erg cm^3 s^{-1} sr^{-1} of different spectral lines as functions of the temperature. All of them were calculated at constant electron density $n_e = 10^{8.5}$ cm^{-3}.

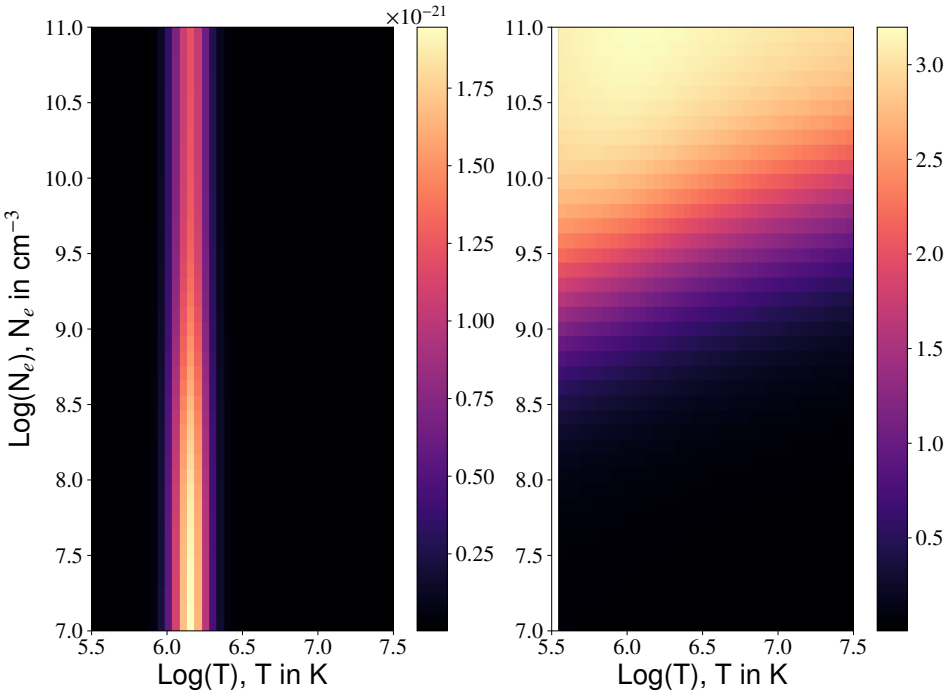

Figure 2.2: Left: Contribution function of the Si X 256.377 Å line as a function of temperature (abscissa) and density (ordinates) in cm^3 erg / s / sr. Right: Ratio of the contribution functions of the Fe XIII 203.826 Å and 202.044 Å lines as a function of temperature (abscissa) and density (ordinates). This ratio is commonly used to measure densities in the corona.

radiative transfer probabilities and excitation rates for individual lines. Consequently, astrophysicists work closely with atomic physicists in order to understand how the different ratios in Eq. (2.2) can be determined. In order to develop our method for FIP bias measurement, we used the *CHIANTI*[1] database [Dere et al., 1997]. It is an atomic database for spectroscopic diagnostics of astrophysical plasma. It can be used to interpret spectral lines and continua emitted from optically-thin astrophysical sources at high-temperature such as coronal plasma.

We used the *ChiantiPy* library, which is a pure Python package. It uses the *CHIANTI* database to calculate different parameters of use and it can also produce synthetic spectra, which are very helpful when trying to interpret observed spectra. *ChiantiPy* contains routines that can determine the relative level population under the hypothesis of ionization equilibrium for example.

In Fig. 2.1 we can see the contribution functions of four different lines of different ions. I would like to draw attention to the fact that these functions are very dependent on the temperature. It is more likely for an ion to emit a certain line in a given temperature. For example, if we take Mg VIII, the atom has lost 7 electrons. In order for this to happen, the temperature has to be very high, which is why it is no surprise that the contribution for the 762.66 Å line of this ion peaks at high temperatures. On the other hand, C III has only lost 2 electrons, therefore, we would expect the contribution function of a C III line to peak at lower temperatures. The contribution functions depend strongly on temperature and depend less on density as we can see in the left panel of Fig. 2.2. There are however line ratios for some ions, such as the Fe XIII one portrayed in the right panel of Fig. 2.2, that are very density dependent and that can be used for density diagnosis.

I would also like to insist on the fact that the shapes and values of the different contribution functions are specific to each line. The contribution function contains all atomic physics parameters that play a role in line formation, and it is different for each spectral line. In the case of many-level ions, Eq. (2.3) is still valid, but C_{ij} has to be computed through more complex atomic physics models. CHIANTI does allow one to compute the emission of many level ions coming from spontaneous emission but also includes other processes than collisional electron excitation populating excited levels such as collisional proton excitation for example [Young et al., 2003]. Other atomic databases can also be used to compute contribution functions. They might compute the contribution function using other rates coming from different atomic physics models or measurements and they also might include more or less physical

[1] CHIANTI is a collaborative project involving George Mason University, the University of Michigan (USA), University of Cambridge (UK) and NASA Goddard Space Flight Center (USA).

phenomena contributing to ion population and level population. Let's now take a look at the other term in the integral in Eq. (2.3).

2.3 THE DIFFERENTIAL EMISSION MEASURE

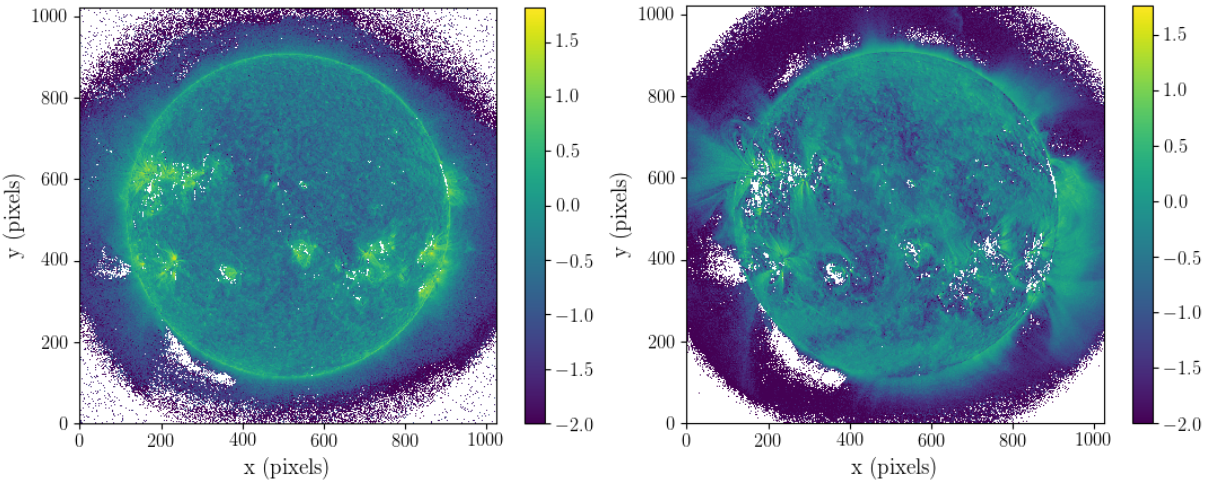

(a) Temperature: 500 000 K

(b) Temperature: 1 250 000 K

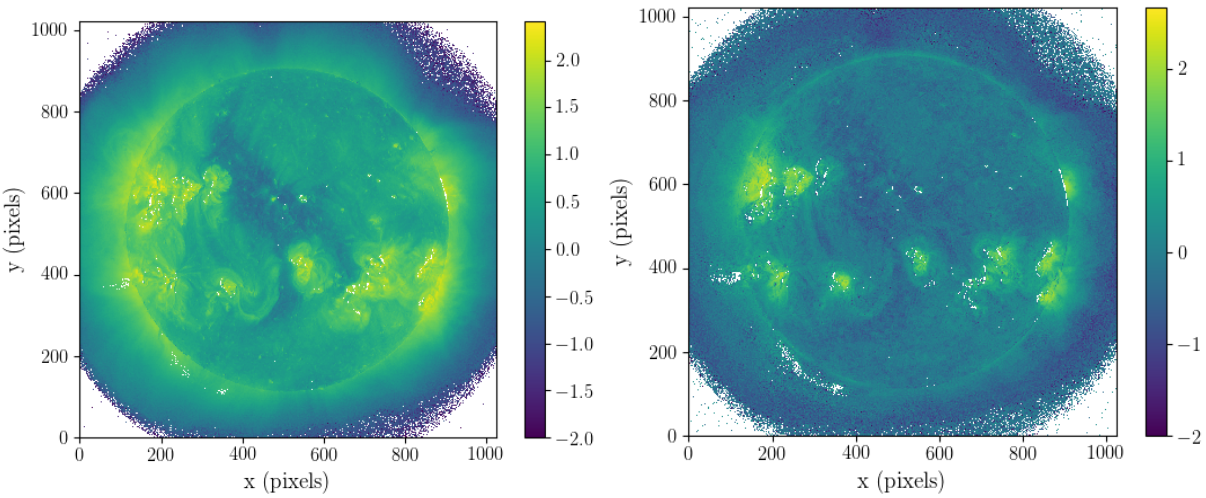

(c) Temperature: 2 000 000 K

(d) Temperature: 4 000 000 K

Figure 2.3: Emission measure at different temperatures as calculated with the method described in Cheung et al. [2015] from AIA observations on June 3rd 2012. The colorbar is in base-10 logarithmic scale: 0 corresponds to an emission measure of 10^{26} cm^{-5}, 1 corresponds to an emission measure of 10^{27} cm^{-5}, -1 corresponds to an emission measure of 10^{25} cm^{-5}, etc.

In order to determine the abundance A_X for every chemical element in the corona, according to Eq. (2.3), we need to know the contribution function as well as the plasma distribution along the line-of-sight $N_e^2(z)$. In contrast to the contribution function, the

distribution of N_e^2 as a function of position along the line-of-sight is the same for all lines.

Knowing exactly what is making a spectral line shine brighter or dimmer is difficult as the spatial distribution of the plasma parameters T and N_e is lost in integration. For example, there could be a single structure at a given temperature emitting the observed radiation; but there could also be several superimposed structures emitting at the same temperature. There is no way of knowing when observing with a single instrument.

However, the usual shape of contribution functions (with a strong dependence on temperature and a weaker dependence on density for most spectral lines) tends to select some temperature range for a given spectral line. Plus, as we are dealing with an optically thin collision dominated plasma, a volume element of plasma will be radiatevely decoupled from its environment. This means that we can think of the solar corona as a collection of small volumes of quasi-isothermal plasmas [Kashyap and Drake, 1998]. Instead of integrating along the line of sight, we will then integrate over small volumes of plasma that are at a certain temperature. We substitute T for z in the integral by writing

$$I_{ij} = \int A_X^C \, C_{ij}(T, N_e) \, \mathrm{DEM}(T) \, dT, \tag{2.5}$$

where we have introduced the differential emission measure (DEM). It can be defined by

$$\mathrm{DEM}(T) = N_e^2 \frac{dz}{dT} \tag{2.6}$$

in the simple case where temperature is a strictly monotonous function of the position along the line of sight. This quantity evaluated at a temperature T measures the amount of the observed plasma that contributes to the emission in a temperature range $[\, T : T + dT \,]$ [Craig and Brown, 1976]. We can also define the emission measure (EM) which corresponds to the DEM(T) integrated over temperature bins. Then $\int C(T) \, \mathrm{DEM}(T) \, dT \approx \sum_i C(T_i) \, \mathrm{EM}(T_i)$, where the sum is over the temperature bin centres.

The DEM or EM can be inferred from Eq. (2.5) using several different EUV spectral lines or emission bands. One example of the ways of determining the EM of a plasma structure is the EM inversion code by Cheung et al. [2015]. This particular routine uses observations taken with the Atmospheric Imaging Assembly (AIA) instrument aboard the Solar Dynamics Observatory (SDO), and finds a sparse solution, i.e. it uses a minimum number of basis functions of $\mathrm{EM}(T)$ to produce an $\mathrm{EM}(T)$ compatible with the observations. In Fig. 2.3 we show an example of EM maps obtained using the Cheung et al. [2015] code (version 1.001), which is available in the SDO/AIA package in SolarSoft. We assume our temperature bins to have a width of $\Delta \log T = 0.05$. This EM was computed at a maximum of solar activity so that the emission of the solar

surface was as inhomogeneous as possible. The emission measure data obtained corresponds to a cube where the first two axes are x and y in pixels and the third axis is temperature: we have the Emission Measure pixel by pixel of our image.

There are many different structures present on the Sun during solar maximum, all emitting at different temperatures, which will yield an EM that depends strongly on position. It is exactly what we see in the emission measures represented in Fig. 2.3 obtained from SDO/AIA data rebinned by a factor 4×4. In Fig.2.3(a), we can see that plasma at 500 000 K (the lowest temperature of the four figures) is present in virtually all types of structures. With increasing temperatures in Figs. 2.3(b), 2.3(c) and 2.3(d), we can see that active regions are made of hotter plasma and that they have more emitting plasma than the central coronal hole.

Different methods exist to determine the DEM from observations (using several spectroscopic lines or spectral bands) that consist in integral inversion methods. However, this is not an easy task as these methods have many limitations [Craig and Brown, 1976, Laming, 2015, Landi et al., 2012]. For most DEM determination techniques, a previous measurement of the density is needed. The insufficiency of the available data as well as the intrinsic nature of DEM inversion make it a difficult, ill-constrained problem that is very poorly conditioned in the density dimension [Judge et al., 1997, Testa et al., 2012b]. Through the application of some of these inversion methods to synthetic data, one finds that the general shape of the DEM is not always well retrieved and the finer details are not always well resolved [Testa et al., 2012b]. As in any such problem, different DEM(T) functions can equally reproduce the observed radiances. Furthermore, when dealing with synthetic observations of multithermal plasma, DEM inversion fails to find a good match with the 'true' DEM [Testa et al., 2012b] and isothermal DEM inversion solutions for a multithermal plasma are biased to specific temperature intervals, for a given set of spectroscopic lines [Guennou et al., 2012b].

2.4 FIP BIAS DETERMINATION

Different methods exist to determine photospheric abundances with remarkable accuracy even though there have been significant shifts in abundances of certain elements (oxygen in particular) throughout the years [Asplund et al., 2009, Caffau et al., 2011, Schmelz et al., 2012, Grevesse et al., 2015, Scott et al., 2015a,b]. Photospheric abundances do not vary with solar surface location or from one particular solar feature to another. On the other hand, coronal abundances, which are derived from EUV spectroscopy, are much more difficult to measure accurately, as evidenced by the discrepancies between different measurements that were previously taken as a

reference by the solar community [Schmelz et al., 2012]. Even though the radiance of a EUV spectral line emitted by an ion is proportional to its abundance, the latter is difficult to determine. This can be explained because many other parameters come into play, related to plasma conditions or to atomic physics, with high uncertainties for some of them.

Let us consider two spectroscopic lines emitted by ions of two different elements: X_{LF} that has a low FIP (LF, $< 10\,\mathrm{eV}$) and X_{HF} that has a high FIP (HF). The radiance and contribution function are for one given spectral line of the LF or HF element, so for simplicity we can drop here the index corresponding to the line or transition and note the contribution functions as C_{LF} and C_{HF} and the radiance is denoted I_{LF} and I_{HF}.

Assuming that abundances are uniform along the relevant part of the line of sight, in the corona, we can write Eq. (2.5) for both lines as

$$I_{LF} = A^{C}_{LF} \langle C_{LF}, DEM \rangle \tag{2.7}$$

$$I_{HF} = A^{C}_{HF} \langle C_{HF}, DEM \rangle, \tag{2.8}$$

where A^{C}_{X} are the coronal abundances for each element, C_{LF} and C_{HF} are the contribution functions for the lines of the low-FIP and high-FIP elements, respectively, and we note the integral in Eq. (2.5) as a scalar product $\langle a, b \rangle \equiv \int a(T)\, b(T)\, dT$.

Introducing the photospheric abundance A^{P}_{X} and the FIP bias $f_X \equiv A^{C}_{X}/A^{P}_{X}$ for element X, the ratio of line radiances becomes

$$\frac{I_{LF}}{I_{HF}} = \frac{A^{P}_{LF}}{A^{P}_{HF}} \frac{f_{LF}}{f_{HF}} \frac{\langle C_{LF}, DEM \rangle}{\langle C_{HF}, DEM \rangle}. \tag{2.9}$$

First ionization potential biases are usually calculated either from the line ratio of two spectral lines (hereafter 2LR method) or following Differential Emission Measure (DEM) analysis; both these methods can yield different results when used on the same data. We now take a look at both of them.

2.4.1 *Using spectral line radiance ratios*

When two spectral lines, one from a low-FIP ion and another from a high-FIP ion, can be chosen so that their contribution functions are very close (at some factor which can then be approximated by $\max(C_{LF})/\max(C_{HF})$), the ratio of the scalar products in Eq. (2.9) becomes almost independent from the DEM, and the relative FIP bias becomes

$$\frac{f_{LF}}{f_{HF}} \approx \frac{I_{LF}}{I_{HF}} \left(\frac{A^{P}_{LF} \max(C_{LF})}{A^{P}_{HF} \max(C_{HF})} \right)^{-1}. \tag{2.10}$$

This is simply the ratio of the radiances multiplied by some constant factor.

This method only works if we are able to find two lines that have similar contribution functions. Of course, finding such adequate line pairs of low-FIP and high-FIP elements with similar contribution functions is difficult and not always possible given the observational constraints. Furthermore, no two contribution functions have the exact same shape, so there is some hidden dependence on the DEM, and this method is often not accurate.

If the shapes of the contribution functions are not similar, the other option we have is to determine the EM.

2.4.2 *Using DEM inversion to derive FIP bias*

When the DEM can be inferred from observations and the contribution functions computed from atomic calculations, the relative FIP bias between high-FIP and low-FIP elements can then be derived from Eq. (2.9) using the observed radiances and assuming the photospheric abundances:

$$\frac{f_{LF}}{f_{HF}} = \frac{I_{LF}}{I_{HF}} \left(\frac{A^{P}_{LF}}{A^{P}_{HF}} \frac{\langle C_{LF}, DEM \rangle}{\langle C_{HF}, DEM \rangle} \right)^{-1}. \tag{2.11}$$

This ratio is simply the low-FIP element abundance bias f_{LF} if we consider that $f_{HF} = 1$.

In practice, the required DEM inversion itself is sensitive to FIP bias, especially because DEM inversion often involves iron lines, a low-FIP element. This sensitivity can however be used as a way to determine the FIP bias, as in e.g. Baker et al. [2013], Guennou et al. [2015]. The steps generally taken to retrieve the relative FIP bias using spectral lines are the following:

- Retrieve radiances from observations of a number of spectral lines from low FIP and high-FIP elements.
- Determine the density (for every pixel in the observation) and use it to compute the contribution functions of the spectral lines used for the analysis.
- Infer the DEM from the radiances of the spectral lines of a low FIP element only, assuming photospheric abundances. This 'inferred' DEM is obtained by inversion of the observed radiances written as

$$I_{ij,\chi_{LF}} = A^{P}_{LF} \langle C_{ij,\chi_{LF}}, DEM^{inferred} \rangle. \tag{2.12}$$

  As in reality this element is subject to the FIP effect, the radiances are in fact

$$I_{ij,\chi_{LF}} = f_{LF} A^{P}_{LF} \langle C_{ij,\chi_{LF}}, DEM \rangle, \tag{2.13}$$

where the DEM is the real DEM. The inferred DEM is then overestimated by a factor

$$\frac{\mathrm{DEM}^{\mathrm{inferred}}}{\mathrm{DEM}} = f_{\mathrm{LF}}. \tag{2.14}$$

- Compute the ratio of the simulated (with $\mathrm{DEM}^{\mathrm{inferred}}$)[2] and observed radiances of a high-FIP element spectral line:

$$\frac{I_{\mathrm{HF}}^{\mathrm{simulated}}}{I_{\mathrm{HF}}^{\mathrm{observed}}} = \frac{A_{\mathrm{HF}}^{\mathrm{P}} \langle C_{\mathrm{HF}}, \mathrm{DEM}^{\mathrm{inferred}} \rangle}{f_{\mathrm{HF}} A_{\mathrm{HF}}^{\mathrm{P}} \langle C_{\mathrm{HF}}, \mathrm{DEM} \rangle} \tag{2.15}$$

$$= \frac{f_{\mathrm{LF}} A_{\mathrm{HF}}^{\mathrm{P}} \langle C_{\mathrm{HF}}, \mathrm{DEM} \rangle}{f_{\mathrm{HF}} A_{\mathrm{HF}}^{\mathrm{P}} \langle C_{\mathrm{HF}}, \mathrm{DEM} \rangle} \tag{2.16}$$

$$= \frac{f_{\mathrm{LF}}}{f_{\mathrm{HF}}}. \tag{2.17}$$

  This ratio is then the relative FIP bias.

In order to accurately obtain a FIP bias with the 2LR technique, both spectral lines have to be formed at very close temperatures, while using the DEM allows more flexibility in the choice of lines. However, as seen in Sec. 2.4.2, the DEM is difficult to estimate accurately, especially when trying to design an automated method. Therefore, a FIP bias determination that would not rely on DEM inversion, like the 2LR method, but that would also be more accurate than the 2LR method would be very convenient. These issues and short-comings were the main motivations for us to develop an entirely new method.

In the following chapter, I will present a new method to measure relative abundances using spectroscopic observations. It is based on the DEM formalism and relies on linear combinations of spectral lines to get rid of the dependence on DEM inversion for FIP bias determination.

[2] If one wants to compute the FIP bias for another low-FIP element (e.g. Si, when the DEM was computed using Fe lines), the inferred DEM is re-scaled so that it reproduces the observed radiance of a line of that element.

3

CORONAL ABUNDANCES WITH OPTIMISED LINEAR COMBINATIONS OF SPECTRAL LINES

This chapter is taken from Zambrana Prado and Buchlin [2019], Measuring relative abundances in the solar corona with optimised linear combinations of spectral lines, published in Astronomy & Astrophysics. It corresponds to section 3 and onward of that paper.

Context. *Elemental abundances in some coronal structures differ significantly from photospheric abundances, with a dependence on the first ionization potential (FIP) of the element. Measuring these FIP-dependent abundance biases is important for coronal and heliospheric physics.*

Aims. *We aim to build a method for optimal determination of FIP biases in the corona from spectroscopic observations in a way that is in practice independent from Differential Emission Measure (DEM) inversions.*

Methods. *We optimised linear combinations of spectroscopic lines of low-FIP and high-FIP elements so that the ratio of the corresponding radiances yields the relative FIP bias with good accuracy for any DEM in a small set of typical DEMs.*

Results. *These optimised linear combinations of lines allow retrieval of a test FIP bias map with good accuracy for all DEMs in the map. The results also compare well with a FIP bias map obtained from observations using a DEM-dependent method.*

Conclusions.*The method provides a convenient, fast, and accurate way of computing relative FIP bias maps. It can be used to optimise the use of existing observations and the design of new observations and instruments.*

3.1 A NEW WAY OF MEASURING THE FIP EFFECT: THE LINEAR COMBINATION RATIO METHOD

3.1.1 *Light bulb*

For some elements, as mentioned above, we can make relative abundance diagnostics without knowing the DEM, by using radiance ratios of the spectral lines of a low-FIP element and a high FIP element, provided they both have very similar contribution functions. Such lines are not always observable however, or their contribution functions are not close enough. Our idea is therefore to generalise this technique by using linear combinations of lines so that the corresponding contribution functions for low-FIP and high-FIP elements are a better match.

We start by defining two radiance-like quantities that would be the analogues of the radiances of Eqs. (2.7)–(2.8), as linear combinations of radiances from individual lines of low-FIP and high-FIP elements:

$$\mathscr{I}_{\mathrm{LF}} \equiv \sum_{i\in(\mathrm{LF})} \alpha_i \, \frac{I_i}{A_i^P}, \tag{3.1}$$

$$\mathscr{I}_{\mathrm{HF}} \equiv \sum_{i\in(\mathrm{HF})} \beta_i \, \frac{I_i}{A_i^P}. \tag{3.2}$$

Please note that the normalization by photospheric abundances here is only a matter of convention.

Using Eq. (2.5), these quantities become

$$\mathscr{I}_{\mathrm{LF}} = \sum_{i\in(\mathrm{LF})} \alpha_i \, f_i \, \langle C_i, \, \mathrm{DEM}\rangle, \tag{3.3}$$

$$\mathscr{I}_{\mathrm{HF}} = \sum_{i\in(\mathrm{HF})} \beta_i \, f_i \, \langle C_i, \, \mathrm{DEM}\rangle. \tag{3.4}$$

If the FIP biases of all used low-FIP elements are the same (and equal to f_{LF}), and the FIP biases of all used high-FIP elements are the same (and equal to f_{HF}), the ratio of the radiance-like quantities is

$$\frac{\mathscr{I}_{\mathrm{LF}}}{\mathscr{I}_{\mathrm{HF}}} = \frac{f_{\mathrm{LF}} \sum_{i\in(\mathrm{LF})} \alpha_i \, \langle C_i, \mathrm{DEM}\rangle}{f_{\mathrm{HF}} \sum_{i\in(\mathrm{HF})} \beta_i \, \langle C_i, \, \mathrm{DEM}\rangle} \tag{3.5}$$

$$= \frac{f_{\mathrm{LF}} \, \langle \mathscr{C}_{\mathrm{LF}}, \mathrm{DEM}\rangle}{f_{\mathrm{HF}} \, \langle \mathscr{C}_{\mathrm{HF}}, \mathrm{DEM}\rangle}, \tag{3.6}$$

where the low-FIP and high-FIP contribution functions have been defined by

$$\mathscr{C}_{\mathrm{LF}}(T) \equiv \sum_{i\in(\mathrm{LF})} \alpha_i \, C_i(T), \tag{3.7}$$

$$\mathscr{C}_{\mathrm{HF}}(T) \equiv \sum_{i\in(\mathrm{HF})} \beta_i \, C_i(T), \tag{3.8}$$

then the relative FIP bias is

$$\frac{f_{LF}}{f_{HF}} = \frac{\mathscr{I}_{LF}}{\mathscr{I}_{HF}} \left(\frac{\langle \mathscr{C}_{LF}, DEM \rangle}{\langle \mathscr{C}_{HF}, DEM \rangle} \right)^{-1}. \tag{3.9}$$

This is analogous to Eq. (2.10) but for the linear combinations of radiances and of contribution functions.

3.1.2 *Finding the optimal linear combinations*

So that the relative FIP bias can be retrieved from observations without determining the DEM, our first idea was to optimise the linear combination coefficients so that the following cost function is minimised:

$$\phi(\alpha, \beta) = \|\mathscr{C}_{LF} - \mathscr{C}_{HF}\| = \left\| \sum_{i \in (LF)} \alpha_i C_i - \sum_{i \in (HF)} \beta_i C_i \right\|, \tag{3.10}$$

where the distance is defined from the scalar product: $\|a\|^2 \equiv \langle a, a \rangle$. If there is no difference between $\mathscr{C}_{LF}$ and $\mathscr{C}_{HF}$, the relative FIP bias from Eq. (3.9) is indeed simply $\mathscr{I}_{LF}/\mathscr{I}_{HF}$. However, if differences remain, especially in the wings of the linear combinations of contribution functions, the result remains sensitive to the DEM.

We therefore decided to look at the problem from a different angle but with a similar approach. Instead of building the cost function ϕ from the distance between the contribution functions as in Eq. (3.10), we came back to Eq. (3.6) and built a new cost function in such a way that after optimisation the ratio $\langle \mathscr{C}_{LF}, DEM \rangle / \langle \mathscr{C}_{HF}, DEM \rangle$ would become as close to 1 as possible for any DEM. As we do not want to compute the DEM in each pixel, this means that we have to choose a set $(DEM_j)_j$ of 'reference' DEMs that would be representative of the DEMs in the map, and we then define the cost function as

$$\phi(\alpha, \beta) = \sqrt{\sum_{j \in (DEM_j)_j} \left| \frac{\sum_{i \in (LF)} \alpha_i \langle C_i, DEM_j \rangle}{\sum_{i \in (HF)} \beta_i \langle C_i, DEM_j \rangle} - 1 \right|^2}. \tag{3.11}$$

This is simply the L2 distance between vector

$$(\psi_j)_j \equiv (\langle \mathscr{C}_{LF}, DEM_j \rangle / \langle \mathscr{C}_{HF}, DEM_j \rangle)_j \tag{3.12}$$

and vector $(1)_j$.

Through the minimisation of ϕ we obtain the coefficients α_i and β_i. Provided that the set of DEMs used to define the cost function from Eq. (3.11) is adequate, we then have $\psi_{DEM} \equiv \langle \mathscr{C}_{LF}, DEM \rangle / \langle \mathscr{C}_{HF}, DEM \rangle \approx 1$ in each pixel and, following Eq. (3.9), the relative FIP bias can be simply retrieved as

$$\frac{f_{LF}}{f_{HF}} = \frac{\mathscr{I}_{LF}}{\mathscr{I}_{HF}} \psi_{DEM}^{-1} \approx \frac{\mathscr{I}_{LF}}{\mathscr{I}_{HF}}. \tag{3.13}$$

This allows us to build relative FIP bias maps from spectroscopic observations without having to determine the DEM in each pixel. We call this method Linear Combination Ratio (LCR) method.

We note that the 2LR technique, as defined by Eq. (2.10), is a special case of a linear combination and can be expressed with the same formalism as the LCR method: a single line from a low-FIP element is chosen along with a single line from a high-FIP element, and the linear combination coefficients are

$$\alpha = \frac{1}{\max(C_{LF})} \qquad \text{and} \qquad \beta = \frac{1}{\max(C_{HF})} \tag{3.14}$$

for the single LF and HF lines, instead of being the result of an optimisation.

3.1.3 *Implementing the LCR method*

We have developed a Python module[1] to compute the optimal linear combinations of spectral lines and to use them to compute relative FIP bias maps from observations.

We describe the different steps to apply the method to observations of EUV spectra in the following.

Selection of the spectral lines

We first need to choose the spectral lines that we want to use. This has to be done by hand, and depends on the lines available for a given observation, instrument, or wavelength range. The following criteria should be taken into consideration:

- The lines have to verify the coronal approximation (see Sect. 2.1).
- They have to form at coronal temperatures; if they form at lower temperatures opacity effects would have to be taken into account.
- The observed signal-to-noise ratio of each line radiance has to be sufficient. The noise in the observed radiance of a weak line propagates indeed to the corresponding linear combination of radiances, especially when it is amplified by a large coefficient in the linear combination.
- Blended lines have to be avoided or de-blended so that the true spectral line radiance is used.
- The atomic physics for the spectral lines has to be well known. Examples of some of the problems that one might encounter are an underestimation of the observed flux in the 50–130 Å wavelength range [Testa et al., 2012a] or anomalous

[1] https://git.ias.u-psud.fr/nzambran/fiplcr

behaviour for ions of the Li and Na isoelectronic sequences for which the atomic physics models tend to underestimate line radiance (Del Zanna et al. 2001; Sect. 7.4 of Del Zanna and Mason 2018). The quality of the atomic data will depend on the database chosen. For the purpose of this paper, we use CHIANTI (version 9.0, previous versions described in Dere et al. 1997, Del Zanna et al. 2015) through the `ChiantiPy` Python package (version 0.8.5), but in principle another database can be used.

- The maximums of the contribution functions of all lines should be at similar temperatures so that we do not mix abundances at various heights.

Computation of the contribution functions

We use the CHIANTI atomic physics database to compute the contribution functions. We also use it to retrieve information about each spectral line, such as typical photospheric abundance, FIP of the element, and upper and lower levels of the transition. Furthermore, for the cases when density maps can be obtained, for example when using a radiance ratio between a pair of lines with different density sensitivities, we compute these contribution functions on a grid of temperatures and densities.

Determination of the optimal linear combinations

Lines are first separated into two subsets, (LF) for lines from low-FIP elements and (HF) for lines from high-FIP elements. We then minimise the cost function ϕ defined by Eq. (3.11) using a very simple set of DEMs, constituted by the typical DEMs provided by CHIANTI for an active region (AR), a coronal hole (CH), and the quiet Sun (QS). For this minimisation, we use the Nelder and Mead [1965] optimisation implemented in the `SciPy` library [Jones et al., 2001–]. As a first guess for the coefficients for each linear combination, we use the median of the maximums of the contribution functions divided by each of these maximums. The optimisation then yields a set of optimal coefficients, $(\alpha_i)_{i\in LF}$ and $(\beta_i)_{i\in HF}$. These coefficients can be optimised for the density grid mentioned in Sect. 3.1.3 if required; we would then obtain optimised linear combination coefficients that are a function of density.

Determining the relative FIP bias

Once we have the coefficients of the linear combinations, we can compute the linear combinations of radiances $\mathscr{I}_{LF}$ and $\mathscr{I}_{HF}$ in each pixel, and then immediately obtain the relative FIP bias f_{LF}/f_{HF} from Eq. (3.13). If a density map can be obtained for the observation, we can compute the FIP bias in each pixel using the linear combination

coefficients best suited for that particular pixel depending on its density (the density dependence of the ratio of the radiances is further discussed in Appendix 3.A).

3.2 TESTING THE METHOD WITH SYNTHETIC RADIANCES

In this section we test the LCR method by applying it to maps of synthetic radiances, so that we control all parameters precisely (in particular the abundances). We also test the 2LR method with the same criteria for comparison.

The test case consists in a uniform abundance map for any given element, combined with a data cube of DEMs, as detailed below. Using both these inputs and atomic physics, we can build 'synthetic' radiances, meaning that they are computed rather than observed. The test is considered successful for a given FIP bias determination method if the output relative FIP bias map is consistent with the input elemental abundance maps, both in uniformity and in value. The test has four main steps, detailed below:

1. We derive a DEM cube from the AIA observation. This is for the sole purpose of producing synthetic radiances, for which we have control over all parameters, while the DEMs are representative of different real solar regions.

2. Using CHIANTI for the contribution functions and the derived DEMs, we calculate the synthetic radiances. We assume different uniform abundances for different elements.

3. We determine the optimal linear combination coefficients for the LCR methods, and the coefficients for the 2LR method.

4. We use these coefficients to retrieve the FIP bias in each pixel assuming Eq. (3.13) is verified. If this is the case, the retrieved FIP bias map should be uniform.

3.2.1 *Synthetic radiance maps*

We start by computing Emission Measure[2] (EM) maps using the Cheung et al. [2015] code (version 1.001), which is available in the SDO/AIA package in SolarSoft. This particular EM inversion method finds a sparse solution, that is, it uses a minimum number of basis functions to produce an $\mathrm{EM}(T)$ compatible with the observations.

We chose an observation of the Atmospheric Imaging Assembly [AIA; Lemen et al., 2012] instrument aboard the Solar Dynamics Observatory [SDO; Pesnell et al., 2012],

[2]The EM is the DEM(T) integrated over temperature bins, of width assumed to be $\Delta \log T = 0.05$ in this section. Then $\langle \mathscr{C}, \mathrm{DEM} \rangle \approx \sum_i \mathscr{C}(T_i)\,\mathrm{EM}(T_i)$, where the sum is over the temperature bin centres.

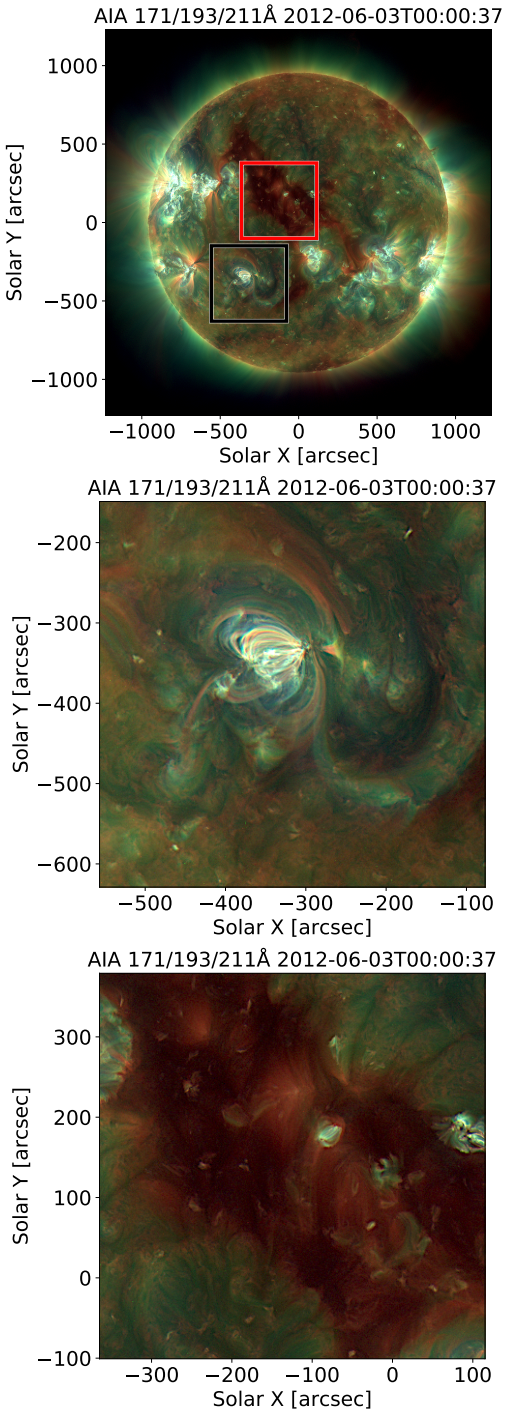

Figure 3.1: Top panel: Composite map of the solar corona on June 3, 2012, in the 171 Å (red), 193 Å (green), and 211 Å (blue) channels of the AIA instrument aboard SDO. The black and red squares correspond to the regions of interest used for testing the method, and are centred on an AR and a CH, respectively. Middle panel: Zoom on the AR region of interest (black square in top panel). Bottom panel: Zoom on the CH region of interest (red square in top panel).

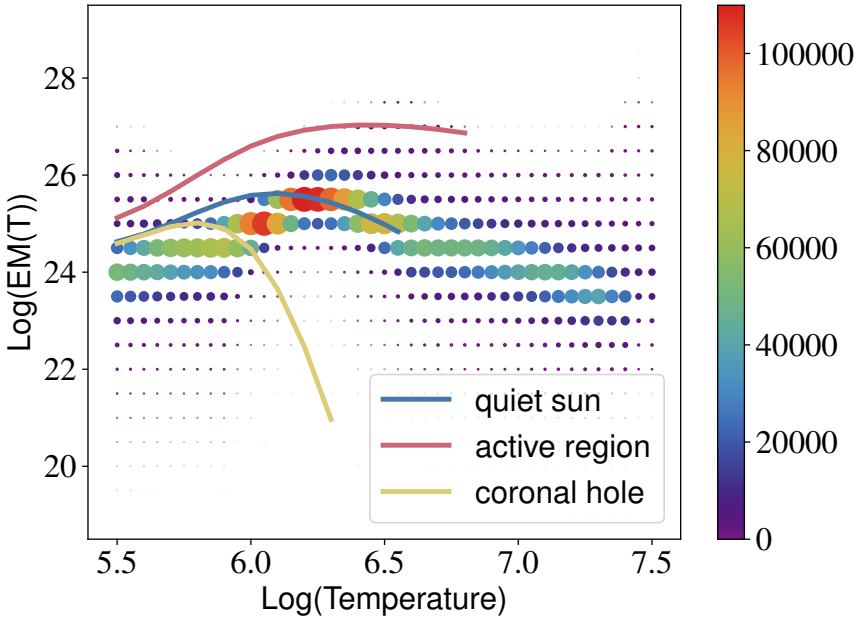

Figure 3.2: Histogram of the EM(T) values in the first region of interest (black square) of Fig. 3.1. The colour scale and the size of the points correspond to the number of pixels containing an EM of a given value at a given temperature. We have also traced in full lines the typical EMs from CHIANTI that we use to optimise the cost function (Eq. 3.11). The red line corresponds to an active region, the blue line to the quiet Sun and the yellow line to a coronal hole.

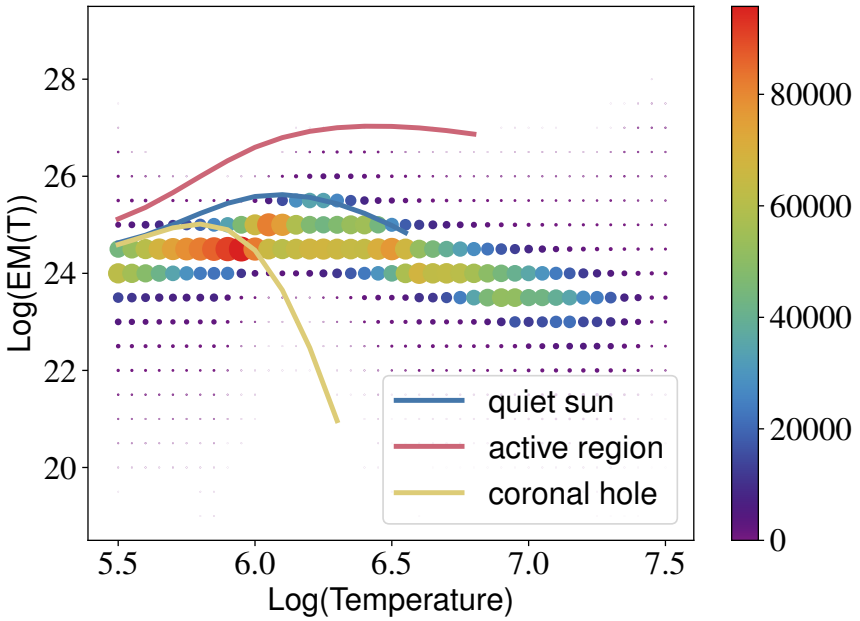

Figure 3.3: Same as Fig. 3.2 but for the second region of interest (red square) of Fig. 3.1.

Table 3.1: Spectral lines used to perform the calculations. All lines were used for the LCR method in Sect. 3.2 and 3.3. The lines in bold correspond to those used for the 2LR method in the tests in Sect. 3.2. For the 2LR method, the coefficients are defined by Eq. (3.14) which explains the factor 10^{25} by which both values are multiplied. For the LCR method they result from the optimisation. These coefficients were calculated for a density of log(n) = 8.3.

Ion	Wavelength (Å)	$\log T_{max}$ (K)	LCR coeff	2LR coeff (10^{20})
Fe XII	195.119	6.2	0.0845	
Fe XIII	201.126	6.2	−0.0738	
Fe XIII	202.044	6.2	0.0294	
Si X	**258.374**	6.1	1.36	4.26
Si X	261.056	6.1	1.46	
S X	**264.231**	6.2	2.16	3.34
Fe XIV	264.789	6.3	0.503	
Fe XIV	274.204	6.3	0.0404	

on June 3, 2012, close to the maximum of solar activity, so that the coronal emission is inhomogeneous. The Sun in this particular day presented various ARs and a large CH at the centre. As shown in Fig. 3.1, we select two separate regions of interest, one being centred on an AR, and the other centred on a CH. We aligned the images from the different detectors and divided each of them by their corresponding exposure time before doing the EM computations. The histograms of the EMs we obtain are shown in Figs. 3.2 and 3.3.

We selected lines available in the observations used by Baker et al. [2013], as in Sect. 3.3 we use the same observational data as these authors to compare the LCR

Table 3.2: First ionization potential of the elements used for the tests, their coronal and photospheric abundances taken from Schmelz et al. [2012] and Grevesse et al. [2007], and the corresponding abundance bias relative to sulfur.

Element	FIP (eV)	A_X^C	A_X^P	f_X/f_S
Fe	7.90	7.08×10^{-5}	2.82×10^{-5}	2.05
Si	8.15	7.24×10^{-5}	3.24×10^{-5}	1.82
S	10.36	1.69×10^{-5}	1.38×10^{-5}	1.00

Table 3.3: Value of ψ_j (Eq. 3.12) for both methods for each reference DEM, as well as the resulting cost function ϕ (Eq. 3.11).

Method	ψ_{QS}	ψ_{AR}	ψ_{CH}	ϕ
2LR	0.882	0.763	1.13	0.295
LCR	0.99998	1.00000	1.00001	2.8×10^{-5}

method results to their results. Eight lines were chosen following the criteria of Sect. 3.1.3 and are listed in Table 3.1. The temperature range of their maximums of formation goes from 1 MK to 2 MK. They include five iron lines, two silicon lines, and one sulfur line; iron and silicon are low-FIP elements, and, like Baker et al. [2013], we consider sulfur to be high-FIP. We further select Si X 258.374 Å as low-FIP line for the 2LR method.

We then create the required synthetic radiance maps using Eq. (2.5), assuming the relative abundance ratios presented in Table 3.2, which provide the 'ground truth' for the FIP biases we obtain using both methods. The abundances we assume here are uniform[3] over the regions of interest, and we take their values from Schmelz et al. [2012] for the corona and Grevesse et al. [2007] for the photosphere; these values and resulting relative FIP biases are presented in Table 3.2.

3.2.2 *Optimisation of the linear combinations of lines*

We present in Fig. 3.4 the contribution functions for the spectral lines listed in Table 3.1. All contribution functions were computed assuming a density of $10^{8.3}$ cm^{-3}. In the top panel of Fig. 3.4, we show the contribution functions of both lines used for the 2LR method, normalized by their maximum. As we can see, they are similar in shape from low temperatures until the maximum of both functions, but for higher temperatures they start to differ from one another significantly. In the bottom panel of Fig. 4, we present the contribution functions of all the lines we use to test the LCR method. They all have different shapes and values. Not all of them start at low temperatures, as ions with a high degree of ionization are formed only at higher temperatures.

After choosing the lines and computing their contribution functions, we determine the optimal linear combination of these lines for the LCR method (Sect. 3.1.3). The reference EMs that we use for the optimisation are plotted on Figs. 3.2 and 3.3. These

[3]Uniformity allows an easy comparison between the obtained FIP bias maps and the ground truth; however, any map could be assumed for the test, as the test (from synthetic radiances to FIP bias maps) gives a result that is proportional to the initial FIP bias in each pixel, as long as all the LF or HF element abundance vectors are collinear.

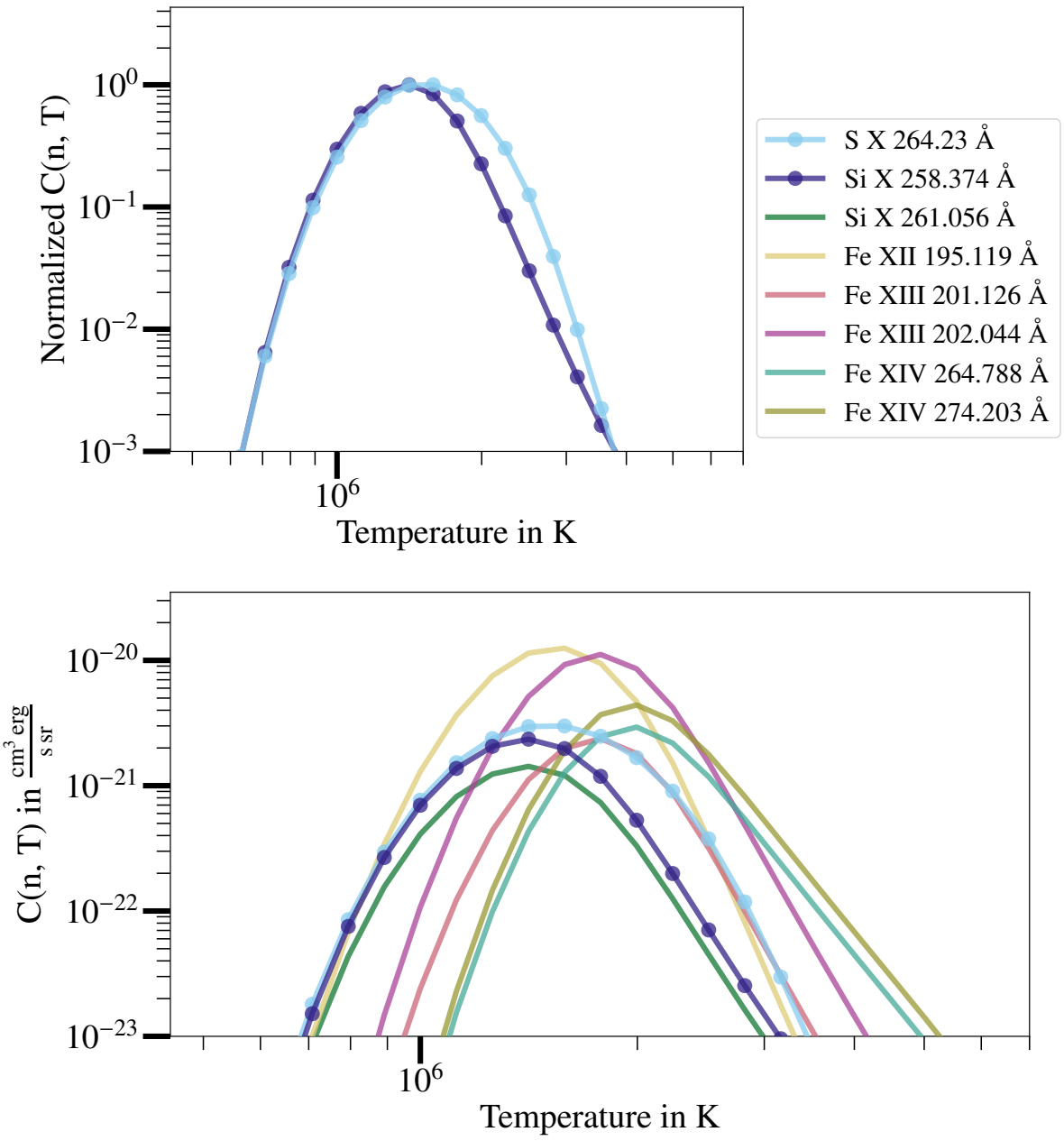

Figure 3.4: Top: Normalized contribution functions of the lines used for the 2LR method. Bottom: Contribution functions of the lines used for the LCR method. All the contribution functions were calculated assuming a constant density of $10^{8.3}\,cm^{-3}$.

are available in the CHIANTI database and correspond to typical EMs for a coronal hole, an active region, and the quiet Sun. The resulting coefficients are included in Table 3.1. For the 2LR method, we use the inverse of the maximum of the contribution functions of the Si X and of the S X lines as values for the (single) α and β coefficients, respectively, therefore allowing the use of the same formalism as for the LCR method.

In particular, we can compute the cost function defined in Eq. (3.11) for both the LCR method (following optimisation) and the 2LR method, as shown in Table 3.3. In this table we also give the components of vector ψ defined in Eq. (3.12), which ideally would all have to be equal to 1 so that the cost function ϕ would be zero. The values in this table already show that the optimisation made in the LCR method yields much better values for the cost function, as well as for each of the ψ components, compared to the same quantities for the line coefficients chosen for the 2LR method. This means that Eq. (3.9) would give very good estimates of the relative FIP bias for any of the three reference DEMs that we use. It is a first indication that the LCR method could work well.

3.2.3 *First ionization potential bias maps obtained from the synthetic radiances*

Applying Eq. (3.9) to the synthetic radiance maps, we now obtain maps of the relative FIP bias for both LCR and 2LR methods.

We present the results for the first region of interest (black square in Fig. 3.1) in Fig. 3.5. The top left panel of this figure clearly shows that we do not retrieve a uniform relative FIP bias using the 2LR method, as confirmed by the standard deviation of the FIP bias (0.15) and the corresponding histogram (bottom left). Furthermore, the histogram peak at about 1.51 is far from the imposed value for the relative FIP bias between the two elements used, silicon and sulfur (1.82). This could be because the normalized contribution function of the S X line goes well over (up to a factor 3.6) that of the Si X line in the temperature range at which the EM peaks ($\log T = 6.3$ to 6.4), as we can see in Fig. 3.4.

The LCR method gives a much more uniform map (top right panel), as confirmed by the corresponding histogram (bottom right) that has a standard deviation of 0.03, a factor of five smaller than that obtained with the 2LR method. Almost all obtained values are between the relative FIP biases for Fe and Si, as we discuss in Sect. 3.2.4. This histogram peaks at 1.87. These results show the accuracy of the linear combination ratio method.

In order to test if these results can be reproduced in regions other than an AR, we perform the same test in the red square of Fig. 3.1. We can see in Fig. 3.1 that this region contains very different structures than the first one, as the second region

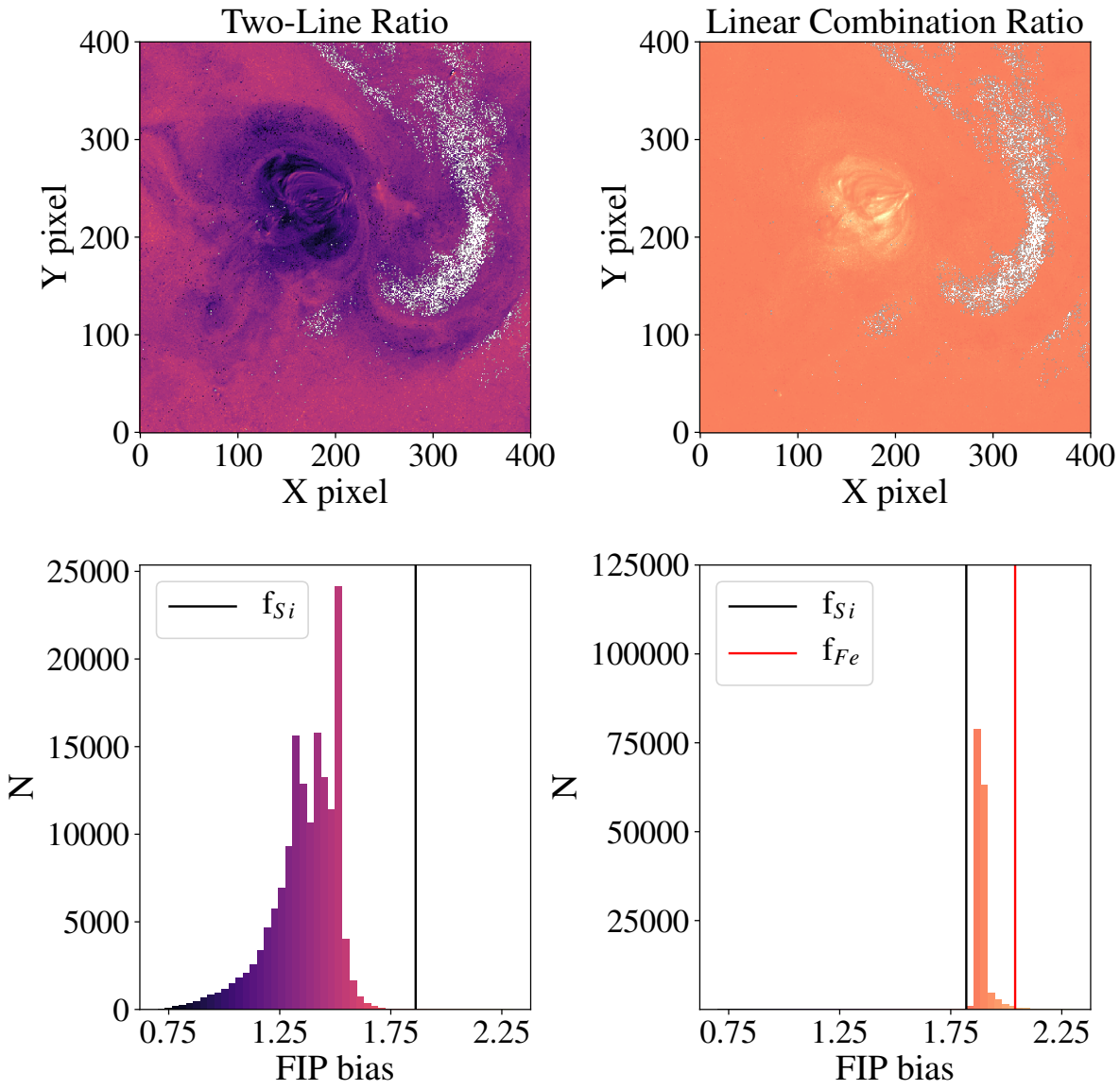

Figure 3.5: Results of FIP bias determination using the 2LR (left) and LCR (right) methods on the synthetic radiances in the first region of interest (black square) of Fig. 3.1: relative FIP maps (top) and their corresponding histograms (bottom), with matching colour scales. The DEM inversion code was not able to find a satisfactory solution in the pixels depicted in white. The vertical lines in the histograms correspond to the imposed uniform values of the relative FIP bias (for each of the low-FIP elements; see Table 3.2) that should ideally be retrieved.

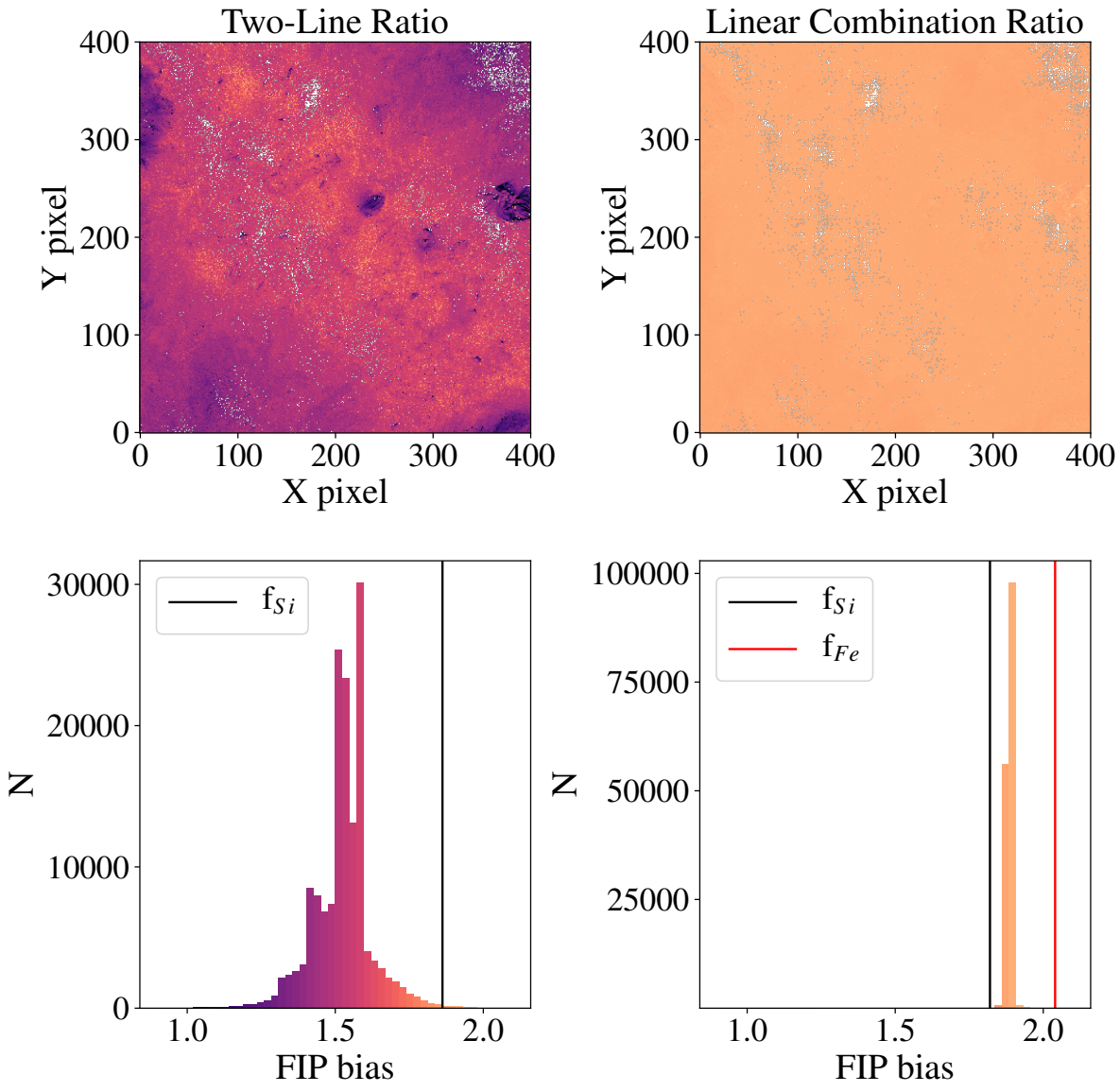

Figure 3.6: Same as Fig. 3.5 but for the second region of interest (red square) of Fig. 3.1.

includes part of a CH. In the results, presented in Fig. 3.6, we can see that the LCR method performs again better than the 2LR technique. We obtain a distribution of relative FIP biases peaking at 1.58 (with a standard deviation of 0.1) for the 2LR method, still very far from 1.82, and a distribution peaking at 1.9 (with a standard deviation of 0.015) for the LCR method. In this case, almost all values are again between the relative FIP biases for Fe and Si.

The LCR results are very close to the imposed FIP biases in both regions even though their EMs are very different (and each region already contains pixels with different EMs). This shows that the LCR method works properly and does not require prior knowledge of the DEM.

3.2.4 *Understanding the remaining non-uniformity in maps*

As the assumed FIP bias map (the ground truth for the test) was uniform, the non-uniformity in the result FIP bias map is a measure of the error in the FIP bias given by the tested method (LCR or 2LR) for this test setup (for the spectroscopic lines, reference EMs, and EM map used for the test). Other sources of error that cannot be assessed with such a test are discussed in Sect. 3.4.

Even though the relative FIP bias values obtained in this test with the LCR method have a standard deviation of 0.02 and 0.03 only in both regions of interest, the 1^{st} and 99^{th} percentiles are 1.78 and 1.88 respectively. Although much better than for the 2LR method, the non-uniformity of the FIP bias is still significant, and we ought to understand possible sources of the remaining non-uniformity in our test FIP bias maps.

OPTIMISATION RESIDUALS. Even after the optimisation, the residuals of the cost function Eq. (3.11) are not zero (Table 3.3). From Eq. (3.12), one understands that these residuals come from the fact that the products $\mathscr{C}_{\mathrm{LF}}(T)\,\mathrm{EM}(T)$ and $\mathscr{C}_{\mathrm{HF}}(T)\,\mathrm{EM}(T)$ for the different EMs used for the optimisation are not close enough. We trace these products for the three reference EMs we used and for both methods in Fig. 3.7.

Above $\log T = 6.2$, both LF and HF curves have the same shape for the LCR linear combinations, whereas this is not the case for the 2LR method. The yellow curves in the top panel of Fig. 3.7 show that, with the AR EM, the 2LR method would overestimate the SX contribution in the $\log T \in [6.2, 6.6]$ range by a factor up to 3.6. Above $\log T = 6.5$, the SX contribution would be underestimated for both methods, but we are far from the peak which means that the contribution of the radiance at these high temperatures might not contribute much to the overall observed radiance.

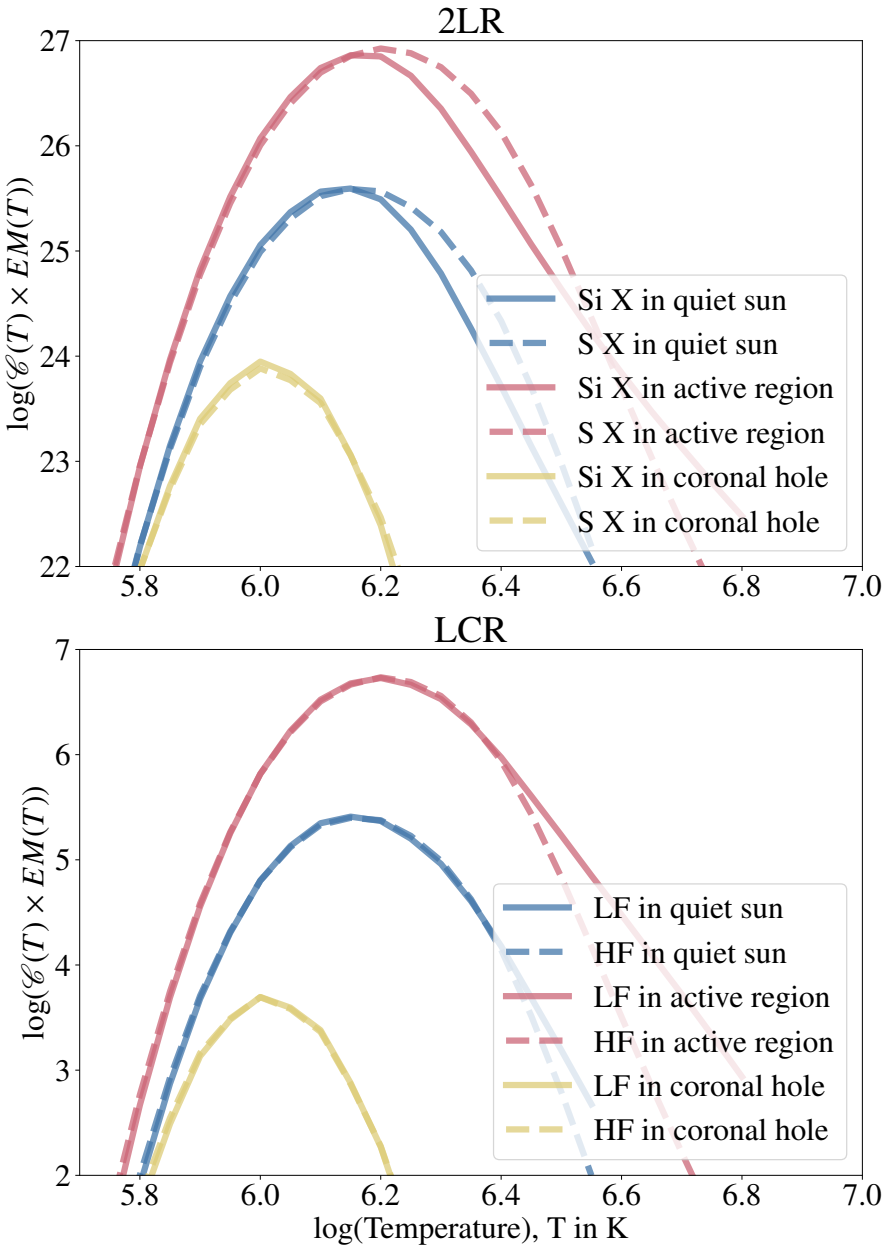

Figure 3.7: Products between the EM and the contribution functions ($\mathscr{C}_{\mathrm{LF}}$, solid lines, and $\mathscr{C}_{\mathrm{HF}}$, dashed lines), as functions of the temperature for both methods, using the coefficients in Table 3.1. Different colours correspond to different EMs from CHIANTI.

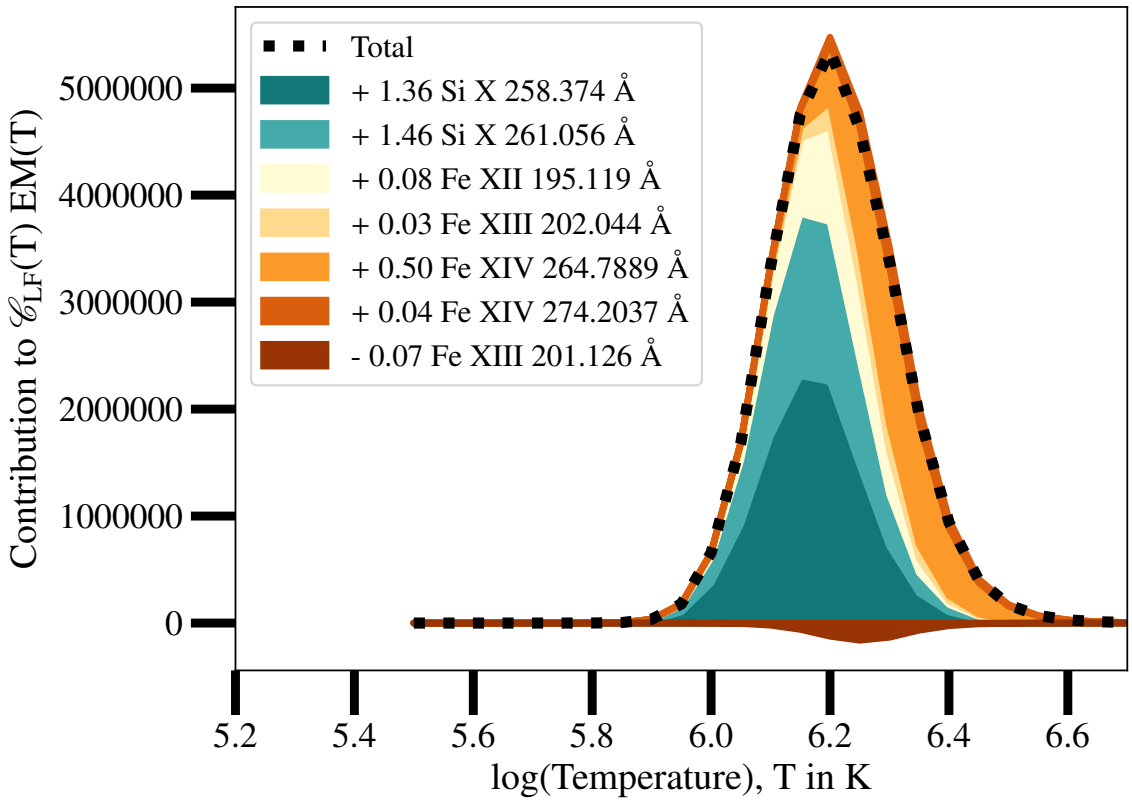

Figure 3.8: Contributions of the different spectroscopic lines to the $\mathscr{C}_{LF}(T)\,EM(T)$ product as a function of temperature for the CHIANTI AR EM. The total (dotted line) corresponds to the full red line in the bottom panel of Fig. 3.7. Here, Fe and Si line contributions are shown in ocher-red and blue-green colours, respectively. We separate the positive and negative contributions to the total.

After integration over T, the resulting $\langle \mathscr{C}, \mathrm{EM}_{\mathrm{AR}} \rangle$ is higher for S than for Si, corresponding to the fact that ψ_{AR} is 24% lower than 1 (see Table 3.3). This is consistent with the strong underestimation of the FIP bias that is obtained following this test in active regions with the 2LR method, as seen in Figs. 3.5 and 3.6.

In contrast, for the LCR method, the mean distance between the LF and HF curves in Fig. 3.7 is much smaller than for the 2LR method. This is measured, after integration over T, by the values of ψ_j in Table 3.3: these values are very close to 1.

Overall, this means that the LCR method performs better than the 2LR method in the range of temperatures including the peak of the mean coronal DEM.

COST FUNCTION RESIDUALS FOR REAL DEMS. The analysis of the cost function residuals in the previous paragraph is for the set of reference EMs that were chosen for the optimisation. However, the DEMs in the map are different. With real observations, we cannot measure the impact of this choice unless we perform a thorough DEM analysis, but this is not an issue in the case of the synthetic observations we produced for our tests in this section.

By applying Eq. (3.12) to the EM we used to produce synthetic radiances in every pixel, we can then retrieve the uncertainty linked to the arbitrary choice of reference EMs. In other words, we can determine through this calculation how far ψ_{EM} is from one for the EM in every pixel. As we can see in Eq. (3.13), this factor determines if we over- or underestimate the relative FIP bias. In both test regions, ψ_{EM} is 1 ± 0.01, meaning that in our case the impact on the FIP biases of the fact that the EMs in the map are not those chosen for the optimisation of the LCR coefficients is 1%. Therefore, the optimal linear combinations seem to be very well adapted to these EMs even though they were not optimised for them specifically.

USE OF DIFFERENT LOW-FIP ELEMENTS. As most values obtained in the test with the LCR method are between the relative abundance biases of Si (1.82) and Fe (2.05), one reason for the remaining non-uniformity in the maps could be the use of lines of LF elements with different abundance biases, while we assumed from Eq. (3.6) that they were the same. To assess this potential reason, we determine how much the spectral lines of each element are contributing to the total linear combination of LF elements in order to fit as best as possible to our HF line.

In our case, we show in Fig. 3.8 the respective contributions of the Fe and Si lines to the $\mathscr{C}(T)\,\mathrm{EM}(T)$ product for the LF linear combination of the LCR method and for the AR EM (for which the differences in the $\log T \in [6.2, 6.5]$ interval were most noticeable for the 2LR method, as discussed above). The relative contributions of the Fe and Si lines depend on temperature. This is true in this case, with the AR EM, but these

proportions will vary for different DEMs. As a result, for any given DEM, the FIP bias given by the LCR method will be closer to that of one element or the other, which can explain a part of the dispersion seen in the histograms of Figs. 3.5 and 3.6.

3.3 DETERMINING FIP BIAS FROM OBSERVATIONS

We applied the LCR method to spectroscopic observations of a sigmoidal anemone-like AR inside an equatorial CH that has previously been studied (including plasma composition) in Baker et al. [2013]. A full description of the evolution of this AR from the 11th to the 23rd October, 2007, including measurement of multi-temperature plasma flows, is presented in Baker et al. [2012]. We focus on a single raster observation lasting 2.25 hours that was carried out with the EIS spectrometer [Culhane et al., 2007] aboard Hinode [Kosugi et al., 2007] on October 17, 2007, at 2:47 UT.

Baker et al. [2013] used the method described in Sec. 2.4.2 in order to retrieve FIP bias maps. These latter authors used ten Fe lines in order to infer the EM from line radiances. They scaled this EM to accurately reproduce the radiance of the same Si X line that we used previously for the 2LR method (see Table 3.1). They then simulated the radiance of the same S X line that we used in the previous section and compared it to the observed radiance. The ratio gives a FIP bias map, reproduced in the left panel of Fig. 3.11.

In our analysis, we start by applying standard SolarSoftware EIS data-reduction procedures to the data, including correcting for dark current hot, warm, and dusty pixels, cosmic rays, slit tilt, CCD detector offset, and orbital variations. The obtained calibrated spectra were then fitted by single (or double, when necessary) Gaussian functions, and we computed integrated radiances for all lines.

We then selected the lines to be used for the LCR method, using the criteria from Sect. 3.1.3. This gives the five Fe lines, the two Si lines, and the S line listed in Table 3.1. We calculated the density of this AR using the Fe XIII λ 202.02 and 203.83 line pair diagnostic. This density map is plotted in Fig. 3.9. We then determined the optimal coefficients to use in each pixel using this map. In the case of this EIS observation, all the selected lines have strong radiances and are fairly isolated in the spectrum. However, among the EIS windows of this observation, only one line of an element considered as HF fits all our selection criteria. As a result, the set of HF lines is reduced to a single line (as in Sec. 3.2).

The results of the LCR method on this observation are presented in the right panel of Fig. 3.11. The FIP bias maps (from Baker et al. 2013 and from the LCR method) display similar FIP bias structures. The distributions of FIP bias values (bottom panels of Fig. 3.11) peak at 1.11 and 1.29. The correlation between both sets of values (Fig. 3.10)

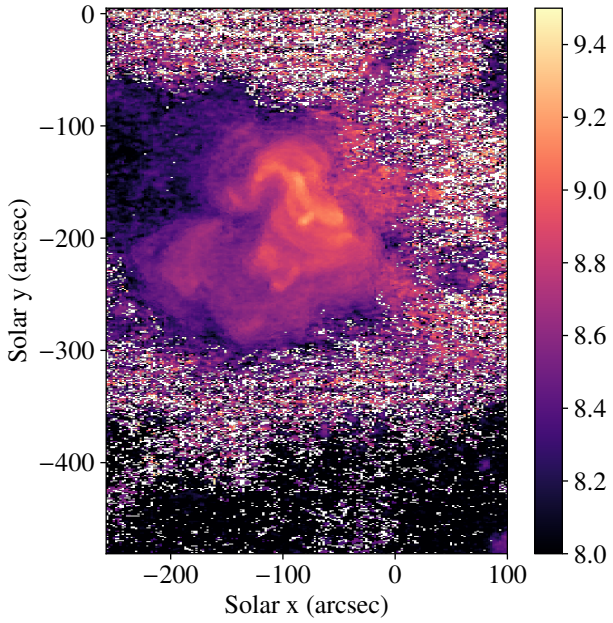

Figure 3.9: Map of the logarithm of the density in cm^{-3} obtained for the observation on October 17, 2007, from EIS spectra. We used the Fe XIII λ 202.02 and 203.83 line pair to calculate this density map. In the white pixels, fitting of the EIS lines failed. The density value of each pixel allows us to compute the optimal linear combination of lines to be used to determine the FIP bias in those pixels.

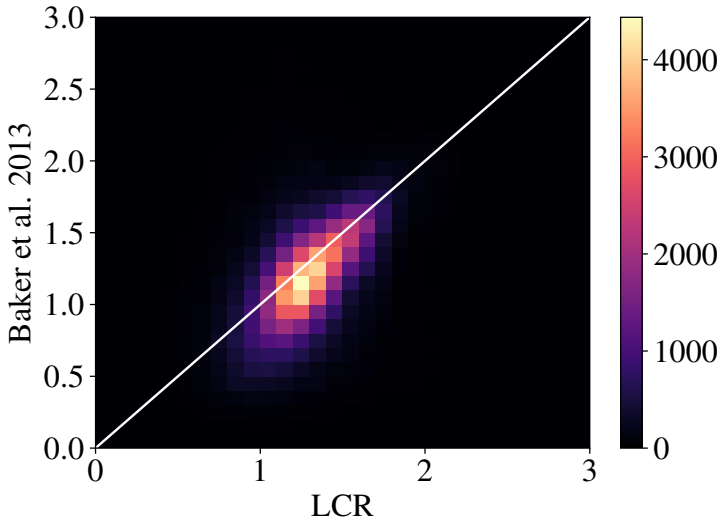

Figure 3.10: Two-dimensional histogram of the FIP bias values of Baker et al. [2013] and those obtained using the LCR method. The white line is the first bisector, where both values are equal.

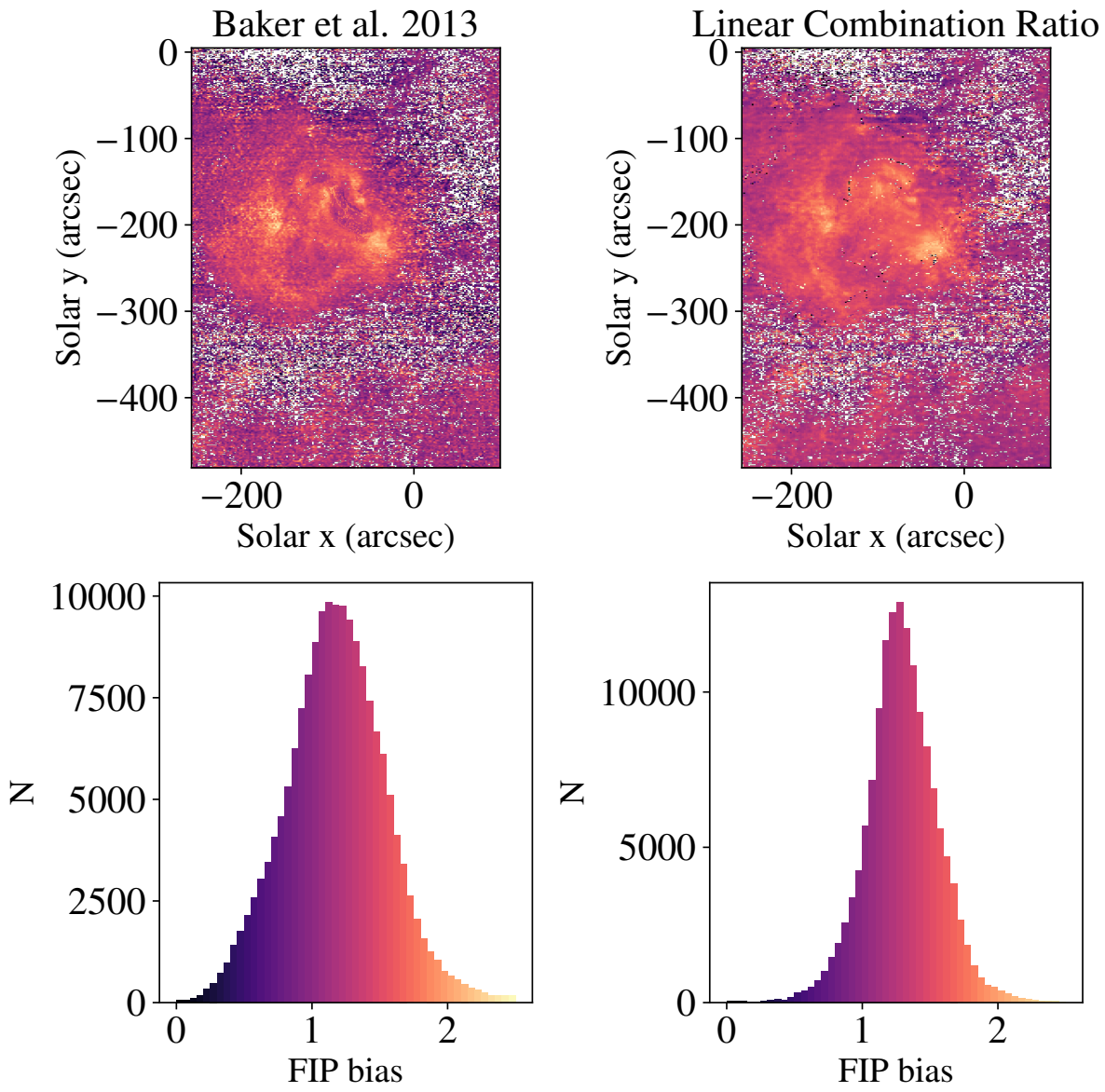

Figure 3.11: First ionization potential bias maps obtained with different methods and the corresponding histograms. The left panel shows the FIP bias map obtained following DEM inversion (adapted from Baker et al. 2013). The right panel shows the FIP bias map obtained using the LCR method. In the white pixels, the fitting of the EIS lines we performed failed. In both FIP bias maps we only plot the pixels where our fitting was successful.

also shows that the LCR values are higher overall than the Baker et al. [2013] values. However, we do not expect a perfect correlation as the real FIP bias values in this region are not known. We find that the LCR FIP bias map provides useful information on the FIP biases in the coronal structures in the field of view, which is remarkable given that it was produced without any DEM inversion.

3.4 DISCUSSION

Some sources of errors that could be identified from the non-uniformity in the test result in Sect. 3.2 have already been discussed in Sect. 3.2.4: the cost function residuals for the reference DEMs and for the real DEMs in the map, and the assumption that all LF (or HF) elements used have the same abundance bias. The cost function residuals for the real DEMs could be reduced by using a more comprehensive set of reference DEMs, or a set that would be more adapted to the observation; but the latter would require better knowledge of the DEMs in the observation, and we wanted to avoid inverting DEMs. The tests we have done show however that the residuals are in practice small for real DEMs given the set of three reference DEMs that we have chosen for the optimisation, and so this set is sufficient.

In regards to the mixing, in the same group (LF or HF) of spectroscopic lines from different elements with different abundance biases this is a matter of compromise. As one can see in Fig. 3.8, for the set of lines that we have chosen (the same as the ones available in the observation analysed by Baker et al. 2013 and re-analysed in Sect. 3.3), using only Si lines would not have allowed us to fit the LF and HF $\mathscr{C}_{\mathrm{LF}}(T)\,\mathrm{EM}(T)$ products, especially in the most relevant temperature interval (close to the DEM peak). The Fe lines provide a better fit, and subsequently a smaller value for the optimised cost function. This gives in the end a more accurate FIP bias determination, although the assumption that all abundance biases are the same for all LF or HF elements has not been verified; this must be checked on a case-by-case basis, depending on the elements giving the available spectral lines, along with their behavior with respect to the FIP effect.

As in any EUV spectroscopic analysis, other uncertainties come from radiometry (inaccurately measuring the line radiances, e.g. because of calibration or line blends), atomic physics (imprecise atomic data for computing the contribution functions; not taking into account effects such as those from non-Maxwellian distributions or from non-equilibrium of ionization, when required) and radiative transfer (opacity and scattering).

3.5 CONCLUSION

Here, we present the LCR method, developed with the aim to provide optimal determination of the relative FIP biases in the corona from spectroscopic observations without the need to previously determine the DEM. This technique relies on linear combinations of spectral lines optimised for FIP bias determination. We developed a Python module to implement the method that can be found at `https://git.ias.u-psud.fr/nzambran/fiplcr`.

Using two linear combinations of spectral lines, one with low FIP elements and another with high FIP elements, we tested the accuracy of the method performed on synthetic observations: these tests show that the method does indeed perform well, without prior DEM inversions. We then applied it to Hinode/EIS observations of an active region. We obtained FIP bias structures similar to those found in the same region by Baker et al. [2013] following a DEM inversion.

Once the optimised linear combination coefficients have been determined for a given set of lines, if radiance maps can be obtained in these lines, the LCR method directly gives the corresponding FIP bias maps, in a similar way to the 2LR method, but with better accuracy. This makes the method simple to apply on observations containing a pre-defined set of lines, with a potential for automation.

Hopefully, producing such FIP bias maps semi-automatically will allow non-specialists of EUV spectroscopy to obtain composition information from remote-sensing observations and compare it directly with in-situ data of the solar wind. This method could also allow better exploitation of observations not specifically designed for composition studies, and an optimal design of future observations. We plan to apply the method to the future Solar Orbiter/SPICE spectra to prepare the observations and analysis of the SPICE data.

APPENDIX

3.A DENSITY DEPENDENCE

As mentioned in Sect. 3.1.3, following the density-dependence of the contribution functions, the coefficients of the linear combinations also depend on density. We traced the resulting value of ψ as a function of density from Eq. (3.12) for the 2LR method in Fig. 3.A.1 and for the LCR method in Fig. 3.A.2. We perform the calculations using the three typical EMs from CHIANTI mentioned above and plotted in Figs. 3.2 and 3.3. The variable ψ represents the ratio of the radiances of the linear combinations of spectral lines if the FIP biases would be 1. The goal of the optimisation in the LCR method is to have ψ be as close to 1 as possible, so that the relative FIP bias is given by the ratio of the linear combinations of spectral lines as defined in Eqs. (3.1) to (3.6).

As we can see in Fig. 3.A.1 (and consistent with the values of Table 3.3 at $\log n = 8.3$), the 2LR method gives values of ψ that can be up to 20% above or below the target value of 1, leading to erroneous FIP bias determination. The ψ value for each EM depends somewhat on density as well. In contrast, the LCR method (Fig. 3.A.2) yields ψ values that are less than 0.7% away from 1 at all densities, leading to much more accurate FIP bias determination than with the 2LR method.

We then trace ψ in Fig. 3.A.3 using only the coefficients computed for the LCR method at a fixed density of $\log n = 8.3$ and the contribution functions evaluated at different density values. We do so to determine the error one would commit by assuming a constant density of $\log n = 8.3$ when determining the optimised coefficients (listed in Table 3.1) instead of using the density-dependent approach. In this case, ψ remains within 20% of the target value of 1 from below $\log n = 7$ to $\log n = 9$, meaning that the LCR method can perform as well as or better than the 2LR method in a significant range of densities, even when not taking the density dependence of the optimal coefficients into account. However, ψ deviates strongly from 1 for higher densities, up to a factor two if $\log n = 11$ instead of 8.3.

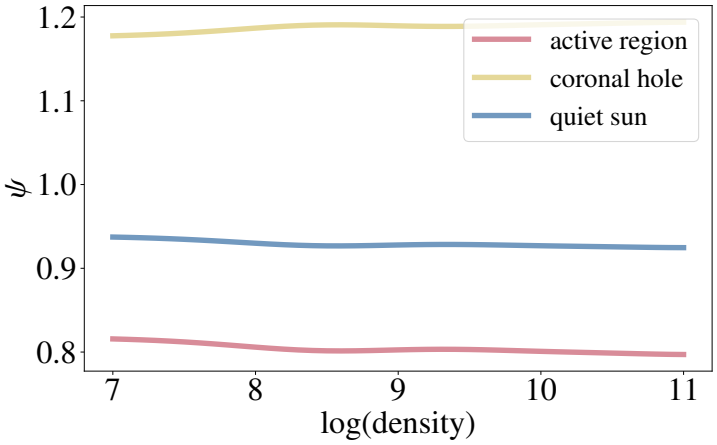

Figure 3.A.1: Value of ψ from Eq. (3.12) as a function of density for each typical EM from CHIANTI for the lines used in the 2LR method. The coefficients used to calculate ψ for every density value are defined by Eq. (3.14). The black lines correspond to the values of $\log n = 8.3$ for the abscissa and $\psi = 1$ for the ordinates.

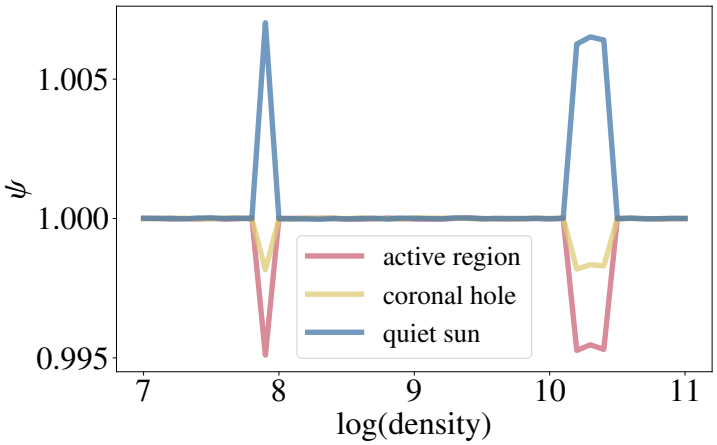

Figure 3.A.2: Value of ψ from Eq. (3.12) as a function of density for each typical EM from CHIANTI for the linear combinations of lines used in the LCR method. The coefficients used to calculate ψ for every density value are the result of the optimisation. For example, the coefficients used for every line at log(n)=8.3 are the ones listed in Table 3.1.

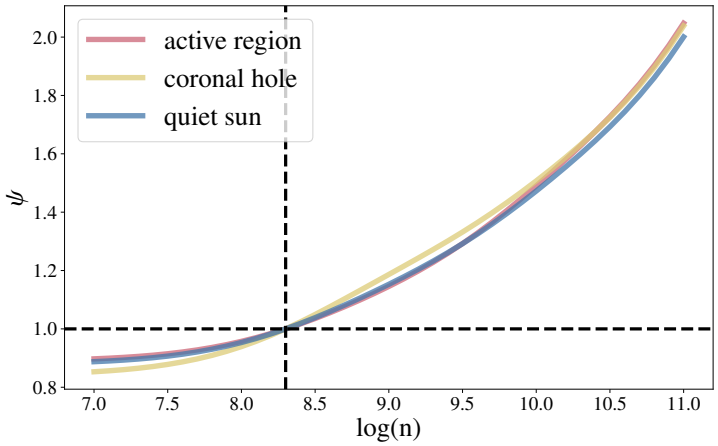

Figure 3.A.3: Value of ψ from Eq. (3.12) as a function of density for each typical EM from CHIANTI for the linear combinations of lines used in the LCR method. This time we use the coefficients listed in Table 3.1 computed at a fixed density of $\log n = 8.3$ and the contribution functions are evaluated at the different density values. The dashed lines correspond to the density value assumed for the optimisation, and to the target value of ψ.

4

ON THE ACCURACY OF THE LCR METHOD

Aims. *The LCR method is based on optimised linear combinations of spectroscopic lines of low-FIP and high-FIP elements that have coefficients such that the ratio of the corresponding radiances yields the relative FIP bias with good accuracy. We aim to determine the uncertainty of any given such combination.*
Methods. *We use a statistical approach based on the Bayes theorem so that we can define the likelihood of the plasma's real relative FIP bias given the inferred relative FIP bias obtained with the LCR method. We present a numerical protocol for determining uncertainties for our measurements based on this conditional probability.*
Results. *We give an example applied to linear combinations of spectral lines observable the EUV imaging spectrometer (EIS) on-board Hinode.*
Conclusions. *Using this statistical approach, we can define the uncertainties linked to the diagnostics made using the LCR method. These uncertainties can be computed using different noise models and tailored to the instrument used and the observations' specificities.*

4.1 INTRODUCTION

We have seen that it is possible to obtain relative FIP bias measurements using the LCR method. The tests that we performed were done using radiances of spectral lines but we did not take into account the effects that noise can have on our relative FIP bias diagnostics. We will now focus on measuring the uncertainty of the method, taking the characteristics of the instrument and noise into account. After obtaining

a measurement of the relative FIP bias using the LCR method, we wish to evaluate the likelihood of the plasma having a given relative FIP bias knowing the result of the measurement. This can be achieved by determining the probability distribution of the possible relative FIP biases of the plasma knowing that the abundance diagnostics has resulted in a given value. We will use a statistical method based on Monte-Carlo simulations and Bayes' theorem similar to the techniques developed for DEM inversions by Guennou et al. [2012a].

We illustrate our methodology in the specific case of a set of spectral lines observable by the EUV imaging spectrometer [EIS; Culhane et al., 2007] on-board Hinode [Kosugi et al., 2007] but the same calculations can be performed for any other combination of lines observable by any other spectrometer, provided we have a model for the instrumental calibration and noises. Modules and tools to do so will be provided in the `fiplcr` Python module that we had previously developed for computing the optimized coefficients for the linear combinations.

4.2 THE LCR METHOD AND CONDITIONAL PROBABILITIES

We will denote I_{ij} the radiance of an optically thin spectral line at wavelength λ_{ij} corresponding to the transition $j \rightarrow i$ of the X^{+m} ions. We will call them our radiances of reference. When observing the corona with a spectrometer, the number of photons detected in a pixel of our instrument will depend on its sensitivity which can be summarized in its effective area $A_{eff}(\lambda)$, a function of the observed wavelength, but also on other characteristics of the observation such as the exposure time and the solid angle observed which accounts for the angular size of a pixel and that of the slit used. These observations are affected by measurement noises and by systematic errors. Some examples of random errors are photon shot noise, which has a Poisson distribution, and detection noises such as thermal and read noise, which can usually be considered Gaussian. Systematic errors may come from the calibration of the instrument. We will call these radiances affected by noises and uncertainties of the instrument calibration I_{ij}^{obs}. Determining the relative FIP bias between low FIP and high FIP elements using the LCR method consists in:

- Choosing a set of spectral lines from low FIP (LF) elements and another set from high FIP (HF) elements.

- Optimizing the coefficients of the linear combinations of each set of lines so that Eq. (3.11) is as close to zero as possible and Eq. (3.13) is verified.

- Computing the relative FIP bias between the LF and the HF elements through the ratio of the two radiance-like quantities defined in Eqs. (3.1) & (3.2), $\mathscr{I}_{\mathrm{LF}}$ & $\mathscr{I}_{\mathrm{HF}}$.

The observed radiances I_{ij}^{obs} can be affected by noises and systematic errors of instrument calibration, so these are to be taken into account when determining the uncertainty of a measurement carried out using the LCR method. The LCR method can be additionally affected by systematic errors concerning atomic physics, the optimisation is done assuming a given contribution for each spectral line and the atomic physics used to compute such contribution functions can be affected by these errors. Therefore, the LCR method can yield different inferred relative FIP biases for a given relative FIP bias of the plasma. We will denote f_i and $f_p = \dfrac{f_{\mathrm{LF}}}{f_{\mathrm{HF}}}$ respectively the inferred relative FIP bias and the relative FIP bias of the plasma.

We want to know the likelihood of the plasma having a relative FIP bias f_p knowing that our measurements yield f_i. This means that the quantity we truly want to evaluate with our analysis is the posterior probability distribution $P(f_p \mid f_i)$. Since several different f_p can potentially yield the same f_i, the derivation of $P(f_p \mid f_i)$ requires us to know $P(f_i)$, the total probability of obtaining f_i no matter the value of f_p:

$$P(f_i) = \int P(f_i \mid f_p) P(f_p) \mathrm{d}f_p, \tag{4.1}$$

where $P(f_i \mid f_p)$ is the probability of obtaining f_i given f_p and $P(f_p)$ is called the prior probability in this framework. The prior allows to take into account the available prior information. If no information is available on how the f_p values might be distributed, we can adopt an uninformative prior which expresses objective information allowing us to rule out non-physical solutions such as negative relative FIP biases for the plasma for example. Bayes' theorem gives:

$$P(f_p \mid f_i) = \frac{P(f_i \mid f_p) P(f_p)}{P(f_i)}, \tag{4.2}$$

which is the conditional probability that the plasma has a relative FIP bias of f_p given that we have obtained f_i through the LCR method with the noisy radiances I_{ij}^{obs}. By evaluating this conditional probability, we will be able to more accurately distinguish between plasma where the FIP effect has taken place and plasma where it has not, given the underlying uncertainties.

4.3 IMPLEMENTATION

We will start by describing a very general implementation scheme summarized in Fig. 4.3.1 that can be useful for any given spectroscopic instrument. We will then

present a simple example where we will assume Gaussian noise to see the general trends we can expect when measuring relative FIP biases with the LCR method. For a deeper dive into noise simulation and the consequences different types of noise can have on these types of measurements see Sec. 6.3. There we perform more realistic simulations of noise for the EUV spectrometer on board Solar Orbiter, SPICE.

As we have seen in the previous section, the quantity we want to evaluate is $P(f_p \mid f_i)$, the conditional probability that the plasma has a relative FIP bias of f_p given that our measurements yield a value of f_i. We can, in principle, determine $P(f_i \mid f_p)$ and then $P(f_p \mid f_i)$ through Monte-Carlo simulations. The procedure one would follow in the case of the LCR method can be summarized in only a few steps, as described in Fig. 4.3.1,:

- Choose a probability distribution of f_p. If we have no information about how f_p might be distributed at the surface of the Sun at any time, we can assume $P(f_p)$ to be uniformly distributed. One could for example adopt a window function for $P(f_p)$ that excludes non physical values such as negative relative FIP biases.

- Compute synthetic radiances I_{ij} for all the spectral lines that will be used for the relative FIP bias diagnostic. This can be done by choosing a DEM and by computing the contribution functions of every spectral line with an atomic database. The DEM should be, if possible, different from the ones used to do the optimisation of the LCR coefficients. This allows to test a more realistic case where the EM of the observed plasma is not a textbook case.

- From the synthetic radiances and instrumental model, simulate noisy radiances I_{ij}^{obs} as would be measured by the instrument. We use Monte-Carlo simulations for this purpose. When using a spectrometer, we can add in at this point photon shot noise, detection noises, an estimation of the systematic errors brought in by the calibration of the instrument and also, in the case of the LCR method, we can include here errors linked to atomic physics. For every f_p we will do N realizations of all necessary random variables to account for all the types of errors we want to simulate. This will yield N different pseudo radiance pairs $(\mathscr{I}_{LF}, \mathscr{I}_{HF})$ for a single f_p value.

- From the noisy pseudo radiances, measure relative FIP biases using the LCR method. Every f_p value will yield N measurements f_i.

- From this sample of N f_i's for every f_p, evaluate $P(f_i \mid f_p)$, then $P(f_i)$ and finally $P(f_p \mid f_i)$ using Bayes' theorem.

This scheme can be applied to any particular linear combination of spectral lines and can be tailored to any instrument when simulating noise.

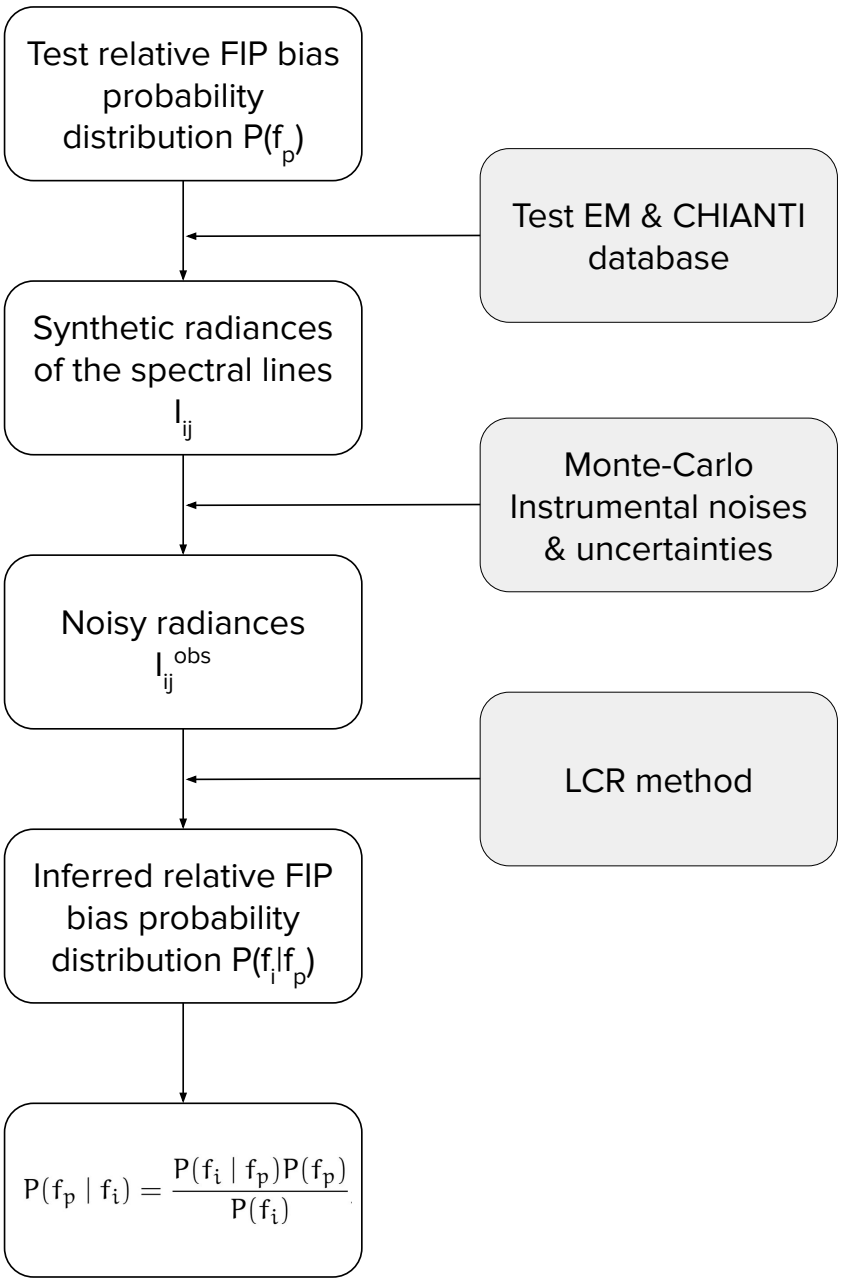

Figure 4.3.1: Schematic representation of the procedure followed. For a given distribution of relative FIP biases (f_p) we compute the corresponding radiances of a set of spectral lines emitted by low FIP and high FIP elements. These radiances are computed using a test EM and contribution functions obtained with the CHIANTI database. Noise is added to these radiances in the form of random variables. Using the LCR method, we obtain inferred relative FIP biases (f_i). The probabilities $P(f_i \mid f_p)$ and $P(f_p \mid f_i)$ are built from a large number of draws of the random variables.

Table 4.3.1: Spectral lines used to perform the calculations. The coefficients result from the optimisation. These coefficients were calculated for a density of log(n) = 9.3.

Ion	Wavelength (Å)	$\log T_{max}$ (K)	LCR coeff
Fe XIII	202.044	6.2	0.164
Si X	258.374	6.1	0.691
S X	264.231	6.2	1.00
Fe XIV	264.789	6.3	0.117

4.3.1 *An example: using spectral lines observable by Hinode/EIS*

The spectral lines we use in this example are listed in Table 4.3.1. These lines are observable by the EIS spectrometer. We use a set of 3 lines from low FIP elements iron and silicon and we use a single line of sulfur as our high FIP element. We assume a constant density of 2×10^9 cm^{-3} for all the regions to calculate the contribution functions $C(T, n_e)$ of the lines. We determine the optimal linear combination of these lines for the LCR method and depict the reference EMs used for the optimisation in Fig. 4.3.2 (blue, red and yellow curves). The coefficients obtained are presented in Table 4.3.1. We perform the tests thoroughly described in Sec. 3.2 using the same AR and CH EM cubes (see Figs. 3.1, 3.2 & 3.3) as well as the same abundances (see Table 3.2). The results of these tests are presented in Fig. 4.3.3.

From these tests we can see that the FIP bias maps we obtain are rather uniform, with both histograms peaking at 1.88, well in between the values of relative FIP bias that we imposed, and with standard deviations of less than 0.02. The LCR results are very close to the imposed FIP biases in both regions even though their EMs are very different. We conclude that these lines are good candidates for relative FIP bias diagnostics.

We now apply the scheme described in Fig. 4.3.1 to this set of spectral lines. We explore a wide range of possible relative FIP biases for our plasma going from 0 to 5 and varying in steps of 0.05. As our prior $P(f_p)$ we adopt a window function that is uniform in the [0, 5] interval and zero elsewhere, as depicted in red in Fig. 4.3.5. This is an arbitrary choice, the impact of changing the size of this interval will be discussed in Sec. 4.4.

For every relative FIP bias value f_p we synthesize the radiances of the lines listed in Table 4.3.1. We can see in Fig. 4.3.2 that the EM we use to synthesize radiances (black line) does not span the same temperature range as the ones we used for the

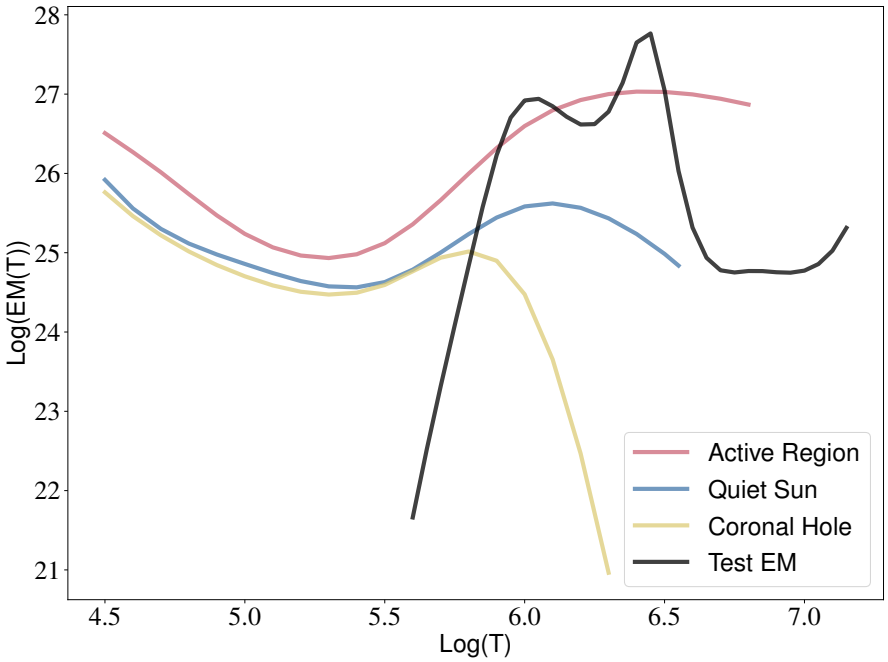

Figure 4.3.2: In colored lines we plotted the typical EMs from CHIANTI that we use to optimise the cost function (see Eq. (3.11)). The red line corresponds to an active region, the blue line to the quiet Sun and the yellow line to a coronal hole. The black line corresponds to the EM that we use in this section as a test EM to produce synthetic radiances. It is an AR EM provided to us by Susanna Parenti [Parenti et al., 2017] corresponding to an AR observed off-limb.

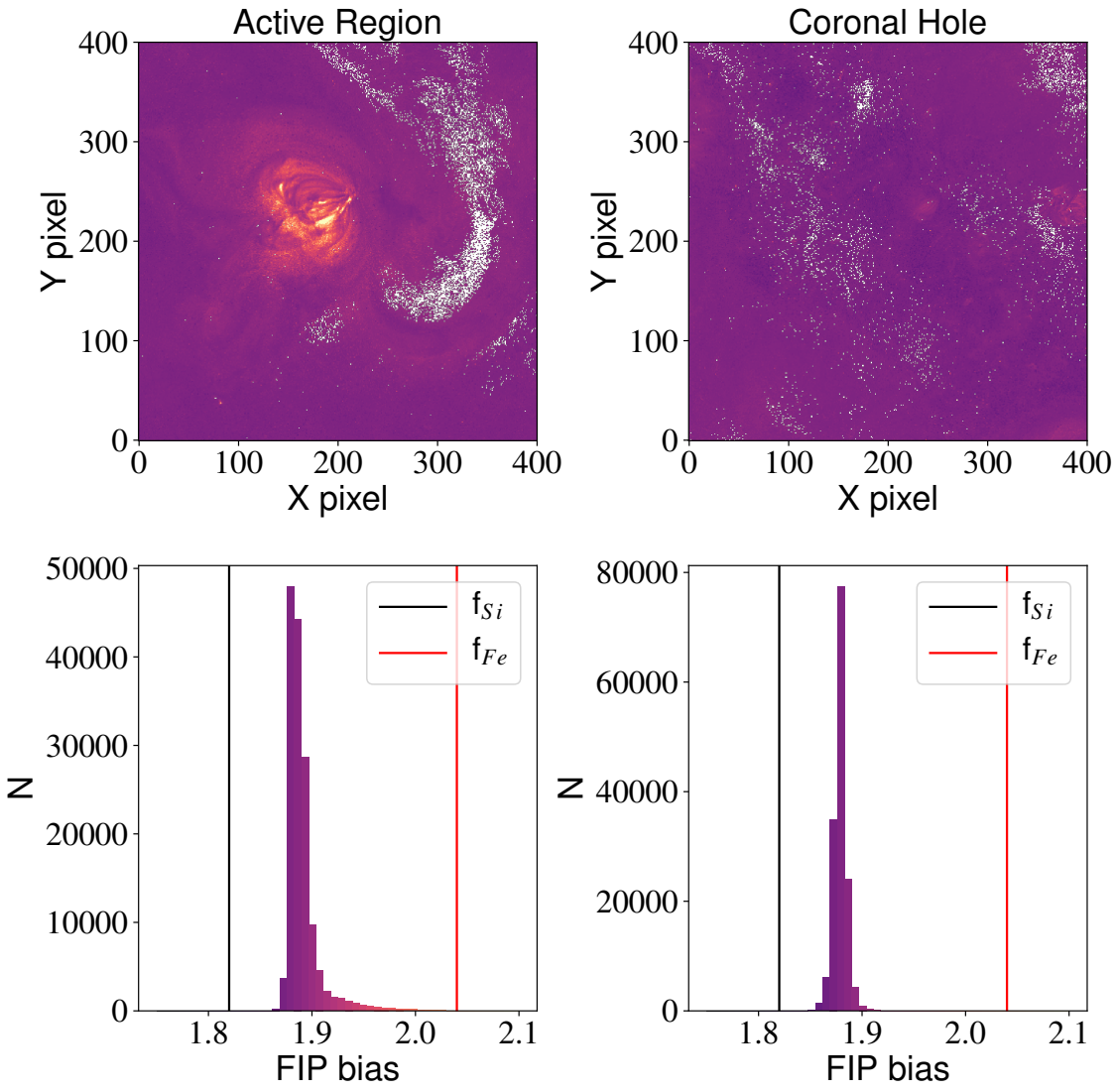

Figure 4.3.3: Results of the relative FIP bias determination using the LCR method following the tests of Sec. 3.2 (top) and their corresponding histograms (bottom), with matching color scales. The vertical lines in the histograms correspond to the imposed uniform values of the relative FIP bias (for each of the low-FIP elements; see Table 3.2) that should ideally be retrieved. On the left we applied the LCR method to radiances synthesized from the EM of an active region (see black square in Fig. 3.1) and on the right from that of a coronal hole (see red square in Fig. 3.1).

optimisation and also has a more complicated shape. These calculations yield our set of radiances I_{ij} of reference.

Using Monte-Carlo simulations we draw a big number of random variables that will be added to the radiance values previously calculated to simulate noise. For this very simple example we will model our noise as Gaussian random perturbations with a 20% standard deviation assuming that this would be a typical error one would obtain for the radiance of EIS observations. This means that we simply need to draw one set of random variables for each spectral line. When using more sophisticated models for the noise, we would have to draw the same amount of random variables for every type of noise we consider. A more detailed example of this process will be described in the next chapter.

For every f_p, we draw 40 000 I_{ij}^{obs} for every spectral line listed in Table 4.3.1. This yields 40 000 pairs of ($\mathscr{I}_{LF}$, $\mathscr{I}_{HF}$). Using the LCR method we hence infer 40 000 relative FIP biases f_i for all the simulated data. For convenience, and to easily visualize the results of the simulations, we will show them as images of 200 by 200 pixels. We show a comparison between a uniform radiance map and an example of a noisy map in the left panels of Fig. 4.3.4. This particular example was made with the Si X λ 258.374 Å line. Using the LCR method we will infer the relative FIP bias for each of the 40 000 draws for each f_p. We can see two different examples of the f_i maps we obtain in the right panels of Fig. 4.3.4. The top panel shows the case of $f_p = 1.0$ and the bottom that of $f_p = 5.0$.

We can now determine the conditional probability that the plasma has a given f_p for any of the relative FIP bias values f_i that we obtain with our diagnostic.

4.3.2 *Obtained probability distributions*

From the histogram of the inferred relative FIP bias values f_i for every imposed value of f_p we obtain the probability distribution of obtaining f_i knowing f_p, $P(f_i \mid f_p)$. We show examples of the conditional probability $P(f_i \mid f_p)$ of obtaining f_i knowing f_p for f_p in [1, 2, 3, 4, 5] in Fig. 4.3.6 and the full probability distribution in Fig. 4.3.7 for all the f_p values.

The examples of Fig. 4.3.6 correspond to vertical cuts in Fig. 4.3.7. As we can see the peak of the probability distribution of each value is near the imposed value f_p. The distributions flatten out as the f_p increases. This is in accordance with the fact that we assume a 20% error on the radiances.

We obtain $P(f_i)$ by integrating $P(f_i \mid f_p)$ over all possible f_p through equation (4.2). It's the probability distribution of obtaining a measurement of f_i no matter the initial f_p. For comparison, we display this curve together with our prior $P(f_p)$ that we had

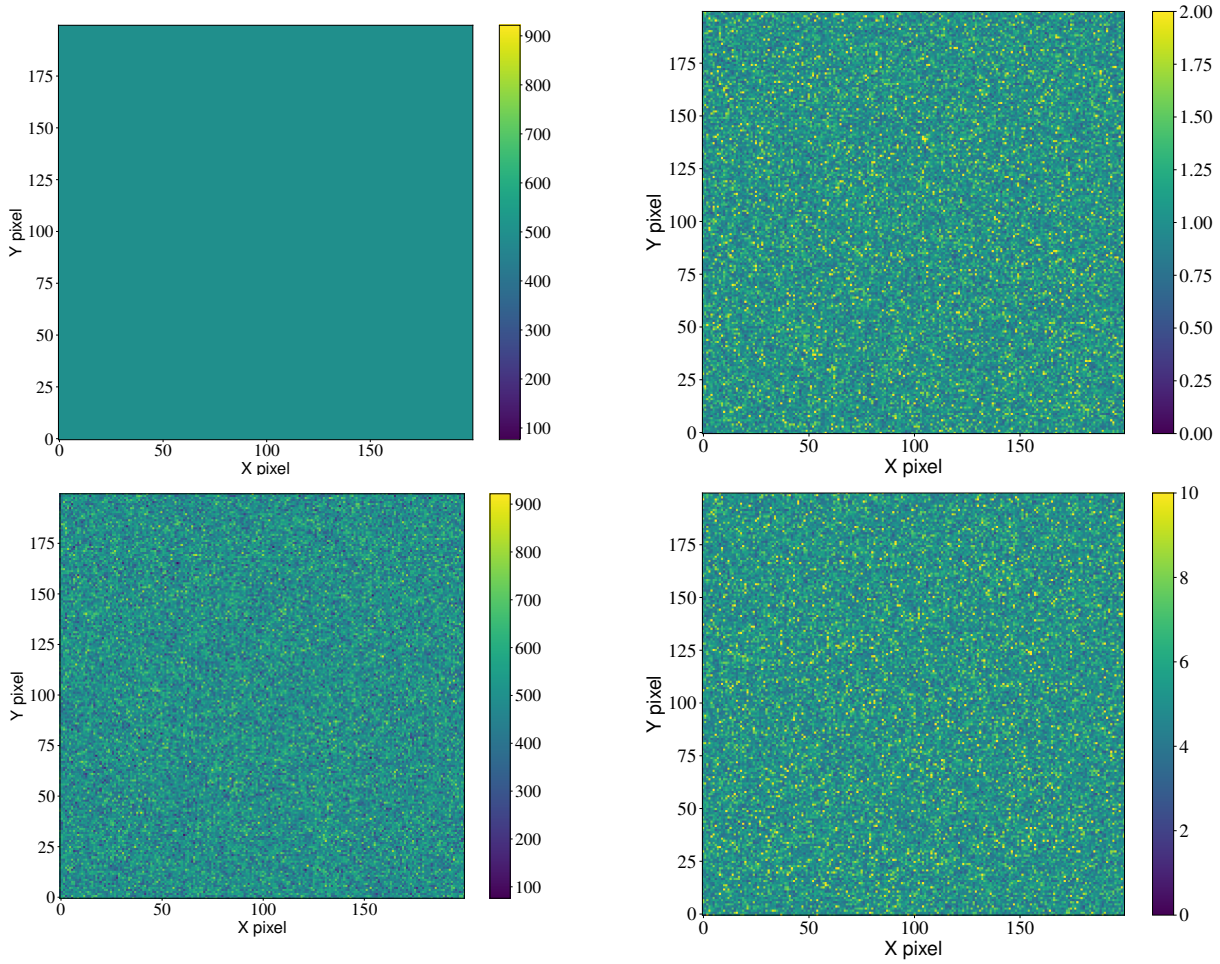

Figure 4.3.4: The top left panel shows a uniform map of 200 by 200 pixels of the radiance of the Si X line (4.3.1) in erg.cm^{-2}.s^{-1}.sr^{-1}. It was synthesized using the CHIANTI data base for the contribution function, an abundance of 10^{-5} and the EM 'Test EM' depicted in Fig. 4.3.2. From this map we computed the 200 by 200 pixel map in the bottom panel. Every pixel corresponds to the result of adding random noise to the previously computed radiance. We added Gaussian random perturbations with a 20% standard deviation assuming that this would be a typical error bar one would obtain for the radiances of EIS observations. Right: From the noisy radiance maps obtained for all spectral lines in Table 4.3.1 we compute the relative FIP bias one would obtain by applying the LCR method in each pixel. We do this for an array of relative FIP bias values going from $f_p = 0.0$ to $f_p = 5.0$. We show examples of such relative FIP bias maps in this figure. On the top, we computed the radiances assuming a relative FIP bias of 1.0 and on the bottom of 5.0.

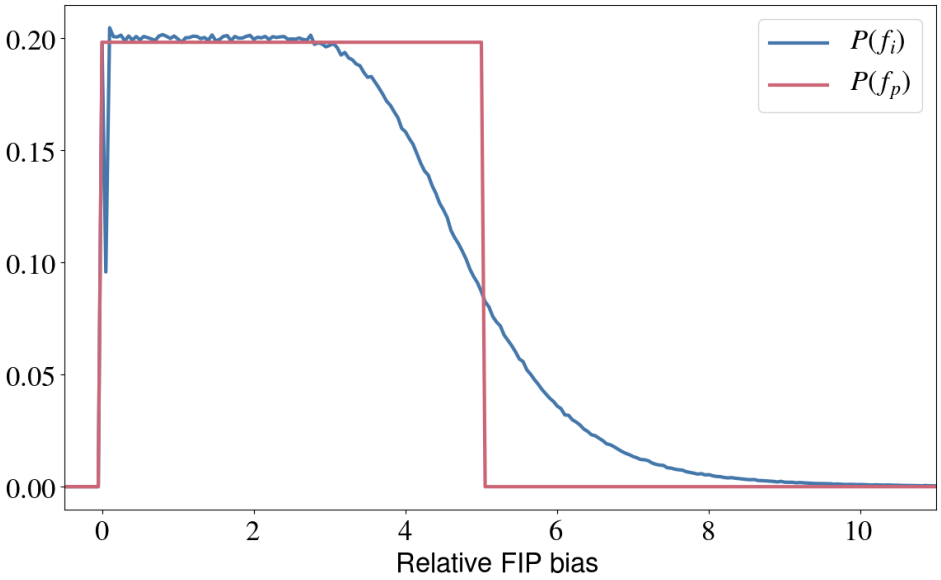

Figure 4.3.5: Probability distribution $P(f_i)$ of obtaining a certain inferred relative FIP bias through the LCR method without knowing the imposed relative FIP bias in blue. Obtained for f_p varying from 0.0 to 5.0 with a prior probability distribution $P(f_p)$ in red that is uniform.

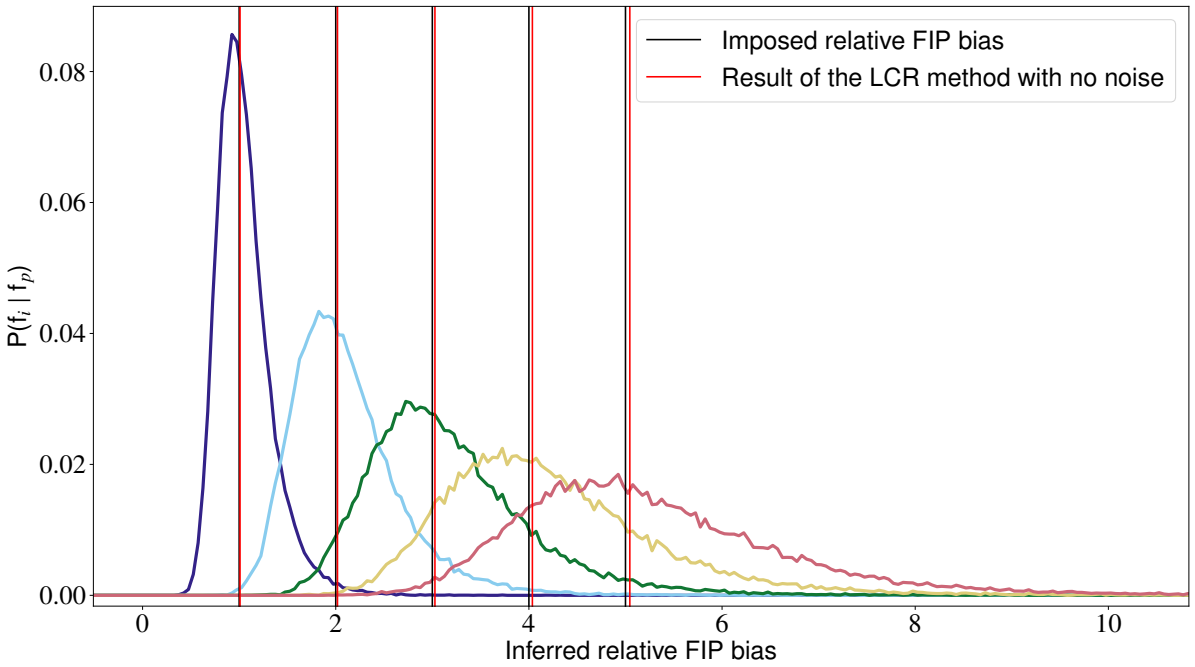

Figure 4.3.6: Examples of the probabilities of inferred relative FIP biases knowing the imposed relative FIP bias. The colored curves show the probability distributions for 5 different imposed relative FIP bias values. We zoomed on the areas where values were most probable. From left to right, we see the probability distribution curves for $f_p = 1,\ 2,\ 3,\ 4$ & 5. The black vertical lines show the imposed relative FIP bias. The red vertical lines show the result of applying the LCR method to the radiances directly, with no noise involved.

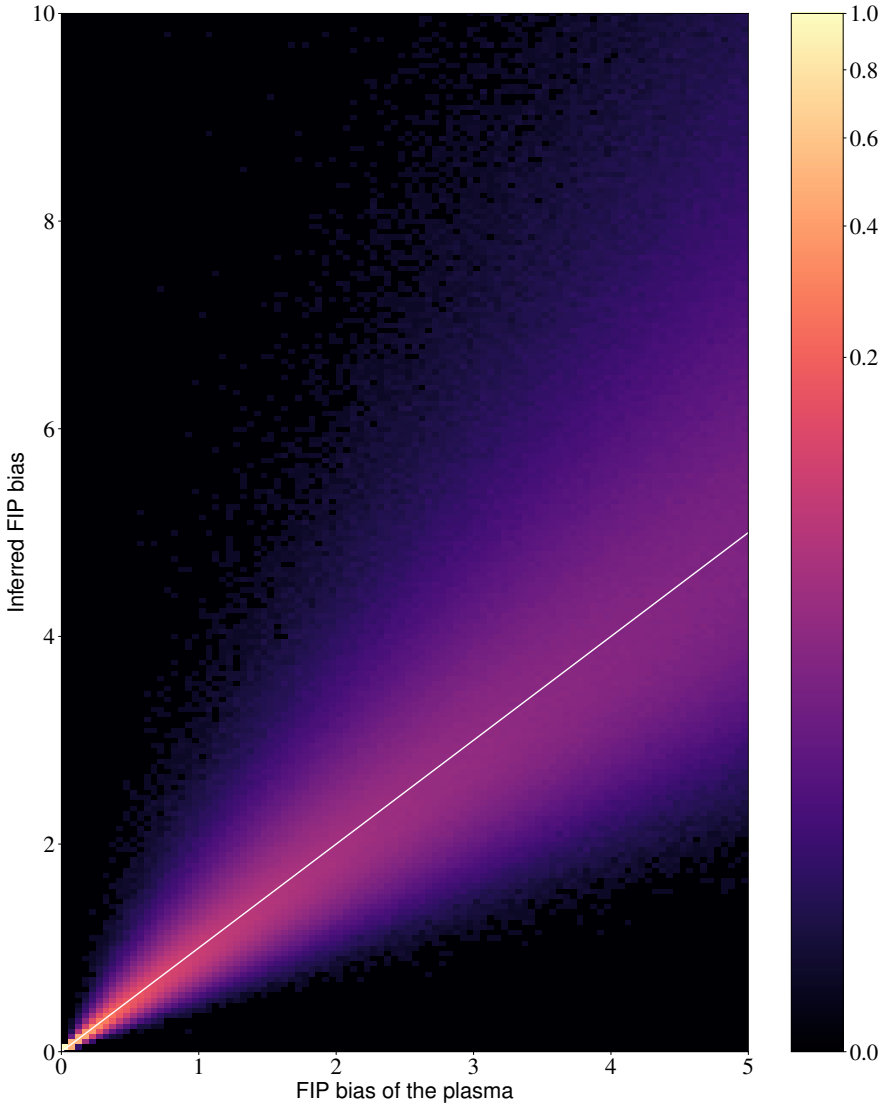

Figure 4.3.7: Conditional probability $P(f_i \mid f_p)$ of obtaining, on the ordinates, an inferred FIP bias f_i knowing the imposed relative FIP bias value, on the abscissa. The color of a pixel of ordinate y and abscissa x corresponds to this probability. The white line is the first bisector, where both values are equal. We zoomed on this particular area because inferred relative FIP bias values above 10.0 or under 0.0 are rare (<0.2% of the total sample).

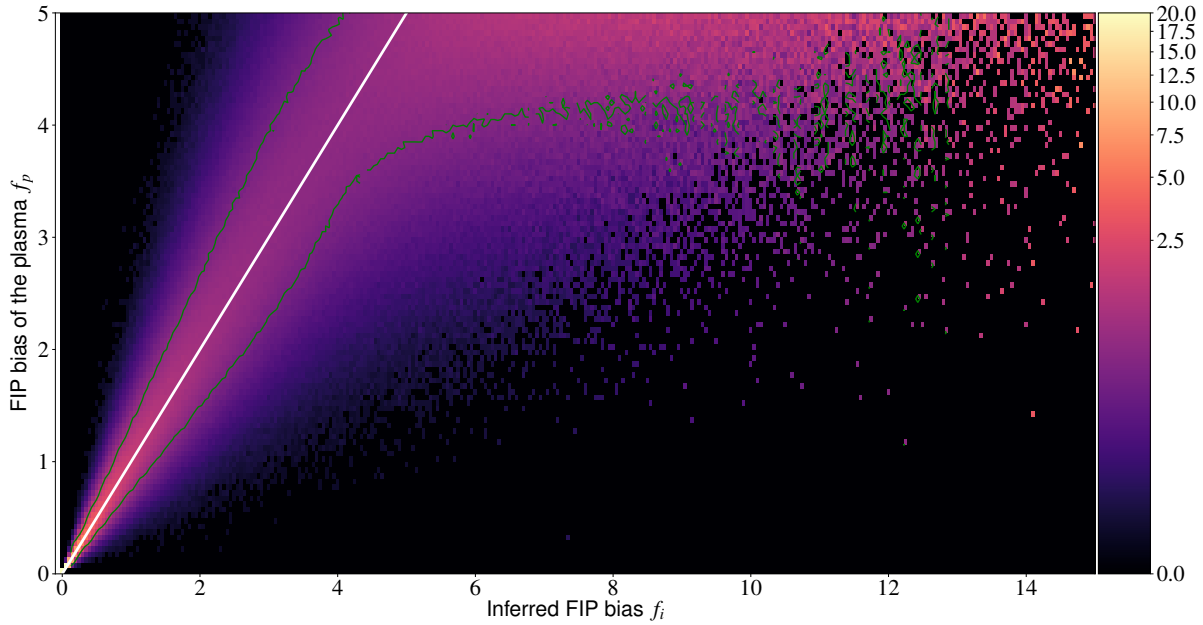

Figure 4.3.8: Conditional probability of the plasma having, on the ordinates, a given relative FIP bias (f_p) knowing the inferred relative FIP bias obtained from observations (f_i), on the abscissa, using the LCR method on the spectral lines listed in Table 4.3.1. Probability distribution obtained for f_p varying from 0.0 to 5.0 and a prior probability distribution $P(f_p)$ uniform between 0 and 5. The white line is the first bisector, where both values are equal. The green contour corresponds to the 75% credible interval computed for each value of f_i.

shown in Fig. 4.3.5. Finally, we compute $P(f_p \mid f_i)$ using Eq. (4.2), this conditional probability map is shown in Fig. 4.3.8.

4.3.3 *Determining uncertainties*

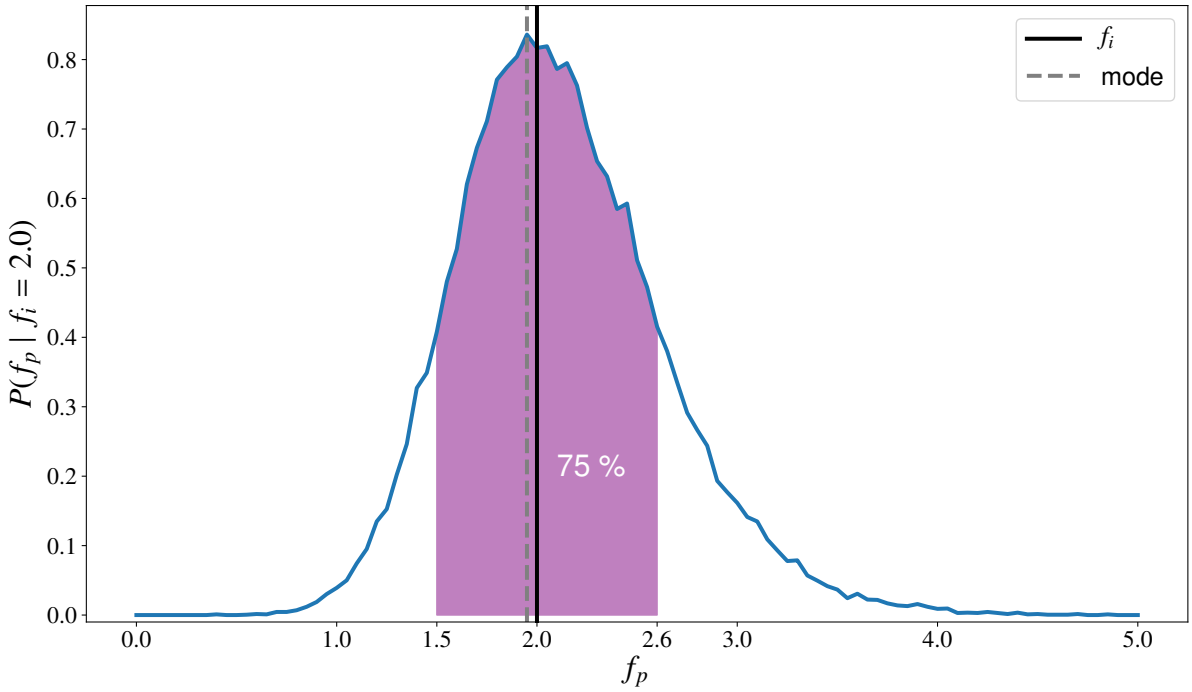

Figure 4.3.9: Conditional probability distribution $P(f_p \mid f_i = 2.0)$ using the LCR method on the spectral lines listed in Table 4.3.1. For every vertical cut in Fig. 4.3.8, the two ordinates defining the position of the green contour correspond to the two boundaries of the purple area depicted here. This area corresponds to the 75% credible interval (or the highest posterior density interval). The black line corresponds to the inferred f_i. The grey dashed line corresponds to the mode of the distribution, i.e. the maximum a posteriori.

In Fig. 4.3.9 we show the conditional probability distribution $P(f_p \mid f_i)$ for $f_i = 2.0$ as an example to explain how we determine the uncertainties using the posterior distribution we obtained through our procedure. In Fig. 4.3.8 we defined the green contour as the credible interval. In our case, we chose an interval within which f_p falls with a 75% probability. We chose the narrowest possible interval, often also called the highest posterior density interval. Fig. 4.3.8, the two ordinates defining the position of the green contour correspond to the two boundaries of the purple area depicted in Fig. 4.3.9. This indicates which points of a distribution are most credible, and which cover most of the distribution. This means that every point inside this interval has a higher credibility than any point outside of it. In this case, the interval was computed such that it spanned over 75 % of the distribution, it can be computed for any other

value as well. We define our uncertainties from the the boundaries of the credible interval. In this example, the LCR method gave $f_i = 2.0$, the most probable f_p value is slightly lower and f_p is most likely in the interval [1.5, 2.6].

4.4 DISCUSSION

We have been able to develop a way to measure the uncertainties of the LCR method. It can take into account the different kinds of noise and systematics provided we have a model for the instrumental calibration and noises. It can also take into account the uncertainties associated with the assumptions we make when using the LCR method (e.g. the atomic physics used to compute contribution functions). Through Bayes theorem, we can obtain a probability distribution for the plasma we are observing given the inferred FIP bias f_i.

One of our main assumptions here is our prior $P(f_p)$. We adopt a window function that is uniform in the [0, 5] interval and zero elsewhere. We had initially used a prior that was uniform in the [1,5] interval but realized that it excluded the inverse FIP effect which can take place at the Sun [Baker et al., 2019, 2020]. This prior is an arbitrary choice, it does exclude non physical values such as the relative FIP bias being negative, but it does not bring that much more information. Widing and Feldman [2001] studied various regions presenting magnetic flux emergence over a week and found that the Mg/Ne abundance ratio of a newborn AR is photospheric, but as time passed, this ratio would increase within the AR. After two to three days, they found an enhancement of the FIP bias of 4.8. The bias increased further as days went on. Other studies have found old ARs to have even higher relative FIP biases [Young and Mason, 1997, Dwivedi et al., 1999]. This means that, if we are observing ARs, the prior can go well beyond 5 as our maximum value. This is a parameter that can easily be changed in the code. However, we do not have a clear idea of what the actual probability distribution of relative FIP biases in the solar corona is. We know that the Sun overall has more FIP effect than inverse FIP effect but we do not know in what proportion we have photospheric or coronal FIP biases. Furthermore, these proportions can change with the solar cycle, we will have more ARs and more activity in general during solar maximum but the interaction between ARs might also impact the FIP effect. For the moment, we will continue using uniformly distributed priors, adapting the maximum value to what we decide to observe if needed.

The numerical protocol developed in this chapter can allow us to test the DEM independence of the method. One way would be by computing the synthetic radiance we add noise to with different DEMs. One example of this would be using a set of isothermal DEMs. This can allow us to see if the coefficients of the linear combinations

would be adapted to measure FIP biases of isothermal or almost isothermal plasma. It is possible that, because of the DEMs we use for the optimisation and because our cost function is built around an integral, at specfic temperatures our ratios would not work. Another way would be to compare the $P(f_p \mid f_i)$ distributions obtained when optimising with different sets of DEMs. The ones we use are very smooth and are adapted to plasma within a certain temperature range. We could compare results obtained from optimizing the coefficients from DEMs from simulations as well.

A way to improve further the method to compute the uncertainties would be by taking the uncertainties on the LCR coefficients into account. Then it would also be possible to improve LCR itself, by taking the instrumental model and expected line radiances into account during the optimisation of the coefficients. Comparing the inferred FIP biases to the inputs of the synthetic radiances, it would be possible to not only quantify the quality of the selection of the lines but also to determine the coefficients of the linear combinations, in the same fashion as in Guennou et al. [2012a] where they seek the parameters of the DEM models that would fit best their input. We here suppose that the coefficients have been sufficiently well optimized. We assume that they are good enough and that the combinations we have chosen are adequate for relative FIP bias measurements. We could follow more closely the methodology proposed in Guennou et al. [2012a] to test our linear combinations by adding in at the beginning the extra step of applying the previous process over the coefficients space and even further by iterating this process through a large sample of sets of spectral lines.

We will now apply the LCR method to observation carried out with the EIS spectrometer. We will analyze the plasma of an AR hours before a jet erupted in the hopes of linking its composition to in-situ measurements. We will be able to provide relative FIP bias measurements at different temperatures and provide uncertainties for these measurements using the techniques developed in this chapter.

5

A TEST CASE WITH A CORONAL JET FROM AR 11092

Context. *This work is part of the joint effort of ISSI team n.418 "Linking the Sun to the Heliosphere using Composition Data and Modelling" led by Susanna Parenti.*
Aims. *The goal of the team is to propose a methodology to connect phenomena taking place in the solar atmosphere to plasma in the heliosphere making use of both data and modelling through elemental composition. The proof of concept for the method tests it out in the case of a coronal AR jet.*
Methods. *We used remote sensing data to determine the relative elemental abundances of various areas of the AR in which the jet appeared. This chapter presents these measurements made using the LCR method.*
Results. *We present the process of selection for the sets of lines to be used, as well as the obtained measurements with their corresponding uncertainties.*

5.1 INTRODUCTION

When a plasma structure leaves the solar atmosphere, it will follow magnetic field lines. The biggest challenge to be sure that the plasma we measure with our instruments comes from that plasma structure that left the Sun is that a complete spatial mapping of data from the Sun to any point in the heliosphere does not exist. Plus, as the SW expands, the topology of the magnetic field changes, the plasma structure may interact with its environment, and there is an uncertainty concerning the changes the structure might undergo through during its travels. We will measure the plasma in situ with

a delay. This is why we need to develop a method that can unambiguously connect what is being measured in the heliosphere to the solar atmosphere.

As mentioned in Sec. 1.3, we could use composition diagnostics to map back heliospheric plasma to its source at the Sun. This is the main objective of the ISSI team n. 418 "Linking the Sun to the Heliosphere using Composition Data and Modelling" led by Susanna Parenti which I had the chance to contribute to. This new methodology takes full advantage of the available remote sensing and in-situ composition data and the latest advances in modelling from the coronal magnetic field to the solar wind. With the launches of Solar Orbiter and Parker Solar Probe, we are closer than ever to the Sun therefore closing on the gap between remote sensing and in-situ observations. The proof of concept for the method tests it out in the case of a coronal AR jet. The aim is to track this distinct coronal plasma from its solar origin to interplanetary space thus establishing a connection between the Sun and the heliosphere.

The team used remote sensing observations to obtain magnetograms as well as temperature, density, Doppler motion and elemental abundance diagnostics of the Sun at the time of the jet. These plasma diagnostics were performed to identify coronal outflow regions and variations within the AR that could be uniquely matched to the in-situ measurements. The magnetograms serve as seeds for different magnetic extrapolation techniques, which allow us to examine the local magnetic field surrounding the AR of interest as well as determining the global coronal magnetic structure of the Sun. Then we can detect the effects the jet had on the local topology of the AR and, in a more global scale, to map open field regions from which plasma can escape into the interplanetary medium and the structure of the helmet streamer belt. The global magnetic field and the solar wind were simulated using a global steady-state MHD modeling which describes the evolution and transport of density, momentum and energy along with the evolution of the magnetic field and electric current. Lastly, in-situ abundance measurements are connected to their upper solar atmosphere using heliospheric ballistic back-tracking which takes into account the Parker spiral that the solar wind forms as it fills the solar system.

UV spectroscopy will allow us to determine the elemental composition of the solar corona surrounding this jet. In this chapter, we will first briefly describe AR jets and present the jet we are interested in. We will then describe how we used the LCR method (see Ch. 3) to determine the relative abundances of different areas of this AR. The process of choosing the spectral lines to use will be described in its entirety, showing examples of sets that work as well as sets that do not work, performing the same tests described in Sec. 3.2. We then will determine the uncertainties of our measurements using conditional probabilities as described in the previous chapter. Finally, we will compare these results to those obtained by a different method.

5.2 AR 11092 & THE AUGUST 2nd 2010 SOLAR JET

5.2.1 *AR jets*

Following the launch of the Yohkoh spacecraft [Ogawara et al., 1991], the Soft X-ray Telescope (SXT: Tsuneta et al. [1991]) allowed for the discovery of numerous dynamic phenomena taking place in the corona, X-ray jets amongst them [e.g. Shibata et al. [1992] & Strong et al. [1992]]. X-ray jets are impulsive and collimated eruptions which appear as short-lived enhancements in X-ray observations of the corona. They are typically associated with bright point flares, ARs or regions where we observe magnetic flux emergence. They are hot streams of plasma with temperatures above 10^6 K and densities ranging from 10^8 to 10^{10} cm^{-3} and may sometimes be associated with cool plasma surges. Statistical analysis of these jets [Shimojo et al., 1996] show that most of them appear to emerge in more active areas. The jets that have their footpoints in ARs often occur at the western periphery of the sunspot. We can also observe them in UV light. During such eruptions, the underlying magnetic field reconfigurates. This suggests that magnetic reconnection may be one of the main drivers of these plasma eruptions.

5.2.2 *Previous analysis of this region*

The jet the team focused on occurred on August 2nd, 2010 in AR 11092 between 17:10 and 17:35 UT. In Fig. 5.2.1 we show AR 11092 a day before the jet appeared as observed by the EIS spectrometer on board Hinode. In Mulay et al. [2016] this jet is analysed in detail. It corresponds to Jet 1 in that paper. They describe the event in its entirety including its kinematics, how the magnetic field evolved, and investigate its possible relationship to other phenomena. These include a low-temperature component visible in Hα, a hot source visible in hard X-ray emission, and a type-III radio burst. They noticed flux emergence and cancellation prior the eruption. The authors identified the footpoints of the jet and they coincide with an open field region. This coronal outflow region will be denoted as CO1 and is indicated by a small rectangle in Fig. 5.2.1.

To fully understand if this jet material reached the interplanetary medium, the team performed plasma diagnostics of the AR from the 1st to the 3rd of August. A detailed analysis of the magnetic field configuration before and after the jet was performed determining that the jet took place in an area where upflows were visible in Doppler imaging and surrounded by a small open magnetic field area thus making it possible that the jet material could leave the corona. The whole method summarized in the introduction of the chapter culminates in the search for signatures of this plasma

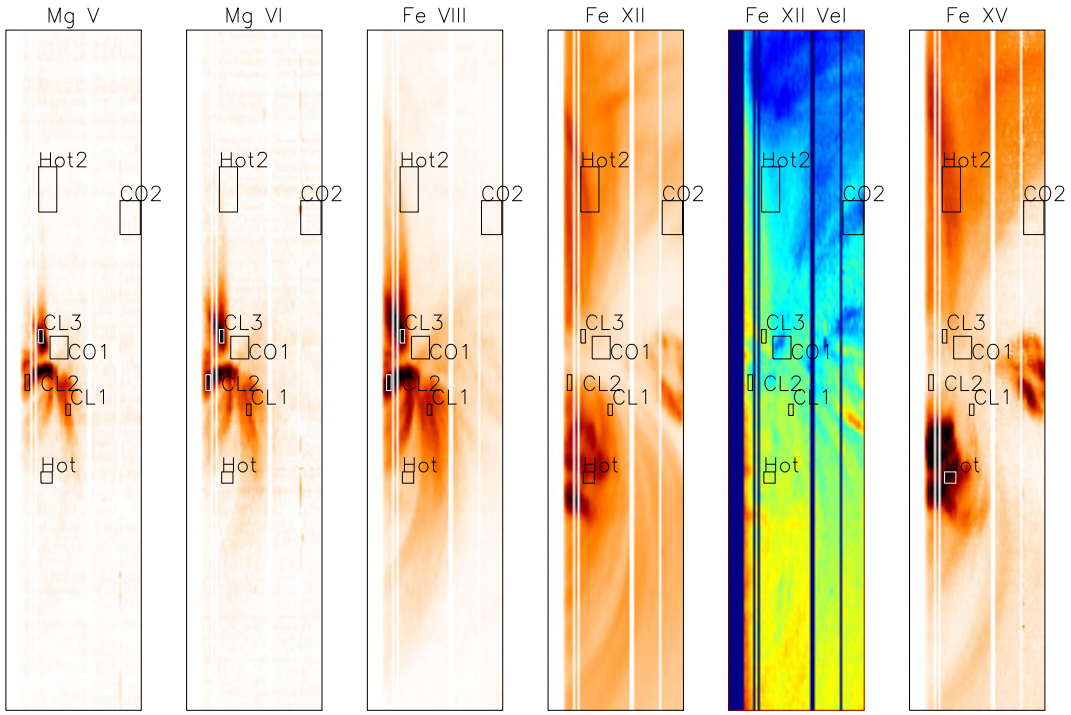

Figure 5.2.1: Integrated intensities (negative images) maps at different temperatures from the EIS raster at 23:39 UT August 1st. The velocity map obtained from the Doppler shift observed in the Fe XII 195.12 Å line is also shown (with a color scale of ±30 km/s). The various regions selected for further analysis are indicated. Courtesy of the ISSI team [Parenti et al., in prep.].

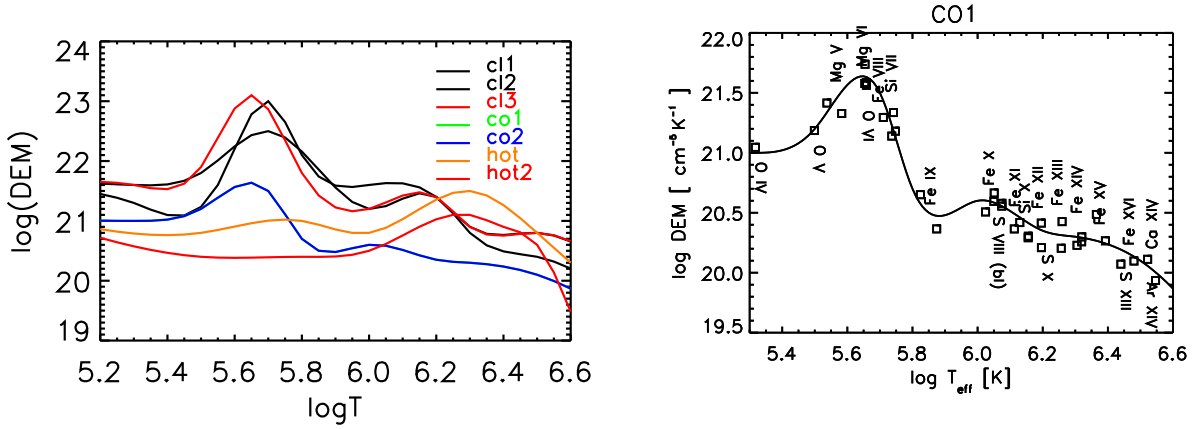

Figure 5.2.2: Left: DEMs of all the regions of interest. Right: DEM of the coronal outflow region CO1. The points indicate the ratio of the predicted vs. observed radiance, multiplied by the DEM value at the effective temperature. Courtesy of the ISSI team [Parenti et al., in prep.].

within the in situ measurements. The detection of in-situ signatures of an AR jet has been attempted in the past, but with unclear results (see for instance Corti et al. [2007]; Raouafi et al. [2016]).

In this chapter we will focus solely on diagnostics of the pre-eruption AR. We will do so by analyzing a raster scan taken by EIS the day prior to the jet. For consistency, and so that relative FIP bias measurements obtained using two different techniques can be compared, we used the same radiances obtained by Giulio Del Zanna for the DEM analysis of the AR.

This raster consists in a full-spectrum of the AR which we will use for FIP bias diagnostics at different temperatures (and therefore different heights in the AR). The observation was carried out only 6 hours before the jet's appearance with the 1" slit and with a 60 second exposure. The intensities in a selection of spectral lines, as well as the Doppler image in Fe XII are shown in Fig. 5.2.1. The EIS data were processed using custom-written software by Giulio Del Zanna. The Doppler image was obtained by removing the orbital variations and the expected variations along the slit, as described in the EIS software note No. 23[1].

The spectral lines profile and total intensity were measured assuming a Gaussian profile and using the Del Zanna [2013] radiometric calibration. The plasma diagnostics was done using the CHIANTI v.8 atomic physics database and software (Dere et al. [1997], 2019). Synthetic lines intensity were calculated assuming ionization equilibrium and photospheric composition Asplund et al. [2009]. Even with an exposure time of 60s, some coronal lines were rather faint. Seven different regions of interest were selected and the spectra were averaged over these rectangular areas. The region denoted as CO1 is where the jet originated. We can see in Doppler shift map that this area corresponds to an outflow area. Another coronal outflow region is denoted as CO2, it has similar characteristics to CO1. As we can see from the Fe XV intensity map on the far right of Fig. 5.2.1, HOT and HOT2 correspond to two regions with hot plasma loops (over 3 MK), we see very little emission from colder spectral lines in these areas. Finally, three regions on the cool loops extending towards the west were selected (CL1, CL2, CL3).

The thermal distribution of the plasma was derived using the Del Zanna [1999] method. Fig. 5.2.2 shows the DEM distribution of the CO1 area. The points indicate the ratio of the predicted vs. observed radiance, multiplied by the DEM value at the effective temperature. We can see that the emission in the coronal outflow region is strongly multi-thermal. The peak of the DEM, at lower temperatures, corresponds to a structure of cool fan loops, visible in the 3rd panel of Fig. 5.2.1 and that were also visible in images taken by AIA at the 171 Å band (not shown in this thesis).

[1] All EIS software notes are available at the EISAnalysisGuide

Relative FIP biases were measured for all the different regions. These results and how they compared to ours will be discussed in Sec. 5.5. We will now present our process of selection of the lines, which sets worked and which did not.

5.3 SELECTING OUR SETS OF SPECTRAL LINES

We tried to take advantage of the fact that we had an EIS full spectrum, including many different spectroscopic lines, to measure relative FIP biases at different temperatures. The same lines were not always observable in all regions because of the different solar structures seen in these regions. In order to measure relative FIP biases with the same set of spectral lines across all areas of interest, we first had to determine which lines had been successfully fitted in all of them. We show the contribution functions of all these lines in Fig. 5.2.3. To keep our analysis consistent with that of the team, we also used a constant density of $2 \times 10^9 \mathrm{cm}^{-3}$ to calculate the contribution functions of the lines, although we note that most of them are nearly independent of density.

We now have to select sets of lines to perform relative FIP bias measurements. Each set was selected mainly by following the shapes of the contribution functions and limiting each set to a given temperature range. Because there are fewer spectral lines from high FIP elements, each set contains one or two lines from high FIP elements and two or more lines from low FIP elements, making sure the latter encompass the same temperature range. For the time being, the selection of which lines from low FIP elements would be best to mix so that their combined shape resembles best the contribution functions of the lines from high FIP elements is done manually. Automating this process would be a great addition to the `fiplcr` Python module. This will be further discussed in Sec. 5.5.

A number of sets were tested. The first hurdle they had to pass was that the optimization algorithm would be able to find coefficients for the linear combinations that satisfy $\psi_{\mathrm{EM}} = \langle \mathscr{C}_{\mathrm{LF}}, \mathrm{EM} \rangle / \langle \mathscr{C}_{\mathrm{HF}}, \mathrm{EM} \rangle \approx 1$ for the set of EMs we use to do the optimization, i.e. that the resulting cost function Φ defined in Eq. (3.11) was close to zero. We found five satisfactory sets at various temperature ranges. They correspond to the five first sets of lines that are listed in Table 5.2.1. The lines emitted by the coolest plasma are on the top of the table and the temperature of the plasma emitting these lines increases in every set going down the list. We present the results of the optimization in Table 5.3.1 which, similarly to Table 3.3, lists the resulting ψ_{EM} for all reference EMs as well as the computed cost function Φ. There is a sixth set listed in both these tables that has a cost function significantly higher than the other sets. We will discuss it in more detail in Sec. 5.3.6.

Table 5.2.1: Sets of spectral lines we tested. The goal is to use them to measure the AR's relative FIP bias at different temperature ranges. The table shows six different sets of spectral lines, including the ions emitting them, their wavelengths, the temperature of maximum emission T_{max} and the optimised coefficient for the LCR method. These coefficients were calculated for a density of $\log n = 9.3$. The spectral lines in bold correspond to ions with a high FIP.

Set #	Ion	Wavelength (Å)	$\log T_{max}$ (K)	LCR coeff
1	**O V**	**248.46**	5.4	1.00
	Si VI	246.002	5.7	2.76
	Mg V	276.579	5.5	0.362
	Mg VI	270.39	5.7	-4.51
2	**S VIII**	**198.553**	5.9	1.00
	Si VII	275.361	5.8	0.743
	Si VIII	276.85	5.9	0.219
	Fe X	184.537	6.0	0.369
	Fe XI	180.401	6.1	-0.0207
3	**S X**	**264.23**	6.2	1.00
	Si X	258.374	6.1	0.691
	Fe XIII	202.044	6.2	0.164
	Fe XIV	264.788	6.3	0.117
4	**S XI**	**285.822**	6.3	1.00
	Ar XI	**188.806**	6.3	-0.155
	Fe XIII	202.044	6.2	0.139
	Fe XIV	211.317	6.3	0.223
	Fe XIV	264.788	6.3	-0.384
5	**S XII**	**288.434**	6.3	1.00
	S XIII	**256.685**	6.4	0.414
	Fe XV	284.163	6.3	0.0988
	Fe XIV	211.317	6.3	0.165
	Fe XVI	262.976	6.4	1.74
6	**Ar XIV**	**194.401**	6.5	1.00
	Ca XIV	193.866	6.5	0.792
	Fe XV	284.163	6.3	-6.27×10^{-4}

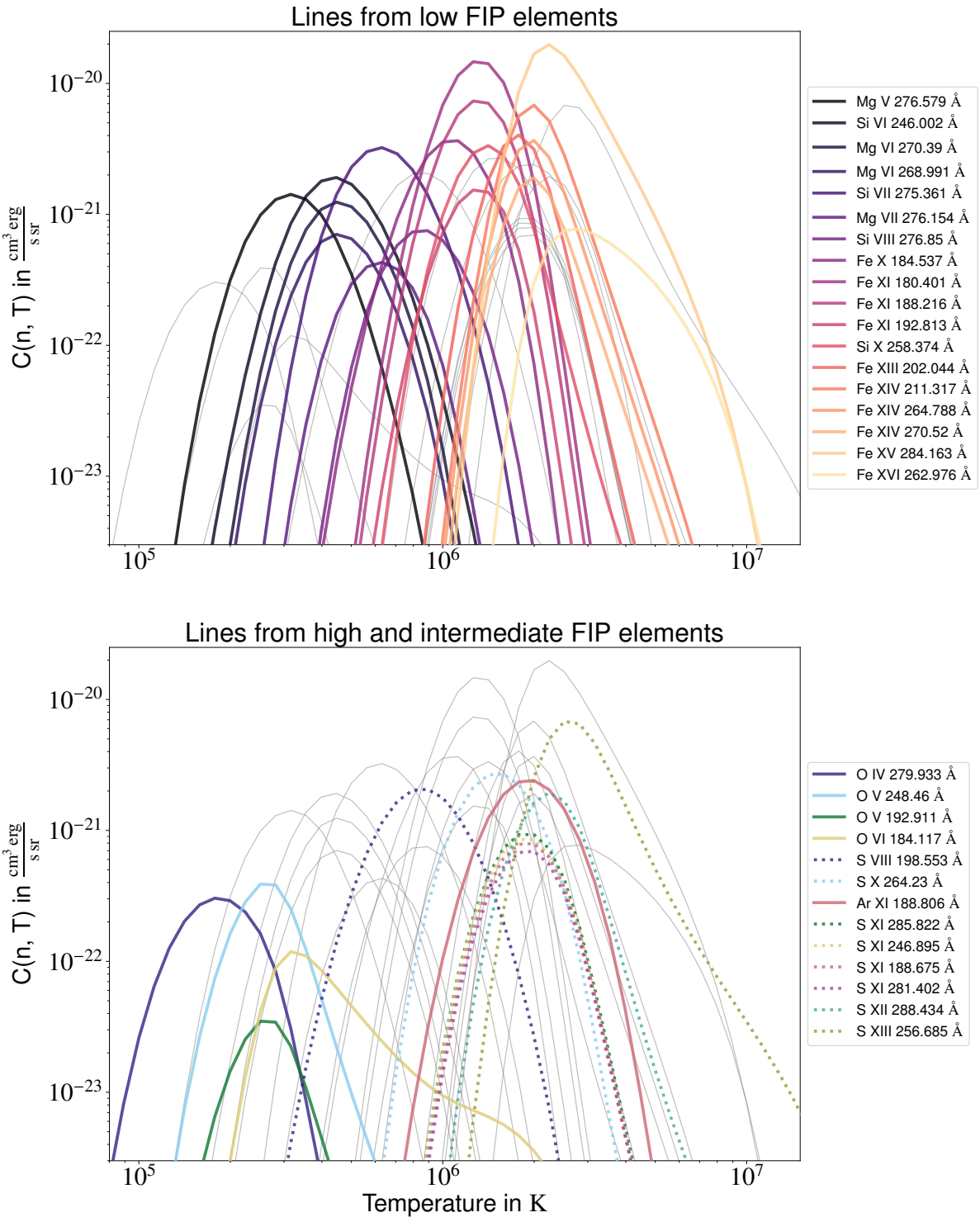

Figure 5.2.3: Contribution functions of all the lines that were successfully fitted in all areas of interest indicated in Fig. 5.2.1. The top panel shows the lines from low FIP elements in color and the fainter grey lines in the back are from intermediate and high FIP elements. In the lower panel the full lines in color correspond to lines from high FIP elements and the dotted colored lines correspond to lines from intermediate FIP elements. In the same fashion as at the top, the fainter grey lines in the back are from low FIP elements.

Table 5.3.1: Value of ψ_j (see Eq. 3.12) for each set of spectral lines listed in Table 5.2.1 for each reference EM, as well as the resulting cost function ϕ (see Eq. 3.11).

Set	ψ_{QS}	ψ_{AR}	ψ_{CH}	ϕ
1	1.000002	1.000005	1.000004	6.7×10^{-6}
2	0.999937	1.000075	1.000041	1.1×10^{-4}
3	1.000051	0.999998	1.000019	5.5×10^{-5}
4	1.000086	0.999629	1.000635	7.4×10^{-4}
5	1.000025	1.000029	1.000045	5.9×10^{-5}
6	0.877134	1.095324	1.002055	1.6×10^{-1}

Table 5.3.2: First ionization potential of the elements used for the tests, their coronal and photospheric abundances taken from Schmelz et al. [2012] and Asplund et al. [2009].

Element	FIP (eV)	A_X^C	A_X^P
Ca	6.11	4.37×10^{-6}	2.19×10^{-6}
Mg	7.65	7.41×10^{-5}	3.98×10^{-5}
Fe	7.90	7.08×10^{-5}	3.16×10^{-5}
Si	8.15	7.24×10^{-5}	3.24×10^{-5}
S	10.36	1.69×10^{-5}	1.32×10^{-5}
O	13.62	4.07×10^{-4}	4.90×10^{-4}
Ar	15.76	2.24×10^{-6}	2.51×10^{-6}

Once the sets were chosen, we tested them further. We applied three different procedures:

- Using the same techniques as in Sec. 3.2, we applied the LCR method on synthetic radiances (where we imposed uniform abundances) of the AR and CH EM cubes we computed in Sec. 3.2.3 from AIA observations. We then compare how the LCR method performs for each set of spectral lines in these two different solar regions. Table 5.3.2 lists all the ions we used, their FIP and the abundance values we imposed. The coronal abundances come from Schmelz et al. [2012] and the photospheric abundances are the same used by the team, taken from Asplund et al. [2009]. From these tests we will see if the FIP bias maps we obtain are rather uniform and, therefore, if the set is a good candidate or not for relative FIP bias diagnostics.

- We know from Table 5.3.1 that, even after the optimization, the residuals of the cost function are not zero. These residuals come from the fact the the products $\mathscr{C}_{\mathrm{LF}}(T)\,\mathrm{EM}(T)$ and $\mathscr{C}_{\mathrm{HF}}(T)\,\mathrm{EM}(T)$ for the different EMs used for the optimization are not close enough. Furthermore, even though the intergrals of these products might be very close, it is possible that at some temperature ranges they have very different shapes. If the plasma we are analyzing is close to isothermal and its temperature happens to fall right were both products diverge, the LCR method will fail. We trace these products for the three different EMs used for the optimization to see how they might differ. This will be particularly helpful to analyze what issues there may be when the FIP bias maps obtained are not uniform.

- Finally, we measured the accuracy of every set by calculating $P(f_p \mid f_i)$ as we did in Ch. 4. Here, once again, we use a simplified model for the noise and we use the same EM depicted in black in Fig. 4.3.2 to synthesize radiances for the uncertainty measurements. We add Gaussian random perturbations with a 20% standard deviation to synthetic radiances when drawing 40 000 I_{ij}^{obs} for every spectral line listed in Table 5.2.1. We also compute the uncertainties for the obtained f_i values using the method described in Sec. 4.3.3.

We analyze the results from these three procedures for each set in the following subsections.

5.3.1 *Set # 1*

We plot the relative FIP bias maps obtained for set # 1 following the tests described in Sec. 3.2 in Fig. 5.3.1. As we can see, in both the AR and the CH regions, the linear

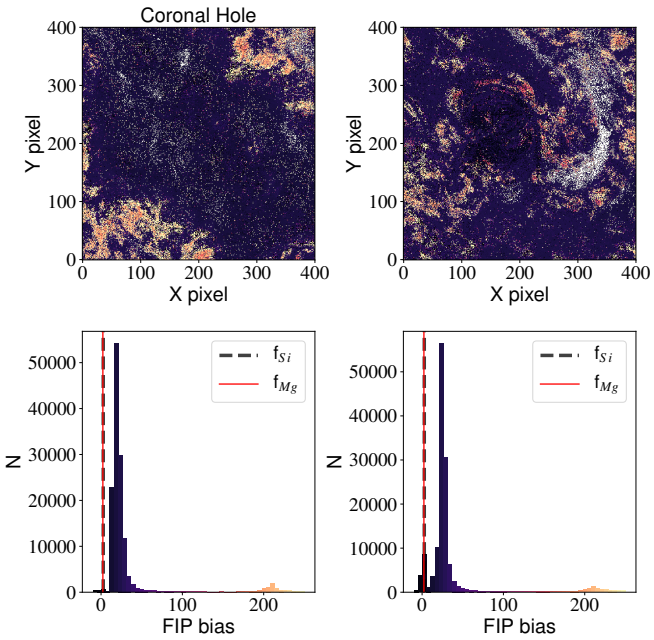

Figure 5.3.1: Results of FIP bias determination using LCR method methods on the synthetic radiances of a CH (left) and an AR (right) for set # 1. These are the same tests and the same regions described in Sec. 3.2. Relative FIP maps (top) and their corresponding histograms (bottom), with matching colour scales are shown. The DEM inversion code was not able to find a satisfactory solution in the pixels depicted in white. The vertical lines in the histograms correspond to the imposed uniform values of the relative FIP bias that should ideally be retrieved. These values are f_{Mg} / f_O = 2.24 in red and f_{Si} / f_O = 2.69 in dashed black lines.

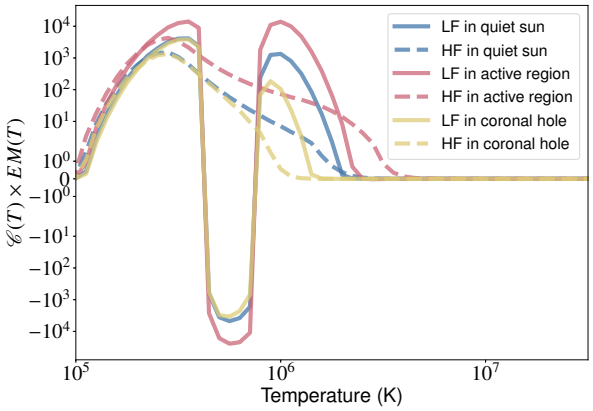

Figure 5.3.2: Linear combination of the products between the EM and the contribution functions of the spectral lines from set # 1 as functions of the temperature. The solid lines correspond to the calculations done for the lines from low FIP elements ($\mathscr{C}_{\mathrm{LF}}$) and the dashed correspond to those done for the lines from high FIP elements ($\mathscr{C}_{\mathrm{HF}}$) using the coefficients listed in Table 5.2.1. Different colours correspond to the different typical EMs from CHIANTI with which we optimised the coefficients.

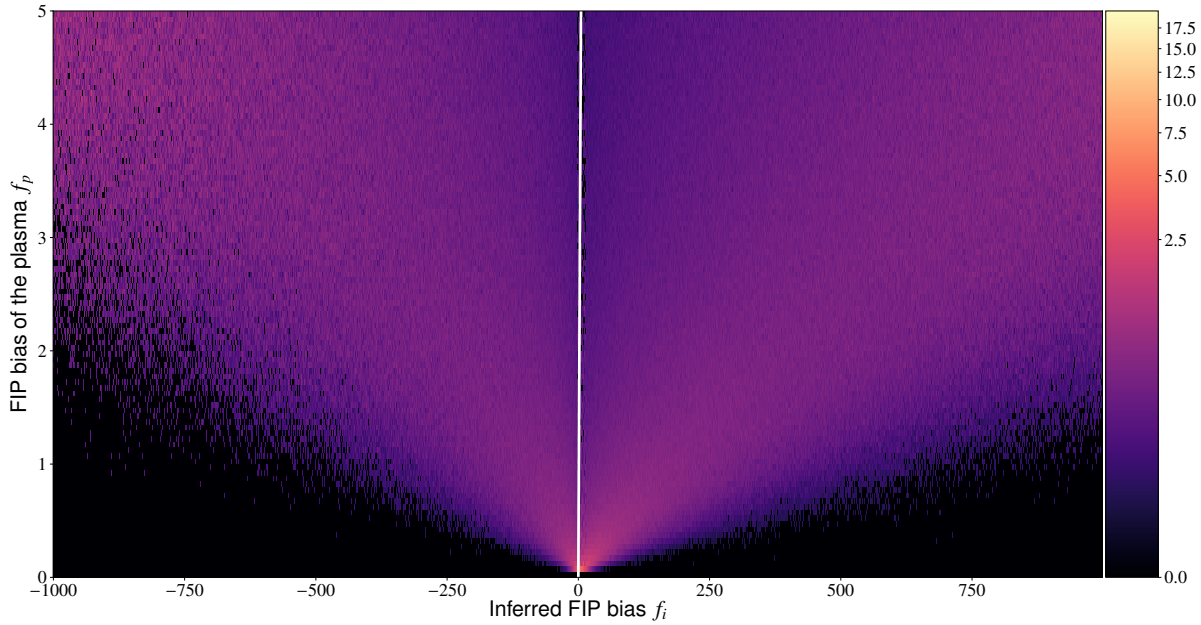

Figure 5.3.3: Conditional probability of the plasma having, on the ordinates, a given relative FIP bias (f_p) knowing the inferred relative FIP bias obtained from observations (f_i), on the abscissa, using the LCR method on set # 1. Probability distribution obtained for f_p varying from 0.0 to 5.0 with a prior probability distribution $P(f_p)$ that is uniform. The white line is the first bisector, where both values are equal.

combinations of lines we used perform very poorly. The histograms for these maps show that most values fall between 10 and 35 which is an enormous over-estimation considering we assumed $\frac{f_{Mg}}{f_O} = 2.24$ and $\frac{f_{Si}}{f_O} = 2.69$. We also have various areas where the relative FIP bias is estimated to be over 200. As we can see in Fig. 5.3.2, in order to compensate for the slope of the right wing of the O V 284.46 Å line which is less steep than its left wing's, the $\mathscr{C}_{LF}(T)\,EM(T)$ product drops considerably to negative values in the temperature range 450 000 to 750 000 K and then is raised again at around 1 MK. This is because the Mg VI 270.39 Å line has a negative coefficient in the LF linear combination (see Table 5.2.1, last column). The coefficients listed in Table 5.2.1 might result in a $\Phi \approx 0$ for the set (as we can see in Table 5.3.1), but from the relative FIP bias maps we obtained, we can conclude that we cannot measure relative abundances with this set. We get such high and even extreme values in the FIP bias maps because both regions have rather high temperature plasma (see Sec. 3.2, Figs. 3.2 and 3.3) and therefore $\mathscr{C}_{LF}(T)\,EM(T)$ is very high in these regions, there is not enough plasma at lower temperatures to compensate it. Because we optimize the coefficients basing the cost function on the ratio of the integrals of $\mathscr{C}_{LF}(T)\,EM(T)$ and $\mathscr{C}_{HF}(T)\,EM(T)$ for some specific reference EMs, cases like these are a blind spot to the optimization we do in order to obtain the coefficients for the LCR method. We see in Fig. 5.3.3, which depicts a zoom of $P(f_p \mid f_i)$ in the $f_i \in [-1000, 1000]$ interval for this particular set, that we

obtain a considerable amount of f_i values that span over various orders of magnitude. As we have seen in Fig. 4.3.2, we calculate these probabilities using an AR EM that peaks at high temperatures, giving further confirmation that without sufficient low temperature plasma, this diagnostic will not allow us to retrieve accurate relative FIP bias measurements.

5.3.2 *Set # 2*

We plot the relative FIP bias maps obtained for set # 2 following the tests described in Sec. 3.2 in Fig. 5.3.4(a). As we can see, in both the AR and the CH regions, the linear combinations of lines we used allow us to retrieve fairly uniform FIP bias maps. The histograms for these maps show that most values fall near the imposed relative FIP biases of $f_{Fe}/f_S = f_{Si}/f_S = 1.74$. We see in Fig. 5.3.4(b) that $\mathscr{C}_{LF}(T)\,EM(T)$ presents a dip into negative values as well but, in this case, with no apparent repercussions on the accuracy of the method. We still retrieve two relative FIP bias maps with histograms peaking at the imposed value and with a narrow distribution. From these tests, this set seems adequate for relative abundance diagnostics. Fig. 5.3.5 depicts a zoom of $P(f_p \mid f_i)$ in the $f_i \in [0, 15]$ interval where most of the obtained f_i values lie. The green contour, which is the credibility interval at 75 %, is what we use to define the uncertainties, as explained in Ch. 4. This set allows us to determine the relative FIP bias of an observed structure and we can provide the probability distribution of the plasma given the f_i inferred using the LCR method.

5.3.3 *Set # 3*

We know from the previous chapter that this set of lines is suitable for FIP bias measurements. We show once again the results of the tests and the probability distribution we had obtained in Sec. 4.3.2 in Figs. 5.3.6(a) and 5.3.7. They show a fairly uniform relative FIP bias map and the conditional probability distribution $P(f_p \mid f_i)$ which will allow us to compute the uncertainties associated with our measurements. Something that we are starting to see in Fig. 5.3.6(b) is that the typical EMs from CHIANTI that we used to perform the optimization only go so far in terms of temperature. We see this in the sudden drop to zero in the blue and red curves (QS and AR EMs respectively) as we approach 10 MK. These $\mathscr{C}_{LF}(T)\,EM(T)$ and $\mathscr{C}_{HF}(T)\,EM(T)$ products fall abruptly to zero above a given temperature even though the contribution functions of the spectral lines in these linear combinations are not equal to zero in this higher temperature range. This means that the light that is nonetheless being emitted by plasma at these higher temperatures is not being taken

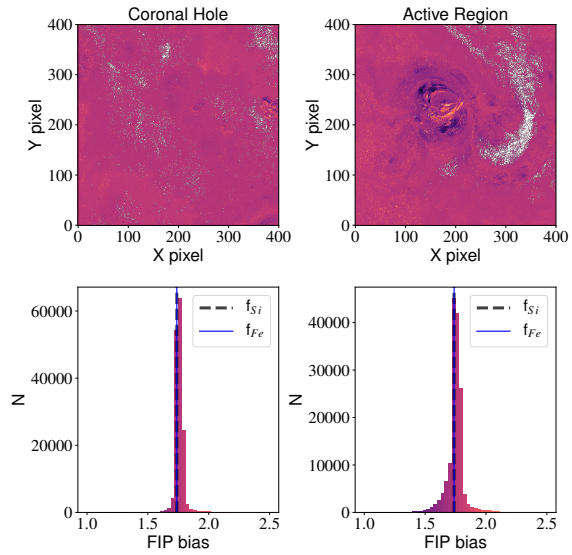

(a) Relative FIP bias maps and their corresponding histograms.

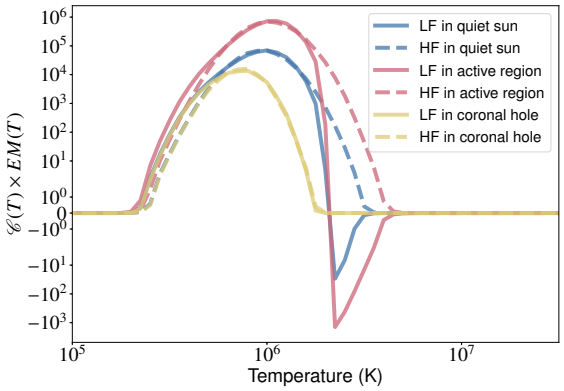

(b) $\mathscr{C}_{LF}(T)\,EM(T)$ and $\mathscr{C}_{HF}(T)\,EM(T)$ products as functions of temperature.

Figure 5.3.4: (a): Same as Fig. 5.3.1 but for set # 2. The vertical lines correspond to the imposed uniform values f_{Fe} / f_S = 1.74 in blue and f_{Si} / f_S = 1.74 in black dashed. (b): Same as Fig. 5.3.2 but for set # 2.

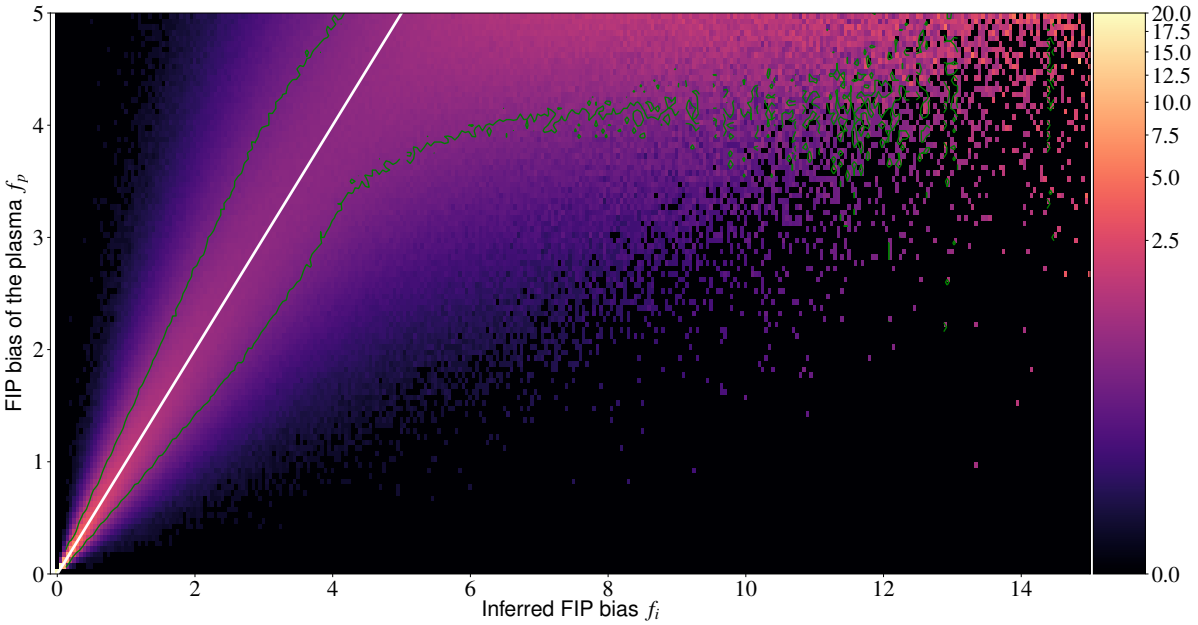

Figure 5.3.5: Conditional probability of the plasma having, on the ordinates, a given relative FIP bias (f_p) knowing the inferred relative FIP bias obtained from observations (f_i), on the abscissa, using the LCR method on set # 2. Probability distribution obtained for f_p varying from 0.0 to 5.0 and a prior probability distribution $P(f_p)$ uniform between 0.0 and 5.0. The white line is the first bisector, where both values are equal. The green contour corresponds to the 75% credible interval computed for each value of f_i.

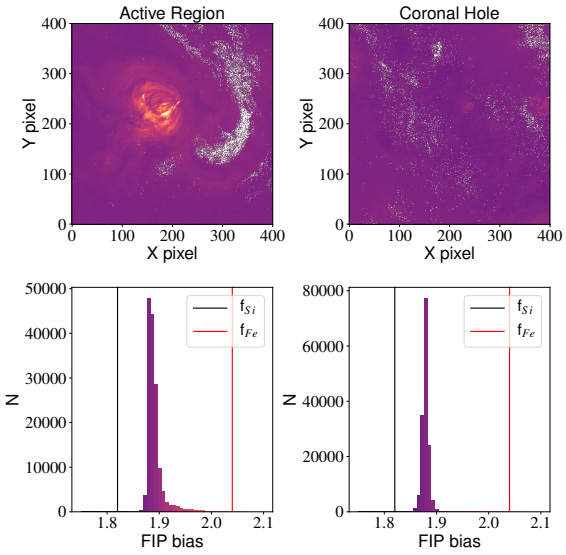

(a) Relative FIP bias maps and their corresponding histograms.

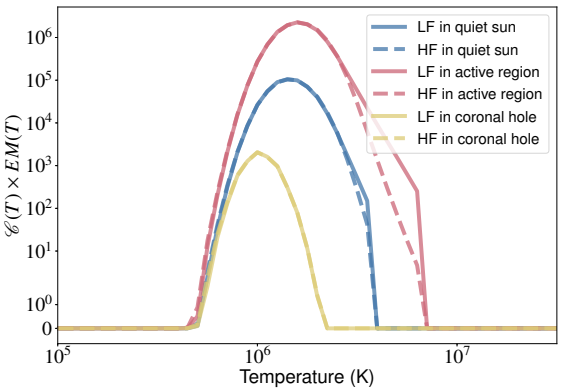

(b) Same as Fig. 5.3.2 but for set # 3.

Figure 5.3.6: (a): Same as Fig. 5.3.1 but for set # 3. The vertical lines correspond to the imposed uniform values $\frac{f_{Fe}}{f_S} = 2.05$ in red and $\frac{f_{Si}}{f_S} = 1.82$ in black.
(b): Same as Fig. 5.3.2 but for set # 3.

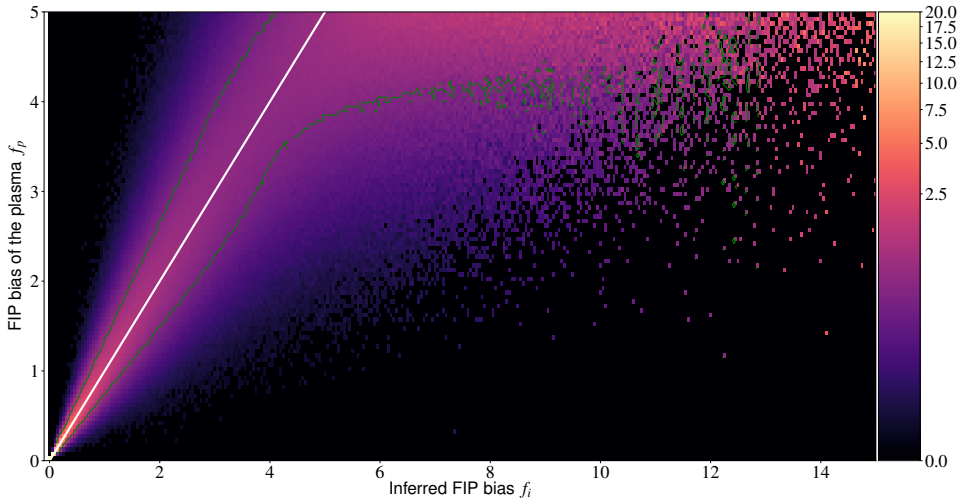

Figure 5.3.7: Same as Fig. 5.3.5 but for the set of lines # 3.

into account in the optimization process. As all the other sets we will test have lines that form at even higher temperatures, we will see this same phenomenon in all of them.

5.3.4 *Set # 4*

In Fig. 5.3.8(a), we see that we obtain FIP bias maps that underestimate the relative FIP bias, we do not retrieve values that are in between the values that we had imposed. In this case we might be using two ions that react too differently to the FIP effect and this is not advisable as the LCR method derives a single FIP bias value. Argon is a high FIP element and here sulfur is being used as a high FIP element even though it is an intermediate FIP element and, as we can see in the histograms, their relative FIP biases compared to iron will be very different. Furthermore, the coefficient of the argon line is negative in this case. We can see that the $\mathscr{C}_{\mathrm{HF}}(T)\,\mathrm{EM}(T)$ products depicted in Fig. 5.3.8(b) have two dips into negative values. This explains the very broad distribution of f_i values obtained in Fig. 5.3.9 (zoom of $P(f_p \mid f_i)$ for $f_i \in [-150, 150]$), which is similar to what we obtained for set # 1. This means that the single FIP bias value the method provides can be even lower than the sulfur FIP bias.

We advise against mixing elements that react so differently to the FIP effect. The values we would obtain using this method would be difficult to interpret. These results show further that the cost function used for the optimization algorithm has some blind spots due to the shapes of the contribution functions of the lines we use combined with the fact that it is based on the ratio of two integrals. This means that we obtain a set that has a very low cost function which would deem it accurate for relative FIP bias measurements even though it is not.

5.3.5 *Set # 5*

The results we obtain for set # 5 are very similar to those obtained for sets # 2 and # 3: the relative FIP bias maps depicted in Fig. 5.3.10(a) peak near the imposed relative FIP bias. In this case, the distribution is broader when dealing with higher temperatures. We have once again the $\mathscr{C}_{\mathrm{LF}}(T)\,\mathrm{EM}(T)$ and $\mathscr{C}_{\mathrm{HF}}(T)\,\mathrm{EM}(T)$ products shown in Fig. 5.3.10(b) falling abruptly to zero at high temperatures. Fig. 5.3.11 shows $P(f_p \mid f_i)$ which we will use to determine the uncertainties associated with our measurements. Unlike sets # 2 and # 3, set # 5 results in a $P(f_p \mid f_i)$ that is less symmetrical with respect to the first bisector: the real FIP bias of the plasma f_p will be underestimated systematically as shown by the green contour's bottom being flush with the first bisector. The f_i value obtained with the LCR method will more often than

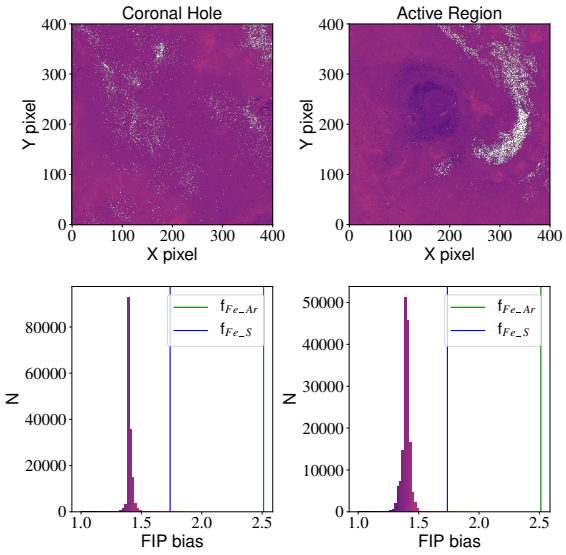

(a) Relative FIP bias maps and their corresponding histograms.

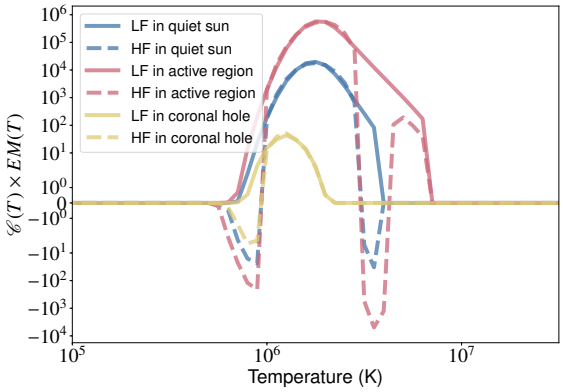

(b) $\mathscr{C}_{\mathrm{LF}}(\mathrm{T})\,\mathrm{EM}(\mathrm{T})$ and $\mathscr{C}_{\mathrm{HF}}(\mathrm{T})\,\mathrm{EM}(\mathrm{T})$ products as functions of temperature.

Figure 5.3.8: (a): Same as Fig. 5.3.1 but for set # 4. The vertical lines correspond to the imposed uniform values $\frac{\mathrm{f_{Fe}}}{\mathrm{f_{Ar}}} = 2.51$ in green and $\frac{\mathrm{f_{Fe}}}{\mathrm{f_S}} = 1.74$ in blue.
(b): Same as Fig. 5.3.2 but for set # 4.

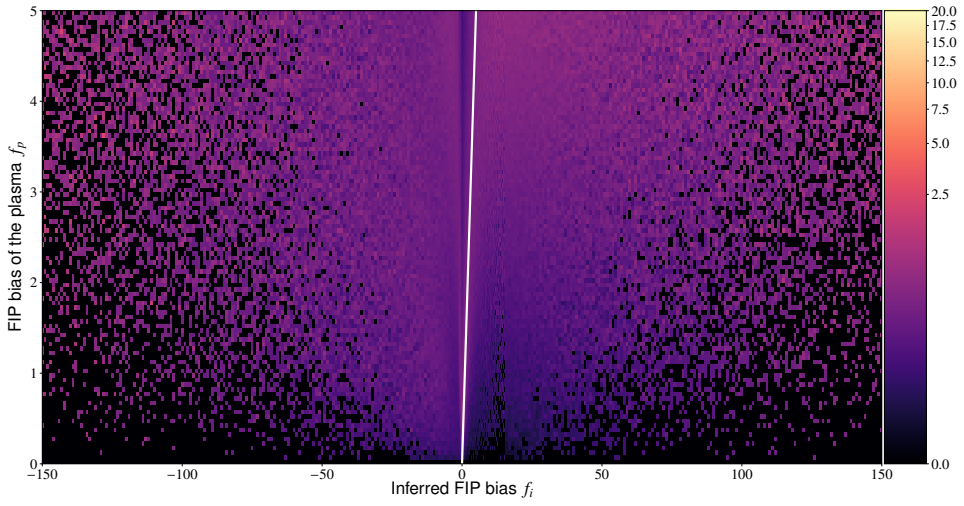

Figure 5.3.9: Same as Fig. 5.3.3 but for the set of lines # 4.

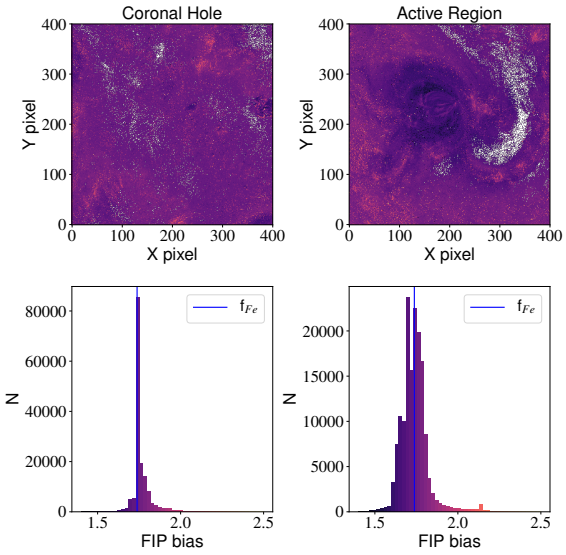

(a) Relative FIP bias maps and their corresponding histograms.

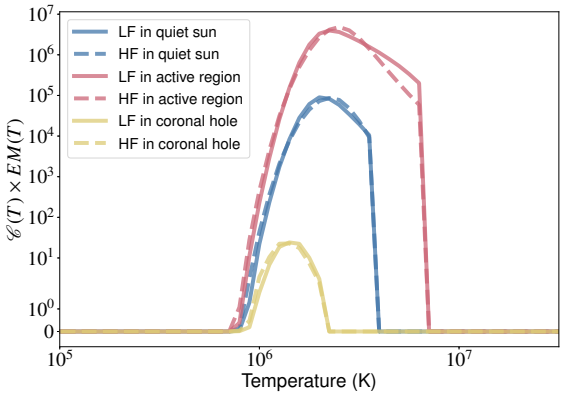

(b) $\mathscr{C}_{\mathrm{LF}}(\mathrm{T})\,\mathrm{EM}(\mathrm{T})$ and $\mathscr{C}_{\mathrm{HF}}(\mathrm{T})\,\mathrm{EM}(\mathrm{T})$ products as functions of temperature.

Figure 5.3.10: (a): Same as Fig. 5.3.1 but for set # 5. The vertical blue line corresponds to the imposed uniform value $\frac{f_{Fe}}{f_S} = 1.74$.
(b): Same as Fig. 5.3.2 but for set # 5.

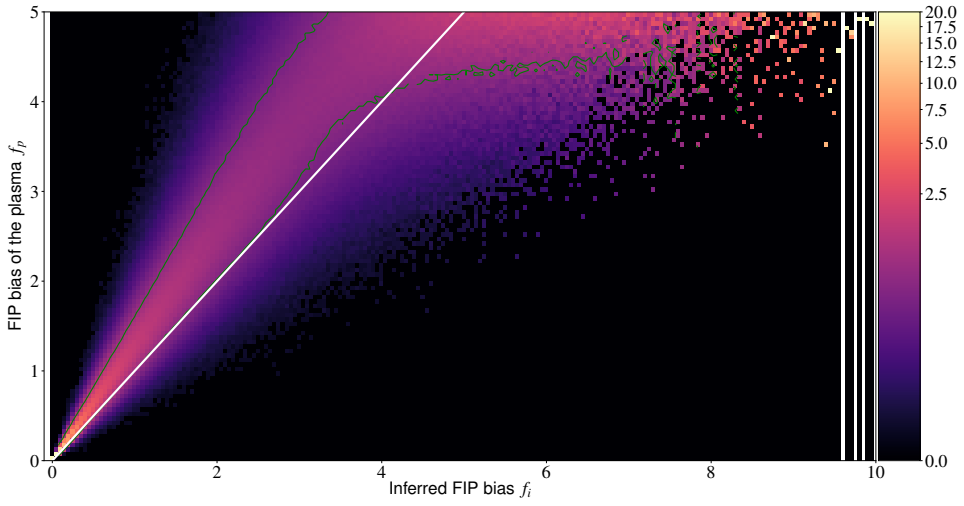

Figure 5.3.11: Same as Fig. 5.3.5 but for set # 5.

not be lower than f_p. Fortunately we do have access to the probability distribution of $P(f_p \mid f_i)$ which can allow us to correct that bias.

5.3.6 *Set # 6*

Set # 6 is the only set that is not observable in all the regions selected. It is only observable with high enough counts in regions CO1 and CO2. Given that CO1 is where the jet appeared, we were interested in measuring the FIP bias here in particular which led to try to have as many sets as we could in these regions. Even though set # 6 has the highest Φ (see Table 5.3.1), the relative FIP bias maps we obtain in Fig. 5.3.12(a) are much more uniform that those obtained with set # 1. Here we also fall victims to the limited temperature range of the EMs used for the optimization as we can see in Fig. 5.3.12(b). Fig. 5.3.13 shows $P(f_p \mid f_i)$ for this set and we obtain a similar distribution as the ones for sets # 2, # 4 and # 5 which we had deemed acceptable to be used to determine relative FIP biases. Given the probability distribution we obtain, we think that this set of lines could still be useful to measure relative abundances at very high temperature. It would benefit from an optimization carried out with EMs that include higher temperatures.

5.4 RELATIVE FIP BIAS MEASUREMENTS OBTAINED

Table 5.4.1: Relative FIP bias values obtained for each set of spectral lines deemed reliable for each region selected in AR 11092 from an observation carried out a few hours before the jet's on-set. We list the values of f_i measured using the observed radiances and the credibility interval at 75%. For example, for set # 2 and region CL1, we obtained $f_i = 2.2$ and the credibility interval at 75% is [1.5, 3.0].

Set	CL1	CL2	CL3	CO1	CO2	HOT	HOT2
2	$2.2^{+0.8}_{-0.7}$	$2.7^{+0.9}_{-0.8}$	$2.7^{+0.9}_{-0.8}$	$2.0^{+0.7}_{-0.6}$	$1.8^{+0.6}_{-0.6}$	$1.0^{+0.4}_{-0.3}$	$0.9^{+0.3}_{-0.3}$
3	$1.9^{+0.6}_{-0.5}$	$1.6^{+0.5}_{-0.4}$	$2.0^{+0.6}_{-0.5}$	$2.0^{+0.6}_{-0.5}$	$2.0^{+0.6}_{-0.5}$	$1.7^{+0.5}_{-0.5}$	$1.9^{+0.6}_{-0.5}$
5	$1.3^{+0.7}_{-0.1}$	$4.8_{-0.6}$	$2.9^{+1.6}_{-0.1}$	$2.5^{+1.5}_{-0.0}$	$1.8^{+1.0}_{-0.0}$	$1.8^{+1.0}_{-0.0}$	$1.4^{+0.9}_{-0.0}$
6				$3.1^{+1.6}_{-0.3}$	$3.3^{+1.5}_{-0.2}$		

The observed radiances of all the lines listed in Table 5.2.1 are shown in Fig. 5.4.1. We use these radiances to perform our relative FIP bias analysis using the LCR method. As previously stated, we assume a density of 2×10^9 cm^{-3} and photospheric abundances

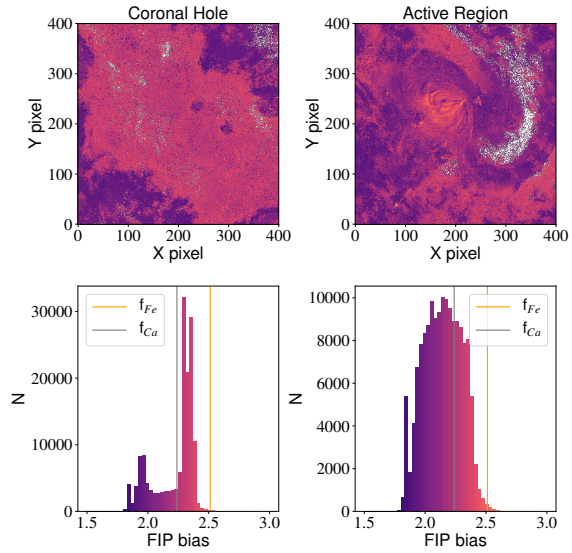

(a) Relative FIP bias maps and their corresponding histograms.

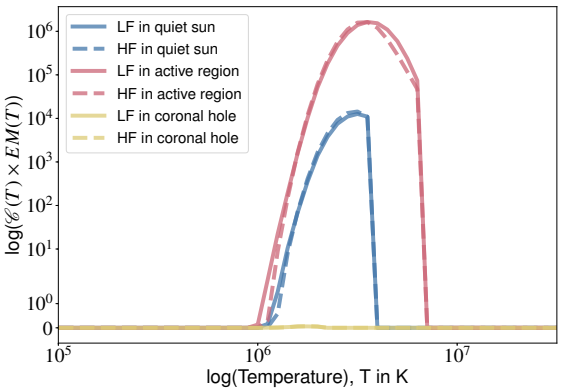

(b) $\mathscr{C}_{\mathrm{LF}}(\mathrm{T})\,\mathrm{EM}(\mathrm{T})$ and $\mathscr{C}_{\mathrm{HF}}(\mathrm{T})\,\mathrm{EM}(\mathrm{T})$ products as functions of temperature.

Figure 5.3.12: (a): Same as Fig. 5.3.1 but for set # 6. The vertical lines correspond to the imposed uniform values $\frac{\mathrm{f_{Fe}}}{\mathrm{f_{Ar}}} = 2.51$ in orange, $\frac{\mathrm{f_{Fe}}}{\mathrm{f_S}} = 1.74$ in blue, $\frac{\mathrm{f_{Ca}}}{\mathrm{f_S}} = 1.55$ in purple, and $\frac{\mathrm{f_{Ca}}}{\mathrm{f_{Ar}}} = 2.24$ in grey.
(b): Same as Fig. 5.3.2 but for set # 6.

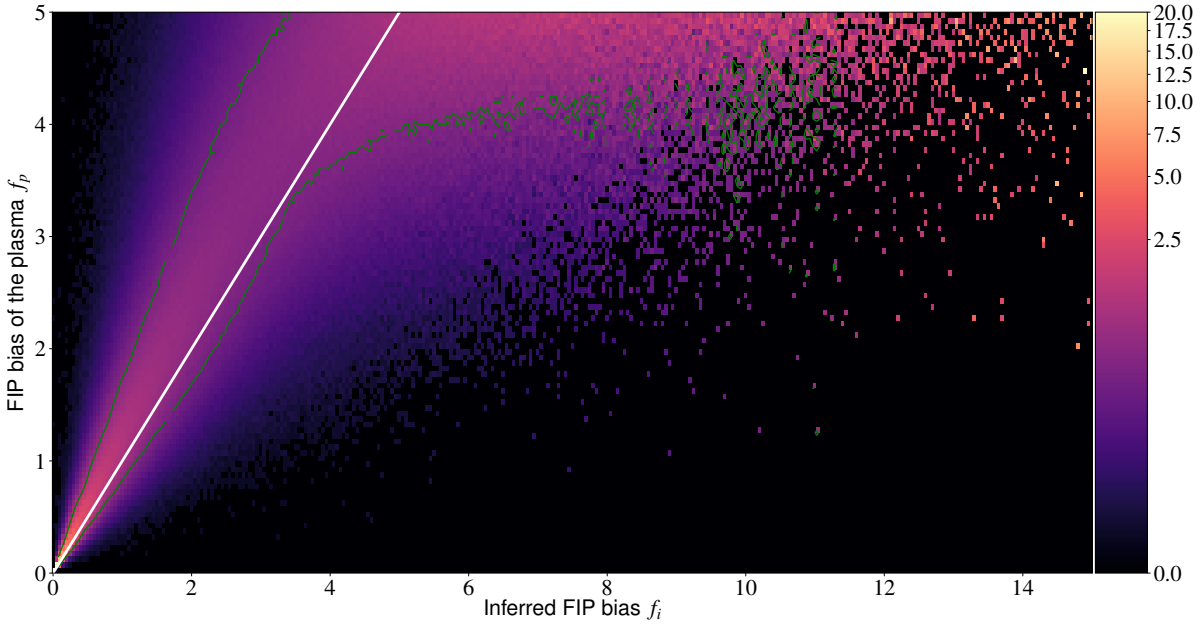

Figure 5.3.13: Same as Fig. 5.3.5 but for set # 6.

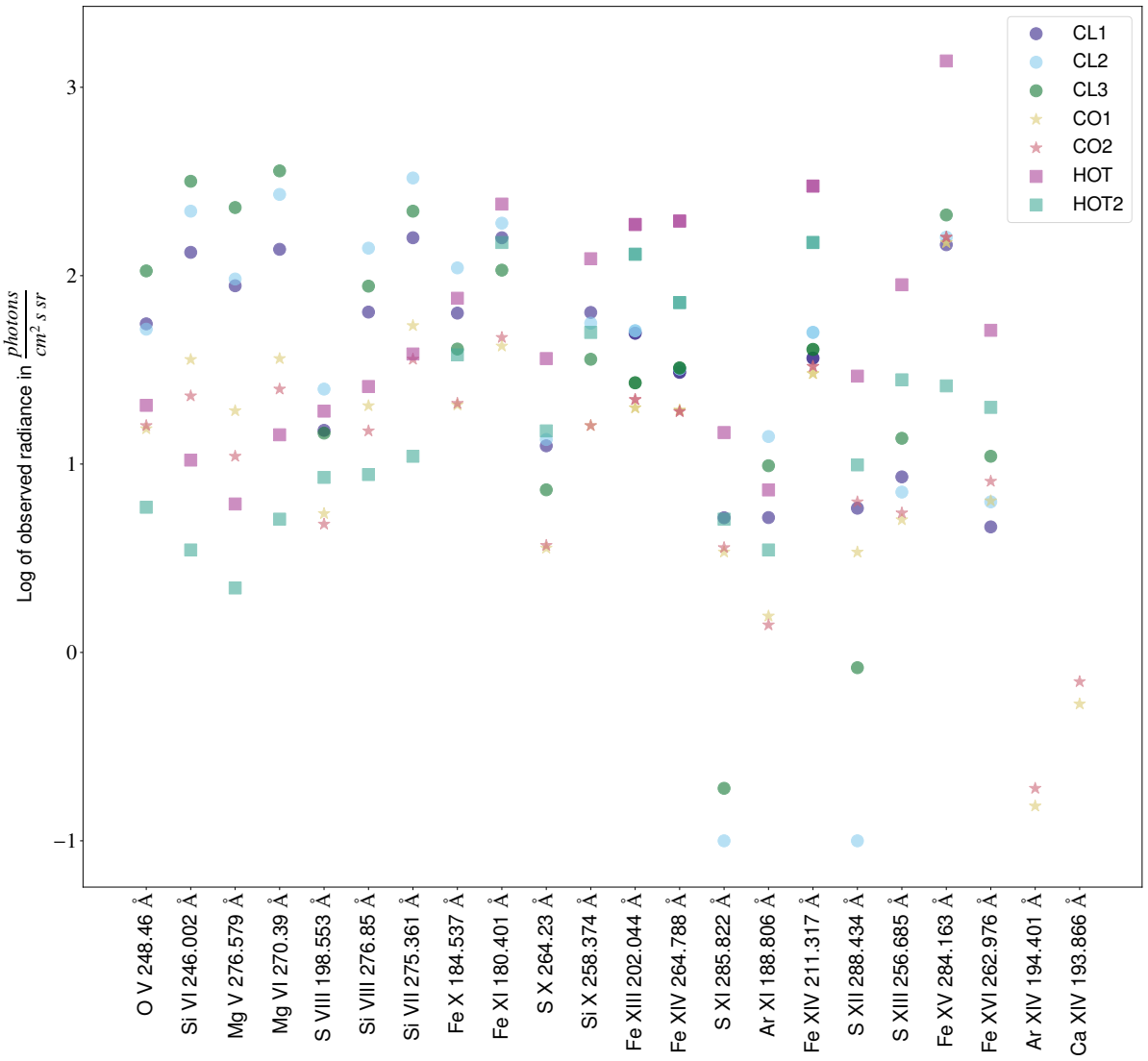

Figure 5.4.1: Logarithm of the observed radiances in photons cm^{-2} s^{-1} sr^{-1} for each spectral line listed in Table 5.2.1. The different markers and colors show the values in the different regions.

of Asplund et al. [2009]. The relative FIP biases obtained in each region using sets # 2, # 3, # 5 and # 6 in every region where the spectral lines for each set were observable are listed in Table 5.4.1. This table shows the values we obtained, i.e. the f_i inferred, as well as the credibility interval at 75%. For example, for set # 2 and region CL1, 75% of the possible f_p (knowing that we measured a f_i=2.2) lie in the interval [1.5,3.0]. We infer this from Fig. 5.3.5.

The FIP effect can only be constrained by the Fe/S relative abundance in sets # 2, # 3 and # 5. Sulfur is an intermediate FIP element which can be subject to a slight enhancement of its abundance. It is therefore no surprise that we obtain a higher value when comparing iron and calcium to argon in set # 6, argon having a much higher FIP than sulfur. In the CO1 and CO2 regions we observe an enhancement of low FIP elements as compared to the sulfur abundance of a factor 2 and at least a factor 3 when compared to argon. We should however note that the argon and calcium lines are very weak. As we have used Gaussian noise with a standard deviation at 20% to simulate noise in all lines, the uncertainties for the relative FIP bias obtained are most likely underestimated as these very weak lines (at least an order of magnitude lower than the iron line we also have in this set) would drag along more noise.

The hotter loop region HOT and HOT2 show photospheric abundances at lower temperatures (results of set # 2). Given that the very hot loops we wanted to analyse within this region barely exist at those temperatures and that coronal plasma is optically thin, what we are seeing in this temperature range is probably the underlying quiet sun material which does generally have abundances closer to photospheric. Higher in temperature we see an enhancement in the abundance closer to a factor 2. It should be noted however that the DEMs of regions HOT and HOT2 peak at log(T) = 6.3, the CH EM and the QS EM we used for the optimization drop to zero not far from that temperature and thus do not cover the higher temperature range of the EM used for testing. It is possible that, because the EMs we used for the optimization are not well adapted for these temperature ranges, the coefficients we obtained are not the most adapted or our error bars are underestimated. The lines used emit light at temperatures higher than those we can account for with our optimization.

In the cooler loop regions CL1, CL2, and CL3 we also see an enhancement. It should be noted however that within set # 5, the observed radiance for the S XII line in regions CL2 and CL3 drops significantly as compared to the radiance of the same line in other regions of interest as well as compared to most other lines. The relative FIP bias values obtained, specially when using lines that form at high temperatures, are therefore most likely to be inaccurate and their uncertainties underestimated. A value of 4.8 for the relative FIP bias is simply incorrect and a better model for the noise should have been considered.

5.5 DISCUSSION

From a EIS raster observation of an AR we have obtained relative FIP bias measurements at different temperatures. The measurements previously made by other members of the ISSI team showed similar results regarding the CO1 and CO2 regions. Concerning the hot loop regions, they found they had abundances closer to coronal, i.e. enhanced by a factor 2 to 3 as compared to photospheric abundances. Their measurements are a bit higher than ours but within the error bars. As explained above, the cost function that we use and the temperature range of the EMs we optimise the coefficients with might be playing a role. Unlike our measurements, they found that all the cool loop legs (CL1, CL2, CL3) indicated photospheric abundances, within a factor of two. Our measurements are a bit higher than that.

For sets # 1, 2 and 4 the minimization results in negative coefficients which can lead to obtaining non physical negative values for the FIP bias, especially for noisy observations. This should not be an issue when dealing with a small negative contribution to the overall pseudo contribution function as it was the case in Chapter 3. When negative coefficients change dramatically the shapes of the $\mathscr{C}_{\mathrm{LF}}(T)\,\mathrm{EM}(T)$ and $\mathscr{C}_{\mathrm{HF}}(T)\,\mathrm{EM}(T)$ products, forcing the coefficients to be positive might be a better option. I tested a different minimization algorithm that allows to put constrains on the coefficients (L-BFGS-B). I did so on sets # 1 and # 4. This did not work as the algorithm gave null coefficients to most lines, leaving us in each case with only one LF line and one HF line that have contribution functions that differ too much. This simply suggests that just because these lines form at similar temperature ranges, they will not automatically be suited for relative FIP bias measurements. We will just have to look for other lines to combine.

Following the results observed for the hotter sets of lines, perhaps it would be more judicious to use a set of EMs that span over a broader temperature range to optimise the LCR coefficients. This would allow us to optimise the coefficients by taking into account the emission of these lines which we cut off with the EMs that we currently use. Another option would be to perform the optimization using a set of different EMs that are representative of the type of object one is planning to observe. There might still be blind spots following the latter approach and one might misdiagnose a fraction of the observed plasma that does not fit the cannon imposed by the EMs used for the optimization. Furthermore, this goes against the philosophy of the method which aims to be DEM independent. This matter truly needs more digging into. The EMs we have used for the tests are better adapted to measurements in a hot corona but not in a scalding hot one.

The AR EM we used to perform Bayesian analysis is not be the best suited to determine uncertainties at lower temperatures, this is important for sets # 1 and # 2 in particular. In the future, we will use an EM better adapted to these temperatures.

Concerning the uncertainties obtained for the spectral lines that are weak, I think they are an underestimation. A lot of the lines we used were very weak, sometimes with an observed radiance over 3 orders of magnitude smaller than another line used in the same set. Assuming an error of only 20% for all of them equally is painting with too broad a brush. This value was chosen to test them all because we do not have the uncertainty value for every single EIS radiance measured by the ISSI team. A more accurate simulation of the noise will be carried out in the next chapter. If one is to use this method to estimate uncertainties, the errors on the fitting of the lines and any source of noise and uncertainty *must* be taken into account. This thesis in general focuses more heavily on the methodological aspect of measuring FIP biases with the LCR method and the real life application of the method has been less developed for the moment. This chapter in particular would greatly benefit of a better synergy between the two.

Moreover, one of the main issues that testing all these different sets of lines has surfaced is that the value of the cost function does not always reflect the aptitude of a set of lines to perform accurate relative FIP bias diagnostics. For 2 out of the 5 first sets, we had obtained a cost function very close to zero, the relative FIP bias maps and the conditional probability densities showed however a different story. When analyzing Figs. 5.3.2 and 5.3.8(b) we can see that the over-compensations (the temperature ranges where values drop) occur often in the wings of the $\mathscr{C}(T)\,\mathrm{EM}(T)$ products. When we had first developed the LCR method, the cost function was based solely on the contribution functions of the lines. The wings of the contribution functions were problematic as they had the biggest differences. Using a quadratic loss function that is by nature dominated by outliers made it so that these wings completely dominated how the coefficients were being optimised. This was not useful at all since most of the radiance emitted by the line does not come from the wings of the contribution function. We had hoped that by switching from only comparing the contribution functions to comparing the integrals of the products of the contribution functions and typical EMs we would obtain better results. We did, the previous two chapters are a testament to that, but our cost function still cannot discriminate between sets of lines as well as we would like. We need to test out other cost functions or find another way to flag the sets that will not be useful if we want to test out systematically a large number of sets instead of doing the process described above individually by hand. This would allow to automate the selection of lines.

Facing the LCR method to these three different types of regions, that have incredibly different plasma temperature distributions and where not all the same lines are observable with the same ease has definitely allowed us to spot the challenges the LCR method faces and its short-comings. A more complete simulation of the noise will be made in the next chapter where we will provide a list of sets that could be useful to measure relative abundances using SPICE.

6

MEASURING RELATIVE ABUNDANCES WITH SPICE, THE EUV SPECTROMETER ON-BOARD SOLAR ORBITER

Context. *Linking solar activity on the surface and in the corona to the inner heliosphere is one of the main goals of Solar Orbiter. Its unique combination of in-situ and remote sensing instruments can be used to shed light on this difficult task by, e.g., determining the source region of the solar wind measured in-situ at the spacecraft position.*
Aims. *As the LCR method is based on optimized linear combinations of only a few spectral lines, it can be telemetry efficient but still reliable. We wish to make these measurements with SPICE (SPectral Imaging of the Coronal Environment), the EUV spectrometer on board Solar Orbiter.*
Methods. *We test different sets of spectral lines for relative FIP bias diagnostics using the methods described in previous chapters. We model different types of random noise and use an estimation of the systematic errors brought in by the calibration of the instrument to determine the impact noise has on the sets of lines we tested.*
Results. *We present some examples of abundance diagnostics that can be applied to data from SPICE.*

6.1 INTRODUCTION

Solar Orbiter was launched on February 10th 2020. This mission is like no other since it will get very close to the Sun, up to 0.28 AU, and will allow for out-of-ecliptic

imaging of the Sun. Solar Orbiter's orbit will go up to 32 degrees off of the ecliptic plane, which is very exciting since it will provide the first direct images of the solar poles. In its payload it carries 4 in-situ instruments and 6 remote sensing instruments. They will allow us to take a look at what is going on at the Sun itself and also in the heliosphere. The main question Solar Orbiter seeks to answer is how does the sun create and control the heliosphere and how solar activity changes with time. To answer this question, the scientific objectives of Solar Orbiter were chosen to be broad and, they include determining the processes responsible for the heliospheric magnetic field, how SPEs are accelerated and transported, understanding what causes CMEs, their evolution and interaction with the SW but also determining the sources of SW.

From a remote sensing point of view, clues to answer these questions will arrive in the form of vector magnetic fields, line of sight velocities, and imaging and spectroscopy of the solar corona in different wavelengths, on and off-disk. From an in-situ point of view, we will get different measurements for energetic particles, magnetic and electric fields, different types of waves and information about the protons, electrons and heavy ions populating the heliosphere. Putting all of these resources together we might be able to come up with some answers.

We will focus, as we have throughout this thesis, on one of the many ways in which the different instruments on board Solar Orbiter can be used to answer these fundamental questions. We are interested in creating a link between the Sun and the heliosphere, and more specifically between the SW and its origin. We believe we can achieve this through plasma composition diagnostics. With Solar Orbiter being closer to the Sun, establishing a physical connection between the spacecraft and the solar atmosphere will be easier, many tools are currently being developed to that aim [Rouillard et al., 2019]. The ten instruments Solar Orbiter has on board will give us a complete description of the SW, they will allow us to determine its origin, transport and composition [Auchère et al., 2020, Walsh et al., 2020]. The Spectral Imaging of the Coronal Environment (SPICE) instrument [Anderson et al., 2019] will in particular provide observations going from the upper chromosphere to the corona, with many transition region lines, allowing us to investigate solar phenomena at different heights. SPICE is the high-resolution imaging spectrometer on board Solar Orbiter. SPICE will provide temperature, density, flow and composition information for the observed coronal plasma. These composition measurements can be compared to those made in-situ not only by Solar Orbiter's Solar Wind Analyser [SWA; Owen et al., 2020]) but also to those made by in-situ instruments of other missions such as Parker Solar Probe [PSP; Fox et al., 2016]), the Search for Exospheric Refilling and Emitted Natural Abundances [SERENA; Orsini et al., 2010]) instrument package on board BepiColombo [Benkhoff et al., 2010], or the Solar Wind Ion Mass Spectrometer [SWICS; Gloeckler

et al., 1998] instrument on board the Advanced Composition Explorer [ACE; Stone et al., 1998]), and help us pinpoint the source region of the plasma reaching the spacecraft.

Given the very particular orbit of Solar Orbiter, telemetry will be limited and therefore we will mostly retrieve observations of spectra of a few selected spectral lines. This is why we think the LCR method will be of great help as we have seen that sometimes as little as four spectral lines can give us relative abundance measurements. In this chapter we will briefly describe the SPICE imaging spectrometer, explain how we simulate noisy radiances given the performance of the instrument and provide three sets of spectral lines that could be used for relative abundance measurements. The results of the tests done on these sets and the posterior probability distributions will be provided, in the same way as in the previous chapter. We will end by showing a few tests performed using a simulation of an active region in order to understand if and how different EMs can affect our measurements of relative FIP biases.

6.2 SPECTRAL IMAGING OF THE CORONAL ENVIRONMENT

SPICE is a high resolution imaging spectrometer. It operates at two ultraviolet wavelength ranges: 704 Å to 790 Å and 973 Å to 1049 ÅṪhis wavelength range allows SPICE to scan plasma from the low chromosphere to the flaring corona and thus provide quantitative knowledge of the physical properties of the observed plasma. The physical quantities that the observation of these lines will supply include plasma temperature, emission measure, flow velocities, relative abundances and it will also reveal the presence or not of plasma turbulence. This will help investigating the relationships between all the observed layers of the solar atmosphere. SPICE's high resolution is also ideal to observe the fine-scale structure of the solar atmosphere. The observations carried out by this spectrometer will enlighten us on different science questions regarding solar phenomena such as how CMEs evolve through the corona, how they contribute to solar magnetic flux and helicity balance, how and where shocks form in the corona, how and where energetic particles accelerate and are released from their sources, how magnetic flux is transported and what are its properties at high solar latitudes, and, what are the source regions, the heating and accelerating mechanisms of the SW.

The optical paths for SPICE are shown in Fig. 6.2.1. Sun light enters and travels to a off-axis parabolic mirror designed to minimise the absorption of solar radiation while maximizing reflectivity in the extreme UV. The mirror reflects the EUV radiation towards and forms an image at the slit which then traverses to the grating. This is a concave toroidal variable line space grating specially designed to disperse EUV light,

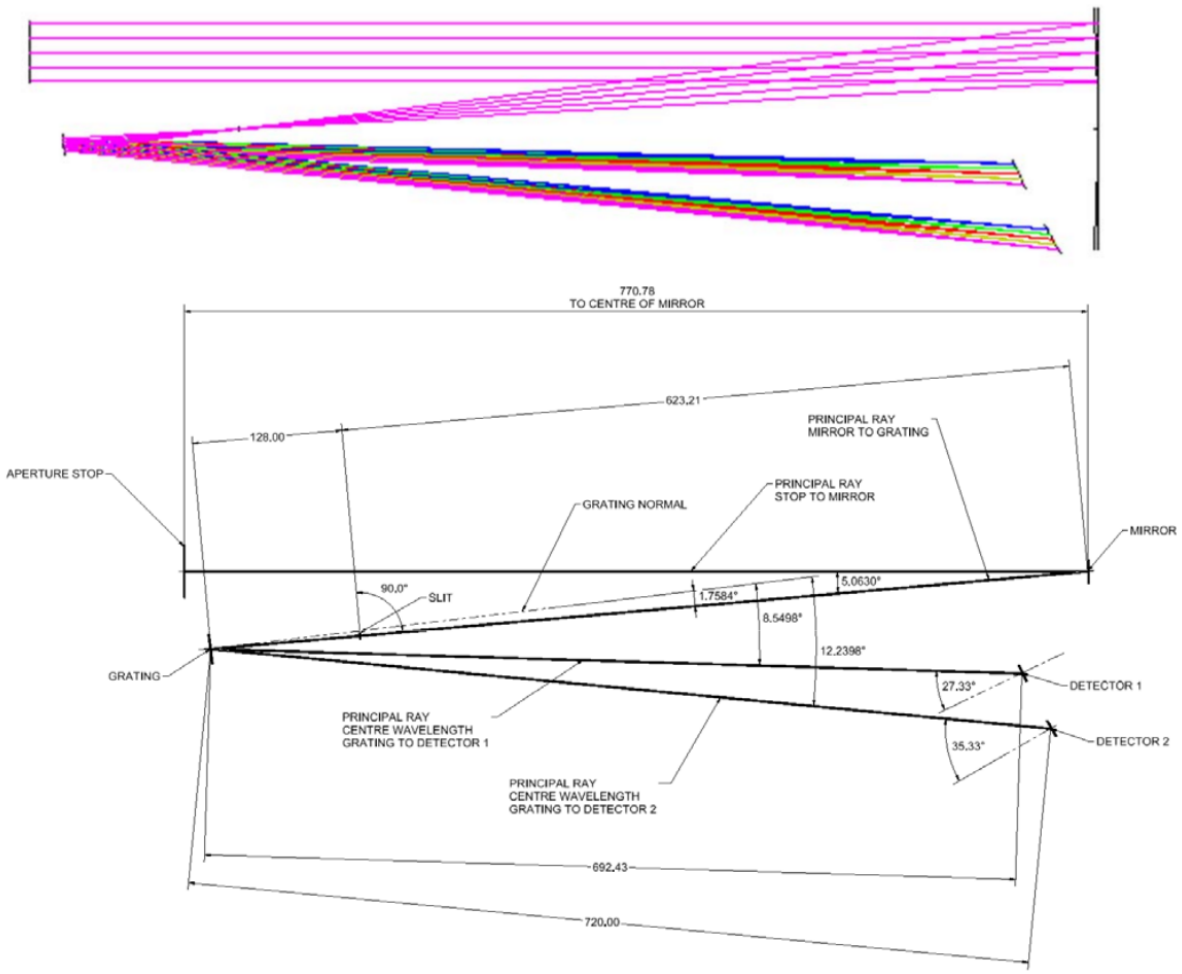

Figure 6.2.1: Scheme of the optical path followed by the observed light within the SPICE instrument, SPICE-user-manual version 8.0.

magnify it and re-image it onto two 2D array detectors. Detector 1 and detector 2 correspond to our short wavelength (SW: 704 Å to 790 Å) and long wavelength (LW: 973 Å to 1049 Å) ranges, they consist of 1024 spatial times 1024 spectral pixels each. When carrying out an observation, both detectors function simultaneously. Once the region of the Sun we want to observe is selected, the spacecraft will point to it and the grating will disperse the spectrum of the thin rectangular area that makes it into the slit onto both detectors. SPICE has four slits with varying widths at 2", 4", 6", and 30". The analysis of the 2D images that can be obtained using the 30" slit will not be discussed in this thesis. We will only focus on spectral images obtained by recording line-spectra. In this case, in order to cover the entire desired area (a wider rectangle), the instrument will raster the slit image across the field of view by rotating the primary mirror. This will give us in the end a 3 dimensional data cube with two spatial dimensions and one spectral dimensions.

A science observation plan for SPICE is called a study. Often we will not take full spectrum observations and therefore have to chose the spectral windows we will observe. Each study is defined by its slit choice, the selected exposure time, the scan mirror start, stop and increment information and the so called camera-plane which includes the windows position, size, binning and compression parameters (to fit within available resources for data down-link, the SPICE science data is compressed on-board).

We will focus on obtaining relative FIP bias maps using the radiances of spectral lines and the LCR method. The spectral lines we will observe with SPICE are emitted by ions that form between 10 000 K and 10 MK. The contribution functions of the strongest observable lines are depicted in Fig. 6.2.2. As we can see, we cover a broad range of temperatures, we have spectral lines from high FIP elements emitting at all temperatures. We do have fewer lines from low FIP elements overall and none with a temperature peak around 10^5 K. At this temperature, we will have to compare the emission from low FIP elements to the intermediate FIP element sulfur.

6.3 SIMULATING NOISY SPECTRA

Observations are mainly affected by random errors. These can be caused for example by Poisson photon shot noise or nearly Gaussian detection noises like thermal and read noise. These noises vary randomly from pixel to pixel and from exposure to exposure. On the contrary, the interpretation of all observed intensities is skewed by the same amount and in the same direction by the systematic errors made on the calibration and atomic physics. These are much harder to estimate than the previous random noises. Estimating the properties of the probability distributions of the systematic

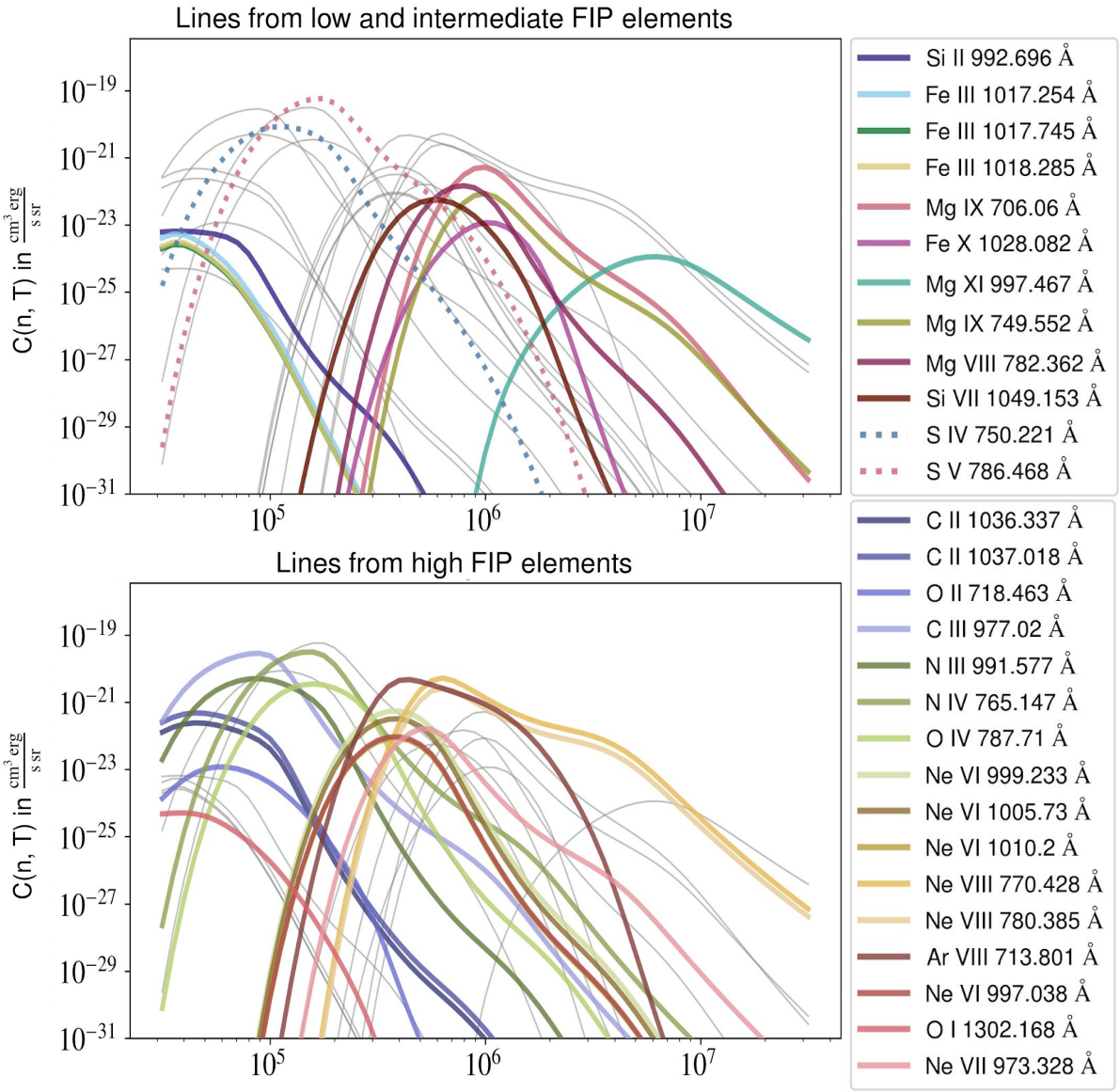

Figure 6.2.2: Contribution functions of the strongest observable spectral lines by SPICE. Similarly to Fig. 5.2.3, the top panel shows the lines from low FIP elements in color and the dotted colored lines correspond to lines from intermediate FIP elements. The fainter grey lines in the back are from intermediate and high FIP elements. In the lower panel the full lines in color correspond to lines from high FIP elements. In the same fashion as at the top, the fainter grey lines in the back are from low and intermediate FIP elements.

errors would require a detailed analysis of the calibration process and of the atomic physics data models. This goes beyond the scope of this thesis. SPICE being still so young, we still have a long way to go with the calibration of the instrument.

In this chapter, we will solely focus on the observation noises and see how their distributions affect the measurements. In the near future we could approximate systematics by assuming for example an uncertainty of 20% to 25% with a Gaussian distribution for the atomic physics and a similar distribution for the calibration. Such approximations have been previously assumed in the litterature [Guennou et al., 2012a].

When observing the corona with a spectrometer, the number of photons of energy $h\nu$ detected in a pixel of our instrument will depend on its sensitivity which can be summarized in its effective area $A_{eff}(\lambda)$, a function of the observed wavelength, but also on other characteristics of the observation such as the exposure time Δt and the solid angle observed which accounts for the angular size Ω of a pixel and that of the slit used:

$$N_{ph} = \frac{I_{ij}}{h\nu} \Delta t \, A_{eff}(\nu) \, \Omega. \tag{6.1}$$

These photon intensities are perturbed by Poisson noise. We can convert them into digital numbers (DN) by multiplying them by the gain of the instrument. The noise associated to the dark current I_{dark} also has a Poisson distribution, it will vary with the exposure time, whether we are binning the data or not, and the width of the spectral window we observe. The background level I_{bkgd} is also a signal so the noise associated to it also follows a Poisson distribution. The reading noise Δn_{read} is considered to have a Gaussian distribution. The characteristics of the observation and the instrument define how we parametrize these distributions when drawing random samples. Values for I_{dark}, I_{bkgd}, and Δn_{read} are listed in Table 6.3.1, they were taken from the latest SPICE scientific performance report. We add all of these noises (all in DNs) to obtain a noisy signal. Then we add together the averages of all noise sources to amount to *pure noise* (dark current + background + reading; in DNs as well). Our noisy radiance will be the result of the subtraction of this pure noise to the noisy signal which we can express in physical units before using it to compute the relative FIP bias.

6.4 SPECTRAL LINES

We tested a variety of spectral lines and the ones we selected to try out in future observations are listed in Table 6.3.2.

Set A corresponds to a comparison between nitrogen and sulfur, using sulfur here as our low FIP element since no low FIP elements show spectral lines in the same temperature range as the N III and N IV lines we selected. We used the test developed

Characteristic	Notation	Value	Unit
Dark current	I_{dark}	2.4	DN / s / pixel
Read noise	Δn_{read}	6.9	DN / pixel
Background noise	I_{bkgd}	1.0	photons / s / pixel

Table 6.3.1: Instrument characteristics used to simulate noise, from the SPICE scientific performance report. The more observations we do with SPICE, the better we will be able to evaluate this values, we should adopt the updated values when available.

Set #	Ion	Wavelength (Å)	log T_{max} (K)	QS radiance $mW\,m^{-2}\,sr{-}1$
A	**N III**	**991.577**	5.0	32.6
	N IV	**765.147**	5.2	52.7
	S IV	750.221	5.0	4.4
	S V	786.468	5.2	19.3
B	**Ne VIII**	**770.428**	5.8	54.7
	Mg VIII	782.362	5.9	16.2
	Mg IX	706.06	6.0	5.5
	Mg IX	749.552	6.0	7.6
C	**Ne VII**	**973.328**	5.7	2.5
	Ne VIII	**770.428**	5.8	54.7
	Si VII	1049.153	5.7	1.8

Table 6.3.2: Sets of spectral lines we tested for SPICE. The table shows three different sets of spectral lines, including the ions emitting them, their wavelengths, the temperature of maximum emission T_{max}, and typical radiances of these lines in the quiet Sun from the Curdt et al. [2001] atlas.

in Sec. 3.2, as we have throughout this thesis, on this set of lines. We did so with an AR and a CH EMs. The results are shown in the left panel of Figs. 6.4.1 and 6.4.2 respectively. We obtain a uniform FIP bias map with a very narrow histogram with values very close to the imposed relative FIP bias.

Set B corresponds to a linear combination of magnesium lines that we will compare to a neon line. They were tested using the same protocol. We can see in Figs. 6.4.1 and 6.4.2 that relative FIP bias values obtained vary more with this set than with the previous one. The hotter the plasma, the broader the histogram.

Set C is a set of spectral lines that was initially proposed by Hardi Peter as a possibility in a SPICE meeting in 2015. His idea of combining two neon lines to compare to a silicon one was what sparked the LCR method, which is a generalization of that idea. Here once again we see more variation when the plasma is hotter. In the case of the CH, the map obtained is fairly uniform except for the two bottom left and upper right corner areas where the plasma is hotter and at the center of the AR we underestimate the relative FIP bias. This is because of the slope of the contribution functions of the neon lines at high temperature (see Fig. 6.2.2). We can possibly use this set with confidence when looking at colder plasma, closer to the temperature of the maximum of the contribution function of the Si VII line, but we should be cautious. A set of lines fit for plasma temperature diagnostics could be observed in conjunction to this set and inform where this diagnostic can be trusted and where it cannot.

To plot $P(f_p \mid f_i)$ as we have done before, we used typical radiances observed in the quiet Sun for I_{ij}. The values are listed in Table 6.3.2, they come from the spectral atlas of Curdt et al. [2001] which used observation from the SUMER spectrometer on board SOHO. We simulated the noise for an observation that would be carried out with the 6" slit, binning in the y direction over 4 pixels and with an exposure time Δt of 2 minutes. An example of a figure similar to the left two plots of Fig. 4.3.4 is shown in Fig. 6.4.3 where, on the left, we have simply a 200 $\times$ 200 uniform DN map for this particular study and for the spectral line from ion N IV and, on the right, we have noisy radiances. We drew 40 000 I_{ij}^{obs} for each spectral line (we did so for each type of noise and added them to the uniform DN map), same as in the previous chapter. We followed the same steps as well to obtain the conditional probability distribution which are plotted for each set as well as the contours defining our credible intervals.

Set A presents a very narrow $P(f_p \mid f_i)$. We can see that this diagnostics leads to systematically underestimating the relative FIP bias between sulfur and nitrogen. The probability distributions will allow us to know which f_p value is most probable even though it will be different from the f_i measured.

Set B has a very unusual $P(f_p \mid f_i)$. At first glance, it seems like a broader version of the one obtained for set A except the f_i values are very high. A zoom to the [-10,50]

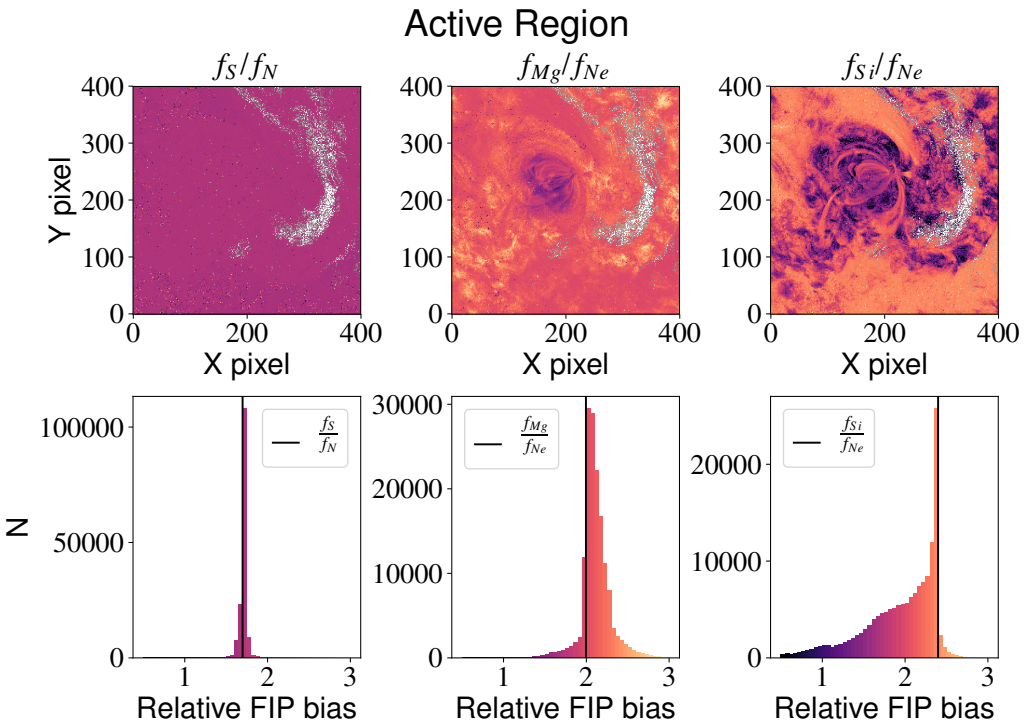

Figure 6.4.1: Tests of Sec. 3.2 on the three sets listed in Table 6.3.2 using an AR EM. Top panels are the retrieved relative FIP bias maps, bottom panels are the corresponding histograms, the black lines in the histograms correspond to the imposed relative FIP biases. The two panels at the left correspond to set A (sulfur and nitrogen spectral lines), the middle ones to set B (magnesium and neon spectral lines), and the right ones to set C (silicon and neon spectral lines).

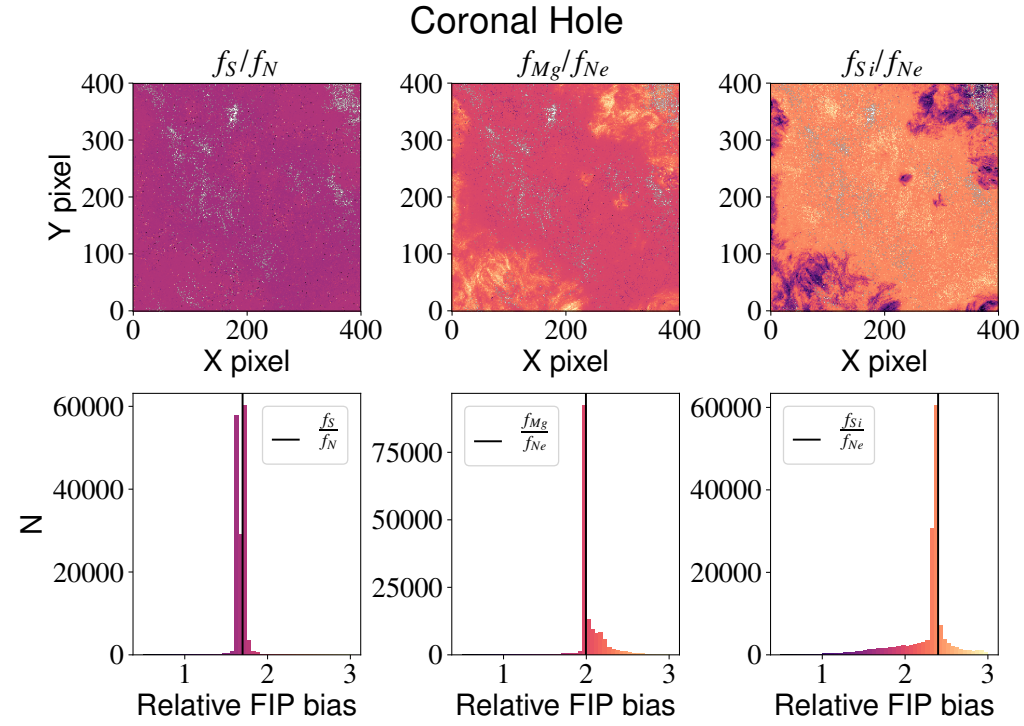

Figure 6.4.2: Same as Fig. 6.4.1 but for a CH EM.

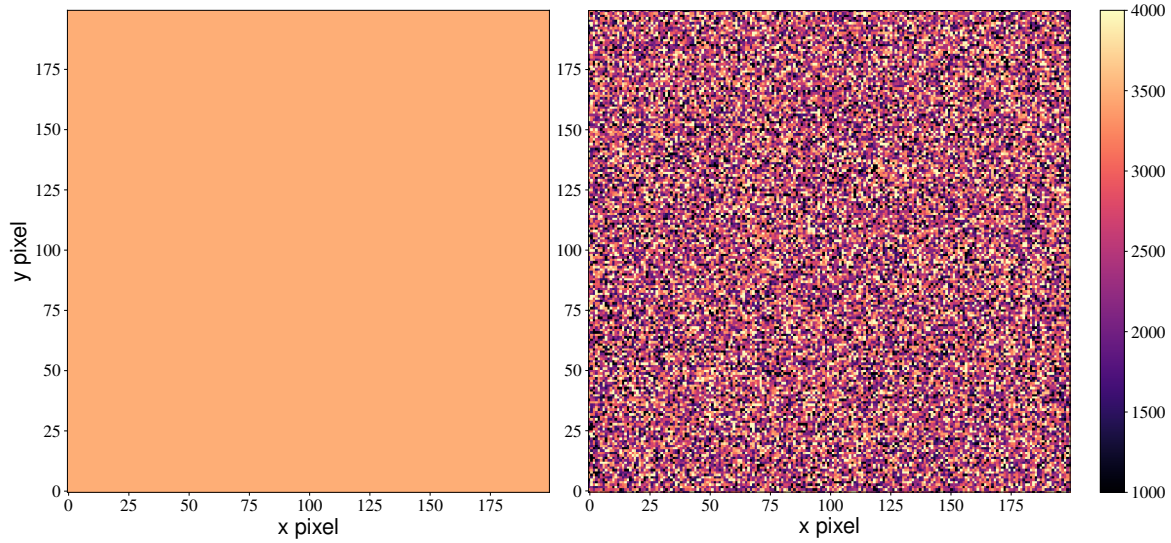

Figure 6.4.3: Examples of the noise simulation for the N IV 765 Å spectral line. Uniform DN map on the left. We drew 40 000 random variables for each type of noise and added them to the uniform DN map to simulate noise, depicted on the right. Calculations performed for an observation with an exposure time of 2 minutes, the 6" slit and a binning in the y direction of 4.

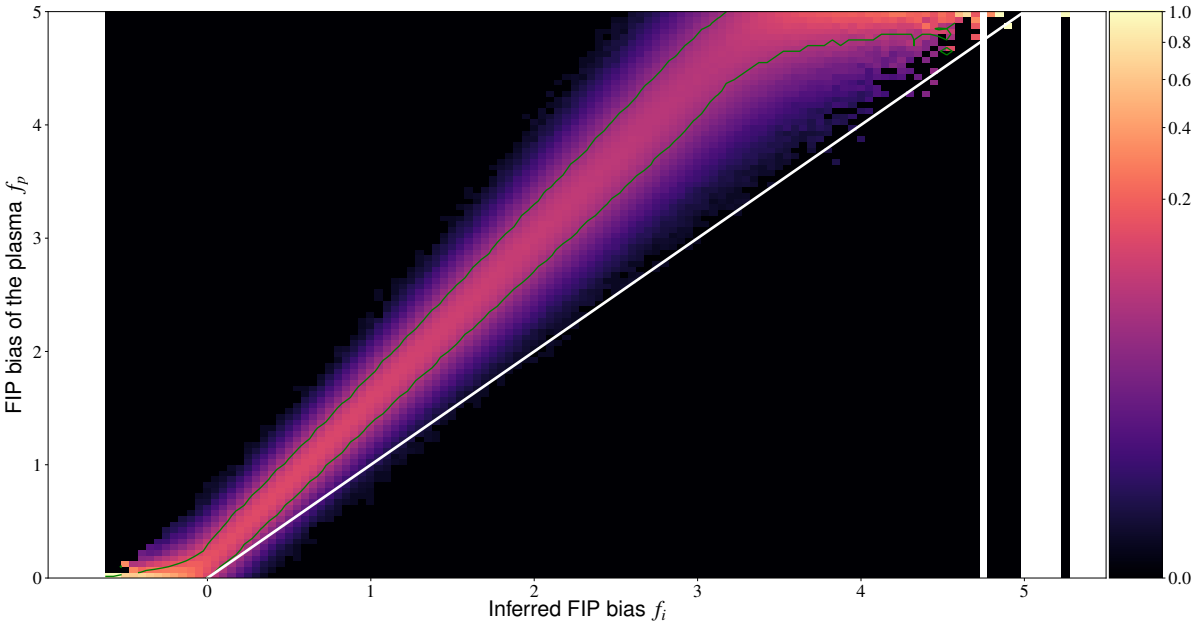

Figure 6.4.4: Conditional probability of the plasma having, on the ordinates, a given relative FIP bias (f_p) knowing the inferred relative FIP bias obtained from observations (f_i), on the abscissa, using the LCR method on set A. Probability distribution obtained for f_p varying from 0.0 to 5.0 and a prior probability distribution $P(f_p)$ uniform between 0.0 and 5.0. The white line is the first bisector, where both values are equal. The green contour corresponds to the 75% credible interval computed for each value of f_i. The white vertical columns correspond to f_i bins where no f_i values were obtained.

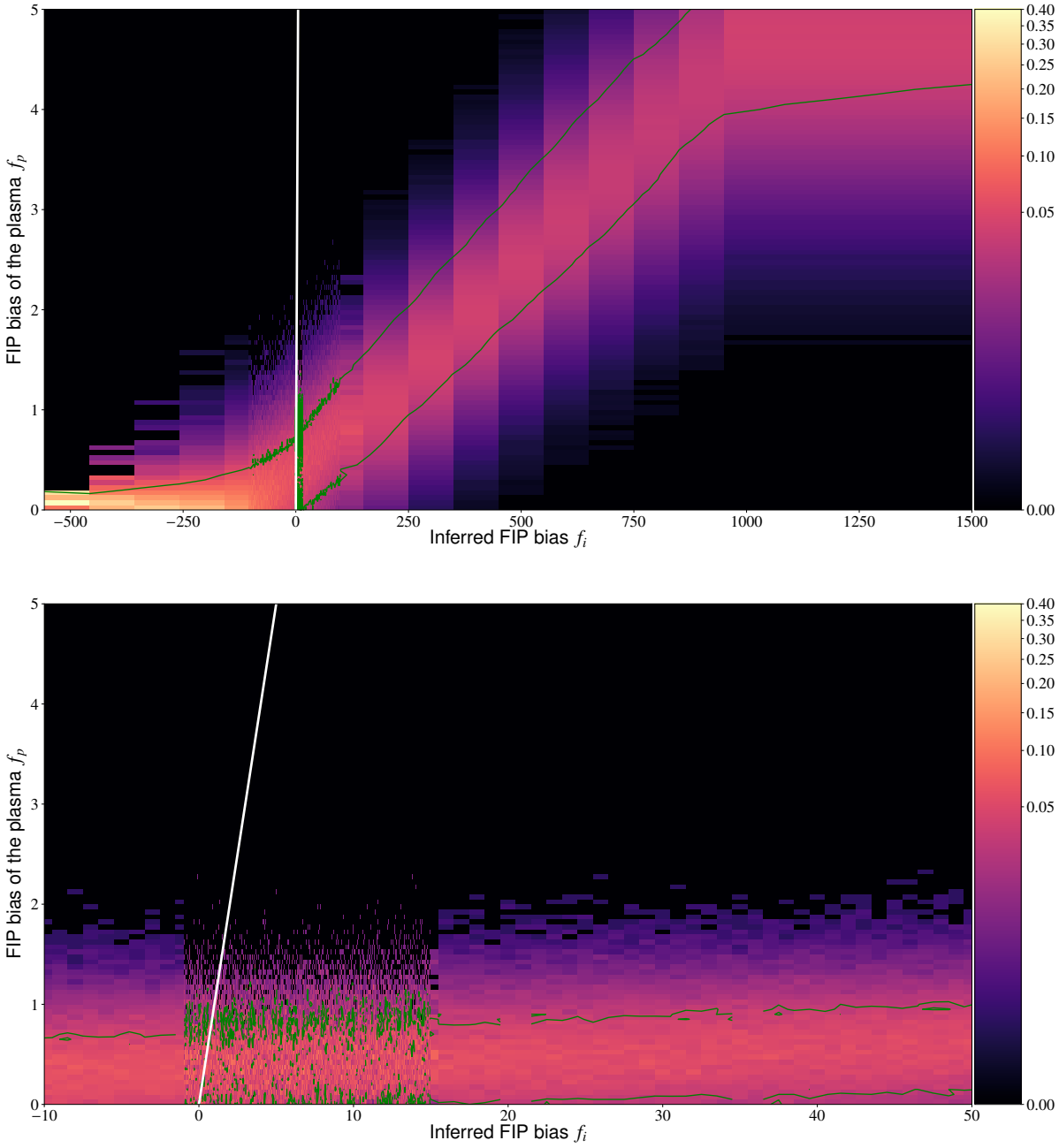

Figure 6.4.5: Top: Same as 6.4.4 but for set B. Bottom: Zoomed version in the [-10,50] range.

range shows a uniformly distributed probability distribution in f_i, the slope of the green top and bottom of the contour being almost flat. We have not been able to draw any conclusion as to why it looks like these. Further analysis is necessary.

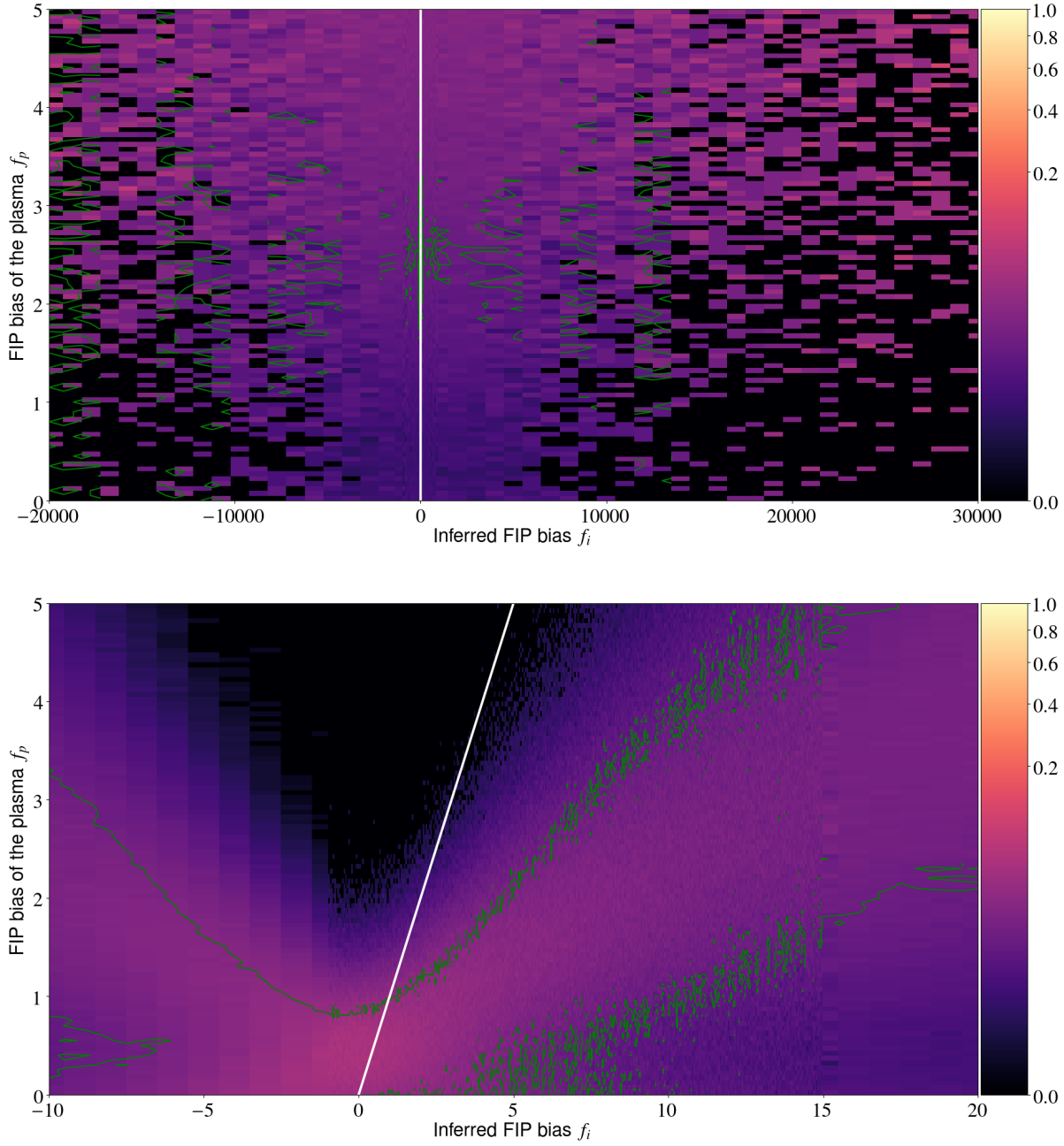

Figure 6.4.6: Top: Same as 6.4.4 but for set C. Bottom: Zoomed version in the [-10,50] range.

Set C also has an unexpected $P(f_p \mid f_i)$. We obtain very high and very low f_i values. This is because the Si VII and the Ne VII lines are much fainter than the other neon line used and carry with them a lot of noise. We might also be overestimating the background noise, more observations and tests with SPICE will help us determine this value better. Upon closer examination, by zooming to the [0, 20] range, we see

that in this range of f_i's we might be able to distinguish photospheric from coronal abundances but the contours are still pretty broad in f_p.

6.5 USING A SIMULATED AR

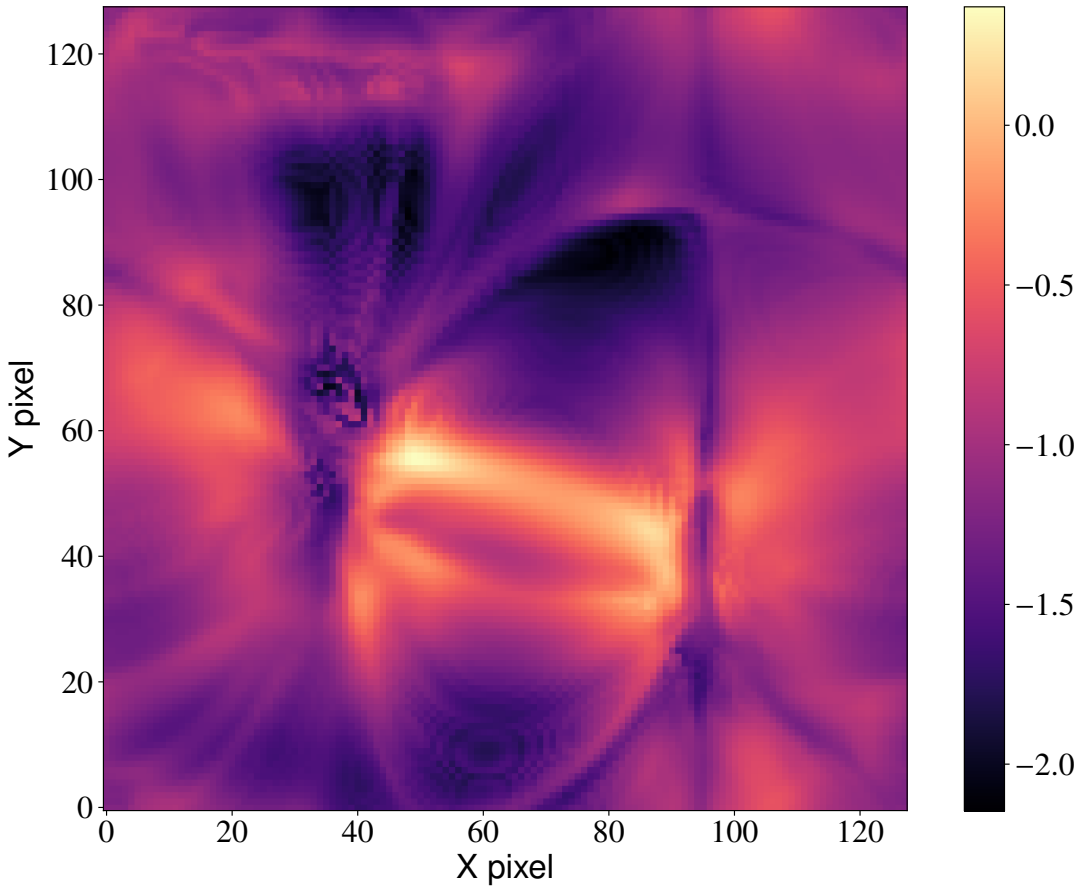

Figure 6.5.1: Log of the simulated radiance of the Si VII 1049 Å line. Radiance in erg / cm^2 / s / sr.

We wanted to use 3D simulations in order to confront the LCR method to EMs with shapes that are very different to the ones we have previously used. Although this is still a work in progress, here we simulate radiances of the AR simulated by Bingert and Peter [2011] and then perform relative FIP bias measurements with the LCR method. This simulation is based on a single fluid MHD model. The data was provided to us by Hardi Peter during a three week long visit I did at the Max Planck Institute for Solar System Research during May 2019. An example of how a line's simulated radiance in this AR looks like is presented in Fig. 6.5.1 for the Si VII 1049 Å line. We have a density cube and a temperature cube. We compute the radiance by selecting only the cells that we consider contain coronal plasma. This is simply defined for the moment as cells having an electron density $n_e < 10^{9.5}$ cm^3. We can evaluate

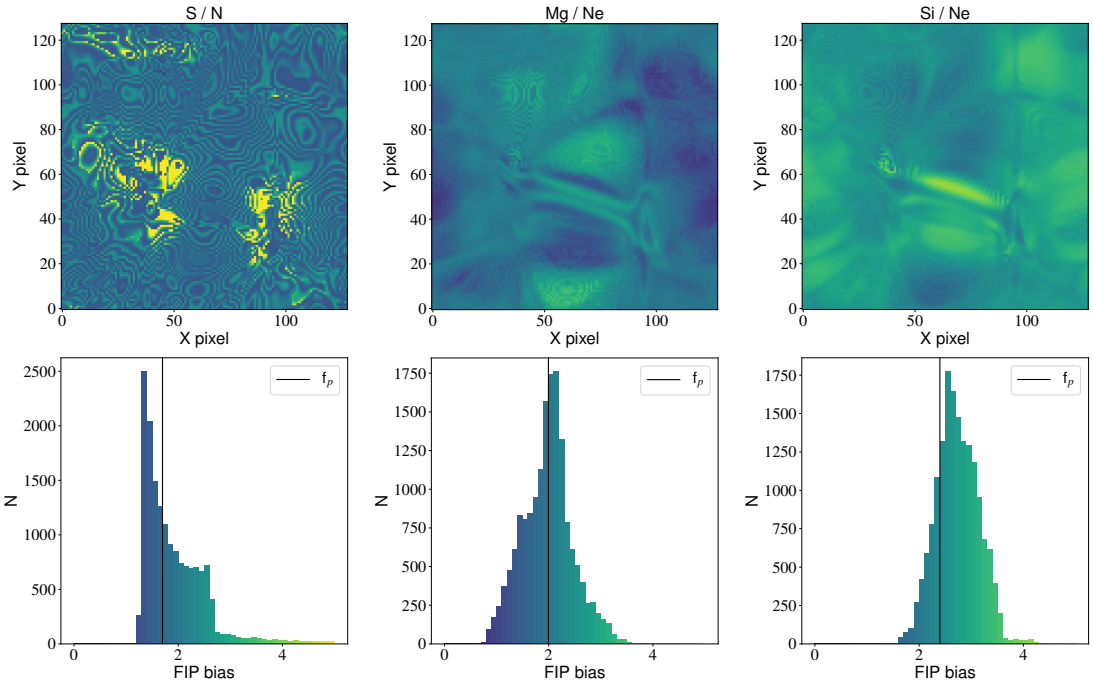

Figure 6.5.2: Relative FIP bias maps (top) obtained for sets A (left), B (middle), and C (right) and their corresponding histograms (bottom). The imposed relative FIP biases correspond to the black vertical lines in the histograms.

the contribution function of the line in every cell and using Eq. (2.3) we integrate along the line of sight to obtain the radiance of the line.

We can impose a uniform FIP bias in every single cell of the simulation and then retrieve relative FIP bias maps by integrating along a selected line of sight. This approach ensures that any deviation from uniformity comes from the impact of the thermal structure of the plasma along the line-of-sight on our linear combination ratio. This allows to see the possible dependence on temperature or on the DEM that a set might have given the shapes of the contribution functions of the lines. To compute the relative FIP bias, we compute the radiance of each spectral line, we compute the average density of the plasma we deemed as coronal, this density value is then used to obtain the coefficients of the linear combinations and we finally compute the LCR. The relative FIP bias maps obtained are shown in Fig. 6.5.2. The histograms we obtain are broader than those obtained with our previous tests. The FIP bias map obtained for the nitrogen to sulfur comparison is unusual looking, it is probably linked to how we defined coronal plasma. When we compute the relative FIP bias maps assuming that the corona has a maximum density of $n_e < 10^8$ cm^3 results differ. This is something we need to investigate further.

6.6 DISCUSSION

More analysis needs to be done to understand what leads to such different results when using EMs from AIA, EMs from simulations and radiances with simulated noise. Given the results of the AIA tests we had with the sets of silicon and magnesium lines, we still believe we can do something with them. We plan to observe these three sets during the Solar Orbiter Remote Sensing Checkout Window planned in the week of the 16^{th} of November 2020 and hopefully what we will learn from these observations will help us figure out exactly what is going on.

When using the simulation data, we assumed that the AR structure is at the center of the solar disk so we integrate along the height above the photosphere but it would be interesting to try other lines of sight. It can help us determine if the point of view can affect our relative FIP bias determination. It can also be helpful in determining the consequences of assuming that the abundances are constant along the line of sight by purposefully imposing non-uniform abundances along the line of sight.

Given the limited telemetry and spectral range available with SPICE, lines that provide density information might not be available. In this case, we can provide $P(f_p \mid f_i)$ for a range of density values so that we can have an idea of what the real FIP bias might be even if we are not sure of the density of the emitting plasma. It is of course better to choose density insensitive lines but this might not be always possible.

In order to investigate transition region abundances, it would be perhaps better to use simulations which resolve better the structures at these temperatures and densities and do go low enough in the solar atmosphere, such as BIFROST [Gudiksen et al., 2011].

7

CONCLUSION

7.1 SUMMING IT ALL UP

The global properties of the heliosphere are quite well understood, however there are several aspects of the small scale features such as the source regions of the solar wind at the Sun that remain unknown. One way forward is by using composition data measured in situ and remotely. Indeed, different structures on the Sun have different abundances that become frozen at a certain height, and therefore we can determine where certain wind plasma detected in situ comes from. In some regions, the coronal abundance of elements that have a First Ionization Potential (FIP) lower than 10 eV is enhanced in comparison to the same element's photospheric abundance, while this is not the case for elements with a FIP higher than 10 eV. We call these changes in abundance the FIP effect. Comparing in-situ and remote sensing composition data, coupled with modeling, can therefore allow us to trace back the source of heliospheric plasma.

During the beginning of my PhD thesis, I focused on developing the Linear Combination Ratio (LCR) method to measure relative abundances of the solar corona using EUV spectroscopy. It can be telemetry efficient but still reliable and is based on optimized linear combinations of only a few spectral lines and, most importantly, requires no prior DEM inversion. This method relies on optimizing linear combinations of spectral lines. It could be used semi-automatically for optimal abundance determinations from existing observations as well as for designing new observations. This method has been thoroughly tested on synthetic spectra and on spectroscopic data. The proof of concept for the LCR method was published in Zambrana Prado and Buchlin [2019]. I also developed a Python module to compute the optimal linear combinations of spectral lines and to use them to compute relative FIP bias maps from observations, available at fiplcr. We applied the LCR method to spectroscopic observations of an active region previously been studied in Baker et al. [2013]. We selected the lines for our linear combinations and measured the relative FIP bias of a mix of iron and silicon and compared it to sulfur. The FIP bias maps obtained in Baker

et al. [2013] and by using the LCR method display similar FIP bias structures. We find that the LCR FIP bias map provides useful information on the FIP biases in the coronal structures in the field of view, which is remarkable given that it was produced without any DEM inversion.

I developed the LCR method further by designing a numerical procedure based on a statistical approach and the Bayes theorem to compute uncertainties of this FIP bias diagnostics. It can take into account uncertainties in the atomic physics and in the instrument calibration, and the different noise components in the data acquisition chain. It provides the probability distribution of the real FIP bias of the plasma given the measurement provided by the LCR method. This procedure has been particularly helpful to spot biases in the LCR method. It allowed us to rule out some sets of spectral lines we might have otherwise trusted if it were only up to the cost function to indicate which sets are usable and which are not.

I have the incredible opportunity of being part of the ISSI Team n.418 "Linking the Sun to the Heliosphere using composition and modeling" led by Susanna Parenti. The aim of the team is to propose a methodology for the connectivity between the heliospheric plasma and its source region at the Sun that makes use of both data and modelling, and which may have a direct application on the Solar Orbiter data [Parenti et al., in prep.]. To validate the method we use a corona active region jet event as a test case. The goal is to determine the plasma conditions at the source region of a jet, modeling the large scale corona and heliospheric environment and determining its in-situ composition and whether it reached 1 AU. My task was to provide relative abundance measurements using EIS observations of the AR from which the jet appeared. I was able to apply the LCR method on observations that were not intended for composition measurements in the first place. I provided relative FIP bias measurements at four different temperature ranges with most of my results being in agreement with relative FIP bias measurements obtained with a method that followed DEM inversion. Facing the LCR method and the uncertainty determination method to real observations was a great learning experience. It informed the steps we will take to better the method, particularly it shed light on the short-comings of the cost function we use to optimize the coefficients of the linear combinations.

The final part of my thesis consists on providing these abundance diagnostics and the characteristics of the observations we would have to carry out in order to obtain good enough composition maps with SPICE. Linking solar activity on the surface and in the corona to the inner heliosphere is one of the main goals of the ESA-NASA Solar Orbiter mission [Müller et al., 2013, 2020]. This mission has been designed to reduce the gap further between in-situ and remote sensing measures, by approaching the Sun up to about 0.3 AU. Its unique combination of in-situ and remote sensing instruments

can be used to shed light on this difficult task by, e.g., determining the source region of the solar wind measured in-situ at the spacecraft position. In particular, SPICE (SPectral Imaging of the Coronal Environment), the EUV spectrometer on board Solar Orbiter will observe the source regions at the Sun that will be sampled a few days after by the in-situ instruments. Approaching the Sun, the plasma and magnetic field properties are only partially modified by the local heliospheric environment, and the connectivity problem will thus have much reduced uncertainties. Observing only a few lines with SPICE, we should be able to obtain relative abundance maps of the observed regions on the Sun. Using atomic physics models of spectral line radiances, I have found at least one linear combination of SPICE lines to observe in order to obtain accurate relative FIP bias maps. Expanding on this effort can make relative abundance measurements routinely available for Solar Orbiter.

We plan to observe the linear combinations described in Chapter 6 during the Solar Orbiter Remote Sensing Checkout Window planned in the week of the 16^{th} of November 2020. This will allow the LCR method to be tested for the first time with real SPICE data and to be compared with other FIP bias diagnostics.

7.2 HOPES OF EXPANSION

As I have applied the LCR method to different spectrometers, I could understand some of the trade-offs required when designing an instrument, in particular when selecting the wavelength ranges of the proposed spectrometer. Indeed, one needs simultaneously a good enough spectral resolution (necessary to separate nearby or blended lines to obtain accurate radiance measurement required for abundance studies), and a spectral range wide enough to include strong enough spectral lines emitted at various temperatures and useful for various plasma diagnostics. In the case of EUV spectroscopic diagnostics of the FIP effect, this wavelength range should include lines from both low FIP and high FIP elements. EIS for example has a lot of low FIP lines, particularly from iron, but has a shortage on strong high FIP lines. SPICE on the other hand has more strong high FIP lines but has a shortage on low FIP lines, and, as we have seen, sometimes we will have to compare a high FIP element to an intermediate FIP element. However, the LCR method allows abundance diagnostics with fewer lines, thus making these diagnostics easier given the instrumental limitations.

The LCR method of course has its own limitations and short-comings as well. I would like to test out different cost functions, different EM sets to do the optimizations, perhaps even optimize the choice of the EM sets to different sets of lines depending on their contribution functions which naturally select a specific temperature range. A

better understanding of its biases is needed, particularly to be able to provide more sets for SPICE. We could also try to use lines that we know are blended and force the coefficients of both lines to be the same, this could be useful for instruments that have a spectral resolution that is insufficient.

I would also would like to explore the possibility of using the LCR method at higher temperatures with X-ray lines when the DEM formalism is still applicable, perhaps even adapt the LCR method to EUV instruments that look at other stars and see which lines we can use to measure the FIP biases of stellar coronae. This would help test the method in the case of the inverse FIP effect as well.

Lastly, another improvement to the LCR method that could be very useful is adopting an a priori distribution that is more realistic. We know that the Sun overall has more FIP effect than inverse FIP effect but we do not know in what proportion we have photospheric or coronal FIP biases. Changing the shape of $P(f_p)$ to reflect the actual distribution of relative FIP biases at the Sun could be done by performing regularly statistical studies of the relative FIP bias over the whole Sun. An example of a full Sun scan was carried out by Brooks et al. [2015] with the EIS spectrometer. The values obtained from this type of observations can give us a distribution of the FIP bias values at the Sun. This distribution will change with the solar cycle as the variability of composition and the Sun's magnetic field evolution seem to be linked [Brooks et al., 2017, Baker et al., 2018]. Seeing the changes in the distribution of relative FIP biases over the course of a cycle could help us better understand this link between magnetic activity and the FIP effect.

The study of abundances will not only allow us to determine the source regions of the solar atmosphere but it will also give us clues and input to understand heating mechanisms and mass-transport which keep puzzling solar physicists.

A

SYNTHÈSE EN FRANÇAIS

Diagnostics spectroscopiques de la composition élémentaire de la couronne solaire

Les propriétés globales de l'héliosphère sont assez bien comprises, mais plusieurs aspects des caractéristiques à petite échelle, telles que les régions sources du vent solaire à la surface du Soleil, restent inconnus. L'une des solutions consiste à utiliser les données de composition mesurées in situ et à distance. En effet, différentes structures sur le Soleil ont des abondances différentes qui se figent à une certaine altitude, et nous pouvons donc déterminer d'où provient un certain plasma du vent solaire détecté in situ. Dans certaines régions, l'abondance coronale des éléments qui ont un premier potentiel d'ionisation (FIP) inférieur à 10 eV est accrue par rapport à l'abondance photosphérique du même élément, alors que ce n'est pas le cas pour les éléments ayant un FIP supérieur à 10 eV. Nous appelons ces changements d'abondance l'effet FIP. La comparaison des données de composition in-situ et de télédétection, couplée à la modélisation, peut donc nous permettre de remonter à la source du plasma héliosphérique. D'ailleurs, les études d'abondance sont également importantes dans la couronne solaire car ces anomalies semblent être étroitement liées au chauffage coronal. Leur étude pourrait nous donner des indices pour nous aider à comprendre l'un des plus grands mystères de la physique solaire.

Au début de ma thèse de doctorat, je me suis concentrée sur le développement de la méthode du Linear Combination Ratio (LCR) pour mesurer les abondances relatives de la couronne solaire en utilisant la spectroscopie UV. Cette méthode, qui peut être efficace sur le plan de la télémétrie tout en restant fiable, est basée sur des combinaisons linéaires optimisées de quelques raies spectrales seulement et, surtout, ne nécessite aucune inversion préalable de la DEM. Elle pourrait être utilisée de manière semi-automatique pour déterminer de manière optimale l'abondance à partir d'observations existantes ainsi que pour concevoir de nouvelles observations. Cette méthode a été testée de manière approfondie sur des spectres synthétiques et sur des données spectroscopiques. La preuve de concept de la méthode LCR a été publiée dans Zambrana Prado and Buchlin [2019]. J'ai également développé un module Python pour calculer les combinaisons linéaires optimales de raies spectrales et les utiliser

pour calculer les cartes de biais FIP relatives à partir des observations, disponible sur fiplcr. Nous avons appliqué la méthode LCR aux observations spectroscopiques d'une région active qui avait été étudiée auparavant dans Baker et al. [2013]. Nous avons sélectionné les raies pour nos combinaisons linéaires et avons mesuré le biais FIP relatif d'un mélange de fer et de silicium et l'avons comparé au soufre. Les cartes de biais FIP obtenues par Baker et al. [2013] et en utilisant la méthode LCR montrent des structures de biais FIP similaires. Nous constatons que la carte de biais du FIP obtenue par la méthode LCR fournit des informations utiles sur les biais du FIP dans les structures coronales du champ de vue, ce qui est remarquable étant donné qu'elle a été produite sans aucune inversion de la DEM.

J'ai poursuivi le développement de la méthode LCR en concevant une procédure numérique basée sur une approche statistique et le théorème de Bayes pour calculer les incertitudes de ce diagnostic de biais FIP. Elle peut prendre en compte les incertitudes de la physique atomique et de l'étalonnage de l'instrument, ainsi que les différentes composantes du bruit dans la chaîne d'acquisition des données. Elle fournit la distribution de probabilité du biais FIP réel du plasma étant donné la mesure fournie par la méthode LCR. Cette procédure a été particulièrement utile pour repérer les biais dans la méthode LCR. Elle nous a permis d'exclure certains ensembles de raies spectrales auxquels nous aurions pu faire confiance si nous nous étions contentés uniquement des valeurs de la fonction de coût après optimisation des combinaisons linéaires de raies.

J'ai eu l'incroyable opportunité de faire partie de l'équipe ISSI n.418 "Linking the Sun to the Heliosphere using composition and modeling" dirigée par Susanna Parenti. Le but de l'équipe est de proposer une méthodologie pour la connectivité entre le plasma héliosphérique et sa région source au Soleil qui utilise à la fois les données et la modélisation, et qui pourrait avoir une application directe sur les données de Solar Orbiter [Parenti et al., in prep.]. Afin de valider cette méthode, nous utilisons un jet coronal issu d'une région active comme cas d'essai. L'objectif est de déterminer les conditions physiques du plasma dans la région source du jet, en modélisant la couronne à grande échelle comme à petite échelle ainsi que l'environnement héliosphérique, en déterminant la composition in situ, et finalement en essayant de déterminer si ce jet a atteint 1 UA. Ma tâche consistait à fournir des mesures d'abondances relatives dans la couronne en utilisant les observations EIS de la région active d'où le jet est apparu. J'ai pu appliquer la méthode LCR sur des observations qui n'étaient pas destinées à des mesures de composition au départ. J'ai fourni des mesures relatives du biais FIP dans quatre plages de température différentes, la plupart de mes résultats étant en accord avec les mesures obtenues avec une méthode qui se sert d'une inversion de la DEM. Confronter la méthode LCR à des

observations réelles a été une grande expérience d'apprentissage. Cela nous a permis de mieux définir les mesures que nous allons prendre pour améliorer la méthode; en particulier, cela a mis en lumière les lacunes de la fonction de coût que nous utilisons pour optimiser les coefficients des combinaisons linéaires.

La dernière partie de ma thèse consiste à fournir ces diagnostics d'abondance et les caractéristiques des observations que nous aurions à effectuer pour obtenir des cartes de composition satisfaisantes avec SPICE. Lier l'activité solaire à la surface et dans la couronne à l'héliosphère est l'un des principaux objectifs de la mission Solar Orbiter [Müller et al., 2013, 2020]. Cette mission a été conçue pour réduire davantage l'écart entre les mesures in-situ et de télédétection, en approchant le Soleil jusqu'à environ 0,28 UA. Sa combinaison unique d'instruments de mesure in-situ et de télédétection peut être utile dans cette tâche difficile, par exemple en déterminant la région source du vent solaire mesuré in-situ à la position de l'engin spatial. En particulier, SPICE (SPectral Imaging of the Coronal Environment), le spectromètre EUV à bord de Solar Orbiter, observera des régions sources au Soleil qui seront échantillonnées quelques jours après par les instruments in-situ. Plus près du Soleil, les propriétés du plasma et du champ magnétique ne sont que partiellement modifiées par l'environnement héliosphérique local, et le problème de connectivité aura donc des incertitudes beaucoup plus réduites. En n'observant que quelques raies avec SPICE, nous devrions pouvoir obtenir des cartes d'abondance relative des régions observées sur le Soleil. En utilisant les modèles de physique atomique des radiances des raies spectrales, j'ai trouvé les meilleures combinaisons de raies SPICE à observer afin d'obtenir des cartes d'abondance relative précises. Cet effort peut rendre les mesures d'abondance relative disponibles systématiquement pour Solar Orbiter.

Nous prévoyons d'utiliser les combinaisons de raies que j'ai obtenues lors de la Solar Orbiter Remote Sensing Checkout Window prévue dans la semaine du 16 novembre 2020. Cela permettra de tester pour la première fois la méthode LCR avec de vraies données SPICE et de la comparer avec d'autres diagnostics de biais FIP.

B

RESUMEN EN ESPAÑOL

Diagnósticos espectroscópicos de la composición elemental de la corona solar

Las propiedades globales de la heliosfera están bastante bien comprendidas, pero varios aspectos de las características a pequeña escala, como las regiones de origen del viento solar en el Sol, siguen siendo desconocidas. Una solución es utilizar los datos de composición medidos in situ y a distancia. De hecho, las diferentes estructuras del Sol tienen diferentes abundancias que se fijan a cierta altitud, por lo que podemos determinar de dónde proviene el plasma de viento solar detectado in situ. En algunas regiones, la abundancia coronal de los elementos que tienen un potencial de primera ionización (FIP por sus insignias en inglés) inferior a 10 eV aumenta en relación con la abundancia fotosférica del mismo elemento, mientras que no ocurre lo mismo con los elementos con un FIP superior a 10 eV. Llamamos a estos cambios en la abundancia el efecto FIP. La comparación de la composición in situ y los datos de teledetección, junto con la modelización, pueden por tanto permitirnos rastrear la fuente del plasma heliosférico. Además, los estudios de abundancia también son importantes en la corona solar porque estas anomalías parecen estar estrechamente relacionadas con el calentamiento de la corona. Su estudio podría darnos pistas para ayudarnos a entender uno de los mayores misterios de la física solar.

Al principio de mi tesis doctoral, me enfoqué en el desarrollo del método del cociente de combinación lineal (LCR por sus siglas en inglés Linear Combination Ratio) para medir las abundancias relativas de la corona solar usando la espectroscopia UV. Este método, que puede ser eficaz en términos de telemetría y al mismo tiempo seguir siendo fiable, se basa en combinaciones lineales optimizadas de sólo unas pocas líneas espectrales y, lo que es más importante, no requiere ninguna inversión previa de la DEM. Podría utilizarse de forma semiautomática para determinar de forma óptima la abundancia a partir de las observaciones existentes, así como para diseñar nuevas observaciones. Este método ha sido ampliamente probado en espectros sintéticos y datos espectroscópicos. La prueba de concepto del método LCR fue publicada en Zambrana Prado and Buchlin [2019]. También he desarrollado un módulo Python para calcular combinaciones lineales óptimas de líneas espectrales y usarlas para calcular

mapas de sesgo FIP relativo de las observaciones, disponibles en fiplcr. Aplicamos el método CRL a las observaciones espectroscópicas de una región activa que había sido previamente estudiada en Baker et al. [2013]. Seleccionamos las líneas de nuestras combinaciones lineales y medimos el bies relativo FIP de una mezcla de hierro y silicio y lo comparamos con el azufre. Los mapas de bies FIP obtenidos por Baker et al. [2013] y utilizando el método LCR muestran estructuras de bies FIP similares. Encontramos que el mapa de bies FIP obtenido mediante el método LCR proporciona información útil sobre los bies FIP en las estructuras coronales del campo de visión, lo cual es notable dado que fue producido sin ninguna inversión de la DEM.

He continuado el desarrollo del método LCR diseñando un procedimiento numérico basado en un enfoque estadístico y en el teorema de Bayes para calcular las incertidumbres de este diagnóstico de bies FIP. Puede tener en cuenta las incertidumbres de la física atómica y la calibración de los instrumentos, así como los diferentes componentes de ruido en la cadena de adquisición de datos. Proporciona la distribución de probabilidad del verdadero bies FIP del plasma dada la medición proporcionada por el método LCR. Este procedimiento ha sido particularmente útil para identificar los sesgos en el método LCR. Nos permitió excluir algunos conjuntos de líneas espectrales en los que podríamos haber confiado si hubiéramos estado satisfechos sólo con los valores de la función de costo después de la optimización de las combinaciones lineales de líneas.

Tengo la increíble oportunidad de formar parte del equipo de la ISSI n.418 "Linking the Sun to the Heliosphere using composition and modeling" dirigido por Susanna Parenti. El objetivo del equipo es proponer una metodología para la conectividad entre el plasma heliosférico y su región de origen en el Sol que utilice tanto datos como modelos, y que podría tener una aplicación directa en los datos de los Orbitadores Solares [Parenti et al., in prep.]. Para validar este método, utilizamos un chorro coronal de una región activa como caso de prueba. El objetivo es determinar las condiciones físicas del plasma en la región de origen del chorro, modelando la corona a gran y pequeña escala, así como el entorno heliosférico, determinando la composición in situ, y finalmente tratando de determinar si este chorro ha alcanzado 1 AU. Mi tarea consistía en proporcionar mediciones de abundancia relativa en la corona utilizando las observaciones del EIS de la región activa de la que se originó el chorro. Pude aplicar el método LCR a observaciones que no estaban destinadas a mediciones de composición al principio. Proporcioné mediciones relativas del sesgo del FIP en cuatro rangos de temperatura diferentes, y la mayoría de mis resultados coinciden con las mediciones obtenidas con un método que utiliza una inversión DEM. Confrontando el método LCR a las observaciones reales fue una gran experiencia de aprendizaje. Nos permitió definir mejor los pasos que daremos para mejorar la metodología; en

particular, puso de relieve las deficiencias de la función de costo que utilizamos para optimizar los coeficientes de las combinaciones lineales.

La última parte de mi tesis consiste en proporcionar estos diagnósticos de abundancia y las características de las observaciones que tendríamos que realizar para obtener mapas de composición satisfactoria con SPICE. Vincular la actividad solar en la superficie y en la corona a la heliosfera es uno de los principales objetivos de la misión Solar Orbiter [Müller et al., 2013, 2020]. Esta misión fue diseñada para reducir aún más la brecha entre las mediciones in-situ y las de teledetección, acercándose al Sol a cerca de 0,3 UA. Su singular combinación de instrumentos de teleobservación e in situ puede ser útil en esta difícil tarea, por ejemplo, para determinar la región de origen del viento solar medido in situ en la posición de la nave espacial. En particular, SPICE (SPectral Imaging of the Coronal Environment), el espectrómetro EUV a bordo del Orbitador Solar, observará regiones fuente en el Sol que serán muestreadas unos días después por los instrumentos in situ. Más cerca del Sol, las propiedades del plasma y del campo magnético sólo se modifican parcialmente por el entorno heliosférico local, por lo que el problema de la conectividad tendrá incertidumbres mucho menores. Observando sólo unas pocas líneas con SPICE, deberíamos ser capaces de obtener mapas de abundancia relativa de las regiones observadas en el Sol. Utilizando modelos físicos de radiación atómica de líneas espectrales, he encontrado combinaciones de líneas SPICE para observar con el fin de obtener mapas precisos de abundancia relativa. Este esfuerzo puede hacer que las mediciones de abundancia relativa estén sistemáticamente disponibles para Solar Orbiter.

Planeamos usar las combinaciones de líneas que obtuve durante la Solar Orbiter Remote Sensing Checkout Window programada para la semana del 16 de noviembre de 2020. Esto nos permitirá probar por primera vez el método LCR con datos reales de SPICE y compararlo con otros diagnósticos de bies FIP.

BIBLIOGRAPHY

L. Abbo, L. Ofman, S. K. Antiochos, V. H. Hansteen, L. Harra, Y. K. Ko, G. Lapenta, B. Li, P. Riley, L. Strachan, R. von Steiger, and Y. M. Wang. Slow Solar Wind: Observations and Modeling. *Space Sci. Rev.*, 201(1-4):55–108, November 2016. doi: 10.1007/s11214-016-0264-1.

M. Anderson, Thierry Appourchaux, Frédéric Auchère, R. Cuadrado, J. Barbay, F. Baudin, Sarah Beardsley, K. Bocchialini, B. Borgo, Davide Bruzzi, Eric Buchlin, G. Burton, V. Blüchel, M. Caldwell, S. Caminade, Mats Carlsson, Werner Curdt, Jenny Davenne, Joseph Davila, and D. Müller. The solar orbiter spice instrument – an extreme uv imaging spectrometer. 09 2019.

M. J. Aschwanden. *Physics of the Solar Corona. An Introduction with Problems and Solutions (2nd edition)*. Springer, December 2004.

Martin Asplund, Nicolas Grevesse, A. Jacques Sauval, and Pat Scott. The Chemical Composition of the Sun. *ARA&A*, 47(1):481–522, September 2009. doi: 10.1146/annurev.astro.46.060407.145222.

F. Auchère, V. Andretta, E. Antonucci, N. Bach, M. Battaglia, A. Bemporad, D. Berghmans, E. Buchlin, and et al. Coordination within the remote sensing payload on the solar orbiter mission. *A&A*, 2020. doi: 10.1051/0004-6361/201937032. URL https://doi.org/10.1051/0004-6361/201937032.

D. Baker, L. van Driel-Gesztelyi, and L. M. Green. Forecasting a CME by Spectroscopic Precursor? *Sol. Phys.*, 276:219–239, February 2012. doi: 10.1007/s11207-011-9893-4.

D. Baker, D. H. Brooks, P. Démoulin, L. van Driel-Gesztelyi, L. M. Green, K. Steed, and J. Carlyle. Plasma Composition in a Sigmoidal Anemone Active Region. *ApJ*, 778:69, November 2013. doi: 10.1088/0004-637X/778/1/69.

Deborah Baker, David H. Brooks, Lidia van Driel-Gesztelyi, Alexander W. James, Pascal Démoulin, David M. Long, Harry P. Warren, and David R. Williams. Coronal Elemental Abundances in Solar Emerging Flux Regions. *ApJ*, 856(1):71, March 2018. doi: 10.3847/1538-4357/aaadbo.

Deborah Baker, Lidia van Driel-Gesztelyi, David H. Brooks, Gherardo Valori, Alexander W. James, J. Martin Laming, David M. Long, Pascal Démoulin, Lucie M.

Green, Sarah A. Matthews, Katalin Oláh, and Zsolt Kővári. Transient Inverse-FIP Plasma Composition Evolution within a Solar Flare. *ApJ*, 875(1):35, April 2019. doi: 10.3847/1538-4357/ab07c1.

Deborah Baker, Lidia van Driel-Gesztelyi, David H. Brooks, Pascal Démoulin, Gherardo Valori, David M. Long, J. Martin Laming, Andy S. H. To, and Alexander W. James. Can Subphotospheric Magnetic Reconnection Change the Elemental Composition in the Solar Corona? *ApJ*, 894(1):35, May 2020. doi: 10.3847/1538-4357/ab7dcb.

M. Banaszkiewicz, W. I. Axford, and J. F. McKenzie. An analytic solar magnetic field model. *Astronomy and Astrophysics*, 337:940–944, September 1998.

Johannes Benkhoff, Jan van Casteren, Hajime Hayakawa, Masaki Fujimoto, Harri Laakso, Mauro Novara, Paolo Ferri, Helen R. Middleton, and Ruth Ziethe. BepiColombo—Comprehensive exploration of Mercury: Mission overview and science goals. *Planet. Space Sci.*, 58(1-2):2–20, January 2010. doi: 10.1016/j.pss.2009.09.020.

S. Bingert and H. Peter. Intermittent heating in the solar corona employing a 3D MHD model. *A&A*, 530:A112, June 2011. doi: 10.1051/0004-6361/201016019.

K. Bocchialini, B. Grison, M. Menvielle, A. Chambodut, N. Cornilleau-Wehrlin, D. Fontaine, A. Marchaudon, M. Pick, F. Pitout, B. Schmieder, S. Régnier, and I. Zouganelis. Statistical Analysis of Solar Events Associated with Storm Sudden Commencements over One Year of Solar Maximum During Cycle 23: Propagation from the Sun to the Earth and Effects. *Sol. Phys.*, 293(5):75, April 2018. doi: 10.1007/s11207-018-1278-5.

David H. Brooks and Harry P. Warren. Establishing a connection between active region outflows and the solar wind: Abundance measurements with eis/hinode. *The Astrophysical Journal Letters*, 727(1):L13, 2011. URL http://stacks.iop.org/2041-8205/727/i=1/a=L13.

David H. Brooks, Ignacio Ugarte-Urra, and Harry P. Warren. Full-Sun observations for identifying the source of the slow solar wind. *Nature Communications*, 6:5947, January 2015. doi: 10.1038/ncomms6947.

David H. Brooks, Deborah Baker, Lidia van Driel-Gesztelyi, and Harry P. Warren. A Solar cycle correlation of coronal element abundances in Sun-as-a-star observations. *Nature Communications*, 8:183, August 2017. doi: 10.1038/s41467-017-00328-7.

E. Caffau, H.-G. Ludwig, M. Steffen, B. Freytag, and P. Bonifacio. Solar Chemical Abundances Determined with a CO5BOLD 3D Model Atmosphere. *Sol. Phys.*, 268:255–269, February 2011. doi: 10.1007/s11207-010-9541-4.

M. C. M. Cheung, P. Boerner, C. J. Schrijver, P. Testa, F. Chen, H. Peter, and A. Malanushenko. Thermal Diagnostics with the Atmospheric Imaging Assembly on board the Solar Dynamics Observatory: A Validated Method for Differential Emission Measure Inversions. *ApJ*, 807:143, July 2015. doi: 10.1088/0004-637X/807/2/143.

Gianni Corti, Giannina Poletto, Steve T. Suess, Ronald L. Moore, and Alphonse C. Sterling. Cool-Plasma Jets that Escape into the Outer Corona. *ApJ*, 659(2):1702–1712, April 2007. doi: 10.1086/512233.

I. J. D. Craig and J. C. Brown. Fundamental limitations of X-ray spectra as diagnostics of plasma temperature structure. *A&A*, 49:239–250, June 1976.

J. L. Culhane, L. K. Harra, A. M. James, K. Al-Janabi, L. J. Bradley, R. A. Chaudry, K. Rees, J. A. Tandy, P. Thomas, M. C. R. Whillock, B. Winter, G. A. Doschek, C. M. Korendyke, C. M. Brown, S. Myers, J. Mariska, J. Seely, J. Lang, B. J. Kent, B. M. Shaughnessy, P. R. Young, G. M. Simnett, C. M. Castelli, S. Mahmoud, H. Mapson-Menard, B. J. Probyn, R. J. Thomas, J. Davila, K. Dere, D. Windt, J. Shea, R. Hagood, R. Moye, H. Hara, T. Watanabe, K. Matsuzaki, T. Kosugi, V. Hansteen, and Ø. Wikstol. The EUV Imaging Spectrometer for Hinode. *Sol. Phys.*, pages 60–+, March 2007. doi: 10.1007/s01007-007-0293-1.

W. Curdt, P. Brekke, U. Feldman, K. Wilhelm, B. N. Dwivedi, U. Schühle, and P. Lemaire. The SUMER spectral atlas of solar-disk features. *A&A*, 375:591–613, August 2001. doi: 10.1051/0004-6361:20010364.

R. D'Amicis and R. Bruno. On the Origin of Highly Alfvénic Slow Solar Wind. *ApJ*, 805(1):84, May 2015. doi: 10.1088/0004-637X/805/1/84.

G. Del Zanna. *Extreme ultraviolet spectroscopy of the solar corona*. PhD thesis, University of Central Lancashire, UK, Jan 1999. URL http://www.damtp.cam.ac.uk/user/astro/gd232/research/thesis/gdz_phd_thesis.pdf.

G. Del Zanna. A revised radiometric calibration for the Hinode/EIS instrument. *A&A*, 555:A47, July 2013. doi: 10.1051/0004-6361/201220810.

G. Del Zanna, B. J. I. Bromage, H. E. Mason, and Robert F. Wimmer- Schweingruber. Elemental abundances of the low corona as derived from SOHO/CDS observations. In *Joint SOHO/ACE workshop "Solar and Galactic Composition"*, volume 598, page 59, November 2001.

G. Del Zanna, K. P. Dere, P. R. Young, E. Landi, and H. E. Mason. CHIANTI - An atomic database for emission lines. Version 8. *A&A*, 582:A56, Oct 2015. doi: 10.1051/0004-6361/201526827.

Giulio Del Zanna and Helen E. Mason. Solar UV and X-ray spectral diagnostics. *Living Reviews in Solar Physics*, 15:5, August 2018. doi: 10.1007/s41116-018-0015-3.

K. P. Dere, E. Landi, H. E. Mason, B. C. Monsignori Fossi, and P. R. Young. CHIANTI - an atomic database for emission lines. *A&AS*, 125, October 1997. doi: 10.1051/aas:1997368.

Bhola N. Dwivedi, Werner Curdt, and Klaus Wilhelm. Analysis of Extreme-Ultraviolet Off-Limb Spectra Obtained with SUMER/SOHO: Ne VI-Mg VI Emission Lines. *ApJ*, 517(1):516–525, May 1999. doi: 10.1086/307178.

B. Edlén. Die Deutung der Emissionslinien im Spektrum der Sonnenkorona. Mit 6 Abbildungen. *Zeitschrift für Astrophysik*, 22:30, 1943.

U. Feldman and K. G. Widing. Elemental Abundances in the Solar Upper Atmosphere Derived by Spectroscopic Means. *Space Sci. Rev.*, 107:665–720, July 2003. doi: 10.1023/A:1026103726147.

N. J. Fox, M. C. Velli, S. D. Bale, R. Decker, A. Driesman, R. A. Howard, J. C. Kasper, J. Kinnison, M. Kusterer, D. Lario, M. K. Lockwood, D. J. McComas, N. E. Raouafi, and A. Szabo. The Solar Probe Plus Mission: Humanity's First Visit to Our Star. *Space Sci. Rev.*, 204(1-4):7–48, December 2016. doi: 10.1007/s11214-015-0211-6.

J. Geiss. Diagnostics of corona by in-situ composition measurements at 1 AU. In E. Rolfe and B. Battrick, editors, *Future Missions in Solar, Heliospheric & Space Plasma Physics*, volume 235 of *ESA Special Publication*, June 1985.

L. Gizon, H. Schunker, C. S. Baldner, S. Basu, A. C. Birch, R. S. Bogart, D. C. Braun, R. Cameron, T. L. Duvall, S. M. Hanasoge, J. Jackiewicz, M. Roth, T. Stahn, M. J. Thompson, and S. Zharkov. Helioseismology of Sunspots: A Case Study of NOAA Region 9787. *Space Sci. Rev.*, 144(1-4):249–273, April 2009. doi: 10.1007/s11214-008-9466-5.

G. Gloeckler, J. Cain, F. M. Ipavich, E. O. Tums, P. Bedini, L. A. Fisk, T. H. Zurbuchen, P. Bochsler, J. Fischer, R. F. Wimmer-Schweingruber, J. Geiss, and R. Kallenbach. Investigation of the composition of solar and interstellar matter using solar wind and pickup ion measurements with SWICS and SWIMS on the ACE spacecraft. *Space Sci. Rev.*, 86:497–539, July 1998. doi: 10.1023/A:1005036131689.

N. Grevesse, M. Asplund, and A. J. Sauval. The solar chemical composition. *Space Science Reviews*, 130(1):105–114, Jun 2007. ISSN 1572-9672. doi: 10.1007/s11214-007-9173-7. URL https://doi.org/10.1007/s11214-007-9173-7.

N. Grevesse, P. Scott, M. Asplund, and A. J. Sauval. The elemental composition of the Sun. III. The heavy elements Cu to Th. *A&A*, 573:A27, January 2015. doi: 10.1051/0004-6361/201424111.

L. Griton and F. Pantellini. Magnetohydrodynamic simulations of a Uranus-at-equinox type rotating magnetosphere. *A&A*, 633:A87, January 2020. doi: 10.1051/0004-6361/201936604.

B. V. Gudiksen, M. Carlsson, V. H. Hansteen, W. Hayek, J. Leenaarts, and J. Martínez-Sykora. The stellar atmosphere simulation code Bifrost. Code description and validation. *A&A*, 531:A154, July 2011. doi: 10.1051/0004-6361/201116520.

C. Guennou, F. Auchère, E. Soubrié, K. Bocchialini, S. Parenti, and N. Barbey. On the Accuracy of the Differential Emission Measure Diagnostics of Solar Plasmas. Application to SDO/AIA. I. Isothermal Plasmas. *The Astrophysical Journal Supplement Series*, 203, December 2012a. doi: 10.1088/0067-0049/203/2/25.

C. Guennou, F. Auchère, E. Soubrié, K. Bocchialini, S. Parenti, and N. Barbey. On the Accuracy of the Differential Emission Measure Diagnostics of Solar Plasmas. Application to SDO/AIA. II. Multithermal Plasmas. *The Astrophysical Journal Supplement Series*, 203, December 2012b. doi: 10.1088/0067-0049/203/2/26.

C. Guennou, M. Hahn, and D. W. Savin. Relative abundance measurements in plumes and interplumes. *The Astrophysical Journal*, 807(2):145, 2015. URL http://stacks.iop.org/0004-637X/807/i=2/a=145.

Donald M. Hassler, Ingolf E. Dammasch, Philippe Lemaire, Pal Brekke, Werner Curdt, Helen E. Mason, Jean-Claude Vial, and Klaus Wilhelm. Solar Wind Outflow and the Chromospheric Magnetic Network. *Science*, 283:810, February 1999. doi: 10.1126/science.283.5403.810.

M. Janvier, P. Démoulin, and S. Dasso. Mean shape of interplanetary shocks deduced from in situ observations and its relation with interplanetary CMEs. *A&A*, 565:A99, May 2014. doi: 10.1051/0004-6361/201423450.

Eric Jones, Travis Oliphant, Pearu Peterson, et al. SciPy: Open source scientific tools for Python, 2001–. URL http://www.scipy.org/. [Online; accessed 2018-07-01].

P. G. Judge, Veronika Hubeny, and John C. Brown. Fundamental Limitations of Emission-Line Spectra as Diagnostics of Plasma Temperature and Density Structure. *ApJ*, 475:275–290, January 1997. doi: 10.1086/303511.

Vinay Kashyap and Jeremy J. Drake. Markov-chain monte carlo reconstruction of emission measure distributions: Application to solar extreme-ultraviolet spectra. *The Astrophysical Journal*, 503(1):450–466, aug 1998. doi: 10.1086/305964. URL https://doi.org/10.1086%2F305964.

R. A. Kopp and G. W. Pneuman. Magnetic reconnection in the corona and the loop prominence phenomenon. *Sol. Phys.*, 50(1):85–98, October 1976. doi: 10.1007/BF00206193.

T. Kosugi, K. Matsuzaki, T. Sakao, T. Shimizu, Y. Sone, S. Tachikawa, T. Hashimoto, K. Minesugi, A. Ohnishi, T. Yamada, S. Tsuneta, H. Hara, K. Ichimoto, Y. Suematsu, M. Shimojo, T. Watanabe, S. Shimada, J. M. Davis, L. D. Hill, J. K. Owens, A. M. Title, J. L. Culhane, L. K. Harra, G. A. Doschek, and L. Golub. The Hinode (Solar-B) Mission: An Overview. *Sol. Phys.*, 243:3–17, June 2007. doi: 10.1007/s11207-007-9014-6.

J. M. Laming. The FIP and Inverse FIP Effects in Solar and Stellar Coronae. *Living Reviews in Solar Physics*, 12:2, September 2015. doi: 10.1007/lrsp-2015-2.

J. Martin Laming. A Unified Picture of the First Ionization Potential and Inverse First Ionization Potential Effects. *ApJ*, 614(2):1063–1072, October 2004. doi: 10.1086/423780.

E. Landi, F. Reale, and P. Testa. Monte Carlo Markov chain DEM reconstruction of isothermal plasmas. *A&A*, 538, February 2012. doi: 10.1051/0004-6361/201117424.

J.R. Lemen, A.M. Title, D.J. Akin, P.F. Boerner, C. Chou, J.F. Drake, D.W. Duncan, C.G. Edwards, F.M. Friedlaender, G.F. Heyman, N.E. Hurlburt, N.L. Katz, G.D. Kushner, M. Levay, R.W. Lindgren, D.P. Mathur, E.L. McFeaters, S. Mitchell, R.A. Rehse, C.J. Schrijver, L.A. Springer, R.A. Stern, T.D. Tarbell, J.-P. Wuelser, C.J. Wolfson, C. Yanari, J.A. Bookbinder, P.N. Cheimets, D. Caldwell, E.E. Deluca, R. Gates, L. Golub, S. Park, W.A. Podgorski, R.I. Bush, P.H. Scherrer, M.A. Gummin, P. Smith, G. Auker, P. Jerram, P. Pool, R. Soufli, D.L. Windt, S. Beardsley, M. Clapp, J. Lang, and N. Waltham. The Atmospheric Imaging Assembly (AIA) on the Solar Dynamics Observatory (SDO). *Sol. Phys.*, 275:17–40, January 2012. doi: 10.1007/s11207-011-9776-8.

John T. Mariska. *The Solar Transition Region*. 1992.

E. Marsch, R. von Steiger, and P. Bochsler. Element fractionation by diffusion in the solar chromosphere. *A&A*, 301:261, September 1995.

D. J. McComas, S. J. Bame, B. L. Barraclough, W. C. Feldman, H. O. Funsten, J. T. Gosling, P. Riley, R. Skoug, A. Balogh, R. Forsyth, B. E. Goldstein, and M. Neuge-

bauer. Ulysses' return to the slow solar wind. *Geophys. Res. Lett.*, 25(1):1–4, January 1998. doi: 10.1029/97GL03444.

D. J. McComas, F. Allegrini, P. Bochsler, M. Bzowski, E. R. Christian, G. B. Crew, R. DeMajistre, H. Fahr, H. Fichtner, P. C. Frisch, H. O. Funsten, S. A. Fuselier, G. Gloeckler, M. Gruntman, J. Heerikhuisen, V. Izmodenov, P. Janzen, P. Knappenberger, S. Krimigis, H. Kucharek, M. Lee, G. Livadiotis, S. Livi, R. J. MacDowall, D. Mitchell, E. Möbius, T. Moore, N. V. Pogorelov, D. Reisenfeld, E. Roelof, L. Saul, N. A. Schwadron, P. W. Valek, R. Vanderspek, P. Wurz, and G. P. Zank. Global Observations of the Interstellar Interaction from the Interstellar Boundary Explorer (IBEX). *Science*, 326(5955):959, November 2009. doi: 10.1126/science.1180906.

R. Mitalas and K. R. Sills. On the Photon Diffusion Time Scale for the Sun. *ApJ*, 401: 759, December 1992. doi: 10.1086/172103.

Sargam M. Mulay, Durgesh Tripathi, Giulio Del Zanna, and Helen Mason. Multiwavelength study of 20 jets that emanate from the periphery of active regions. *A&A*, 589: A79, May 2016. doi: 10.1051/0004-6361/201527473.

D. Müller, R. G. Marsden, O. C. St. Cyr, and H. R. Gilbert. Solar Orbiter . Exploring the Sun-Heliosphere Connection. *Sol. Phys.*, 285(1-2):25–70, July 2013. doi: 10.1007/s11207-012-0085-7.

D. Müller, O.C. St. Cyr, I. Zouganelis, H.R. Gilbert, R. Marsden, T. Nieves-Chinchilla, and et al. The solar orbiter mission. science overview. *A&A*, 2020. doi: 10.1051/0004-6361/202038467. URL https://doi.org/10.1051/0004-6361/202038467.

J. A. Nelder and R. Mead. A simplex method for function minimization. *The Computer Journal*, 7(4):308–313, 1965. doi: 10.1093/comjnl/7.4.308. URL http://dx.doi.org/10.1093/comjnl/7.4.308.

Y. Ogawara, T. Takano, T. Kato, T. Kosugi, S. Tsuneta, T. Watanabe, I. Kondo, and Y. Uchida. The SOLAR-A Mission - An Overview. *Sol. Phys.*, 136(1):1–16, November 1991. doi: 10.1007/BF00151692.

S. Orsini, S. Livi, K. Torkar, S. Barabash, A. Milillo, P. Wurz, A. M. di Lellis, E. Kallio, and SERENA Team. SERENA: A suite of four instruments (ELENA, STROFIO, PICAM and MIPA) on board BepiColombo-MPO for particle detection in the Hermean environment. *Planet. Space Sci.*, 58(1-2):166–181, January 2010. doi: 10.1016/j.pss.2008.09.012.

C. J. Owen, R. Bruno, S. Livi, P. Louarn, K. Al Janabi, and et al. The solar orbiter solar wind analyser (swa) suite. *A&A*, 2020. doi: 10.1051/0004-6361/201937259. URL https://doi.org/10.1051/0004-6361/201937259.

Susanna Parenti, Giulio del Zanna, Antonino Petralia, Fabio Reale, Luca Teriaca, Paola Testa, and Helen E. Mason. Spectroscopy of Very Hot Plasma in Non-flaring Parts of a Solar Limb Active Region: Spatial and Temporal Properties. *ApJ*, 846(1):25, September 2017. doi: 10.3847/1538-4357/aa835f.

Susanna Parenti, Iulia Chifu, Giulio Del Zanna, Justin Edmondson, Alessandra Giunta, Viggo H. Hansteen, Aleida Higginson, J. Martin Laming, Susan T. Lepri, Benjamin J. Lynch, Yeimy J. Rivera, Rudolf von Steiger, Thomas Wiegelmann, Robert F. Wimmer-Schweingruber, and Natalia ZambranaPrado. Linking the sun to the heliosphere using composition data and modelling. *Space Sci. Rev.*, in prep.

Thies Peleikis, Martin Kruse, Lars Berger, and Robert Wimmer-Schweingruber. Origin of the solar wind: A novel approach to link in situ and remote observations. *Astronomy & Astrophysics*, 602:A24, jun 2017. ISSN 0004-6361. doi: 10.1051/0004-6361/201629727. URL http://www.aanda.org/10.1051/0004-6361/201629727.

W.D. Pesnell, B.J. Thompson, and P.C. Chamberlin. The Solar Dynamics Observatory (SDO). *Sol. Phys.*, 275:3–15, January 2012. doi: 10.1007/s11207-011-9841-3.

H. Peter. Velocity-dependent fractionation in the solar chromosphere. *A&A*, 312: L37–L40, August 1996.

K. Poppenhaeger, L. Ketzer, and M. Mallonn. X-ray irradiation and evaporation of the four young planets around V1298 Tau. *MNRAS*, May 2020. doi: 10.1093/mnras/staa1462.

S. R. Pottasch. On the Interpretation of the Solar Ultraviolet Emission Line Spectrum. *Space Science Reviews*, 3:816–855, December 1964a. doi: 10.1007/BF00177958.

S. R. Pottasch. On the chemical composition of the solar corona. *Monthly Notices of the Royal Astronomical Society*, 128:73, 1964b. doi: 10.1093/mnras/128.1.73.

N. E. Raouafi, S. Patsourakos, E. Pariat, P. R. Young, A. C. Sterling, A. Savcheva, M. Shimojo, F. Moreno-Insertis, C. R. DeVore, V. Archontis, T. Török, H. Mason, W. Curdt, K. Meyer, K. Dalmasse, and Y. Matsui. Solar Coronal Jets: Observations, Theory, and Modeling. *Space Sci. Rev.*, 201(1-4):1–53, November 2016. doi: 10.1007/s11214-016-0260-5.

Alexis Rouillard, Rui Pinto, A Vourlidas, Anik De Groof, W Thompson, Alessandro Bemporad, S Dolei, M Indurain, Eric Buchlin, Clementina Sasso, Daniele Spadaro, K. Dalmasse, J Hirzberger, I Zouganelis, A Strugarek, Sophie Brun, M Alexandre, David Berghmans, N. E. Raouafi, and Andrei Zhukov. Models and data analysis tools for the solar orbiter mission. *Astronomy and Astrophysics*, 10 2019.

J. L. R. Saba. Spectroscopic measurements of element abundances in the solar corona: Variations on the FIP theme. *Advances in Space Research*, 15, July 1995.

J. T. Schmelz, D. V. Reames, R. von Steiger, and S. Basu. Composition of the Solar Corona, Solar Wind, and Solar Energetic Particles. *ApJ*, 755:33, August 2012. doi: 10.1088/0004-637X/755/1/33.

N. A. Schwadron, L. A. Fisk, and T. H. Zurbuchen. Elemental Fractionation in the Slow Solar Wind. *ApJ*, 521(2):859–867, August 1999. doi: 10.1086/307575.

R. Schwenn. Solar Wind Sources and Their Variations Over the Solar Cycle. *Space Sci. Rev.*, 124(1-4):51–76, June 2006. doi: 10.1007/s11214-006-9099-5.

P. Scott, M. Asplund, N. Grevesse, M. Bergemann, and A. J. Sauval. The elemental composition of the Sun. II. The iron group elements Sc to Ni. *A&A*, 573:A26, January 2015a. doi: 10.1051/0004-6361/201424110.

P. Scott, N. Grevesse, M. Asplund, A. J. Sauval, K. Lind, Y. Takeda, R. Collet, R. Trampedach, and W. Hayek. The elemental composition of the Sun. I. The intermediate mass elements Na to Ca. *A&A*, 573:A25, January 2015b. doi: 10.1051/0004-6361/201424109.

Kazunari Shibata, Yoshinori Ishido, Loren W. Acton, Keith T. Strong, Tadashi Hirayama, Yutaka Uchida, Alan H. McAllister, Ryoji Matsumoto, Saku Tsuneta, Toshifumi Shimizu, Hirohisa Hara, Takashi Sakurai, Kiyoshi Ichimoto, Yohei Nishino, and Yoshiaki Ogawara. Observations of X-Ray Jets with the YOHKOH Soft X-Ray Telescope. *PASJ*, 44:L173–L179, October 1992.

Masumi Shimojo, Shizuyo Hashimoto, Kazunari Shibata, Tadashi Hirayama, Hugh S. Hudson, and Loren W. Acton. Statistical Study of Solar X-Ray Jets Observed with the YOHKOH Soft X-Ray Telescope. *PASJ*, 48:123–136, February 1996. doi: 10.1093/pasj/48.1.123.

D. Stansby, D. Baker, D. H. Brooks, and C. J. Owen. Directly comparing coronal and solar wind elemental fractionation. *A&A*, 640:A28, August 2020. doi: 10.1051/0004-6361/202038319.

E. C. Stone, A. M. Frandsen, R. A. Mewaldt, E. R. Christian, D. Margolies, J. F. Ormes, and F. Snow. The Advanced Composition Explorer. *Space Sci. Rev.*, 86:1–22, July 1998. doi: 10.1023/A:1005082526237.

Keith T. Strong, Karen Harvey, Tadashi Hirayama, Nariaki Nitta, Toshifumi Shimizu, and Saku Tsuneta. Observations of the Variability of Coronal Bright Points by the Soft X-Ray Telescope on YOHKOH. *PASJ*, 44:L161–L166, October 1992.

P. Swings. Edlén's Identification of the Coronal Lines with Forbidden Lines of Fe X, XI, XIII, XIV, XV; Ni XII, XIII, XV, XVI; Ca XII, XIII, XV; a X, XIV. *The Astrophysical Journal*, 98:116–128, July 1943. doi: 10.1086/144550.

Manuela Temmer, Julia K. Thalmann, Karin Dissauer, Astrid M. Veronig, Johannes Tschernitz, Jürgen Hinterreiter, and Luciano Rodriguez. On Flare-CME Characteristics from Sun to Earth Combining Remote-Sensing Image Data with In Situ Measurements Supported by Modeling. *Sol. Phys.*, 292(7):93, July 2017. doi: 10.1007/s11207-017-1112-5.

P. Testa, J. J. Drake, and E. Landi. Testing EUV/X-Ray Atomic Data for the Solar Dynamics Observatory. *ApJ*, 745:111, February 2012a. doi: 10.1088/0004-637X/745/2/111.

Paola Testa, Bart De Pontieu, Juan Martínez-Sykora, Viggo Hansteen, and Mats Carlsson. Investigating the Reliability of Coronal Emission Measure Distribution Diagnostics using Three-dimensional Radiative Magnetohydrodynamic Simulations. *ApJ*, 758, October 2012b. doi: 10.1088/0004-637X/758/1/54.

S. Tsuneta, L. Acton, M. Bruner, J. Lemen, W. Brown, R. Caravalho, R. Catura, S. Freeland, B. Jurcevich, M. Morrison, Y. Ogawara, T. Hirayama, and J. Owens. The Soft X-ray Telescope for the SOLAR-A mission. *Sol. Phys.*, 136(1):37–67, November 1991. doi: 10.1007/BF00151694.

R. von Steiger, J. Geiss, and G. Gloeckler. Composition of the Solar Wind. In J. R. Jokipii, C. P. Sonett, and M. S. Giampapa, editors, *Cosmic Winds and the Heliosphere*, page 581, 1997.

B. Vršnak, T. Žic, D. Vrbanec, M. Temmer, T. Rollett, C. Möstl, A. Veronig, J. Čalogović, M. Dumbović, S. Lulić, Y. J. Moon, and A. Shanmugaraju. Propagation of Interplanetary Coronal Mass Ejections: The Drag-Based Model. *Sol. Phys.*, 285(1-2):295–315, July 2013. doi: 10.1007/s11207-012-0035-4.

A. P. Walsh, T. S. Horbury, M. Maksimovic, C. J. Owen, J. Rodri-Pacheco, R. F. Wimmer-Schweingruber, I. Zouganelis, and et al. Coordination of the in situ payload of solar orbiter. *A&A*, 2020. doi: 10.1051/0004-6361/201936894. URL https://doi.org/10.1051/0004-6361/201936894.

K. G. Widing and U. Feldman. On the Rate of Abundance Modifications versus Time in Active Region Plasmas. *ApJ*, 555:426–434, July 2001. doi: 10.1086/321482.

P. R. Young and H. E. Mason. The Mg/Ne abundance ratio in a recently emerged flux region observed by CDS. *Sol. Phys.*, 175(2):523–539, October 1997. doi: 10.1023/A:1004936106427.

P. R. Young, G. Del Zanna, E. Landi, K. P. Dere, H. E. Mason, and M. Landini. CHIANTI-An Atomic Database for Emission Lines. VI. Proton Rates and Other Improvements. *ApJS*, 144(1):135–152, January 2003. doi: 10.1086/344365.

Natalia Zambrana Prado and Éric Buchlin. Measuring relative abundances in the solar corona with optimised linear combinations of spectral lines. *A&A*, 632:A20, Dec 2019. doi: 10.1051/0004-6361/201834735.

L. Zhao, T. H. Zurbuchen, and L. A. Fisk. Global distribution of the solar wind during solar cycle 23: ACE observations. *Geophys. Res. Lett.*, 36(14):L14104, July 2009. doi: 10.1029/2009GL039181.

université PARIS-SACLAY

ÉCOLE DOCTORALE
Ondes et matière
(EDOM)

Titre: Diagnostics spectroscopiques de la composition élémentaire de la couronne solaire

Mots clés: Spectroscopie UV, couronne solaire, analyse de données

Résumé: Un des objectifs principaux de la mission Solar Orbiter est d'établir un lien entre l'activité à la surface du Soleil et l'évolution de la couronne et de l'héliosphère interne. Le satellite emporte à cette fin une combinaison unique d'instruments permettant de faire tant des mesures in situ du plasma héliosphérique que des observations à distance du Soleil. Ces mesures nous permettront par exemple de déterminer la région source du vent solaire mesuré in-situ au niveau du satellite. Un outil essentiel pour établir un tel lien sont les mesures de composition. En effet, différentes structures solaires sont caractérisées par des abondances d'éléments chimiques différentes, en raison de l'effet FIP (premier potentient d'ionisation). Comparer les mesures de composition in situ et à distance, en lien avec la modélisation de l'effet FIP, nous permettra de déterminer les sources du plasma héliosphérique.

Lors de la thèse, j'ai développé une nouvelle méthode de mesure d'abondances relatives de la couronne solaire grâce à la spectroscopie UV, la Linear Combination Ratio (LCR) method. Cette méthode peut être peu coûteuse en télémétrie tout en restant fiable; elle se base sur des combinaisons linéaires optimisées de raies spectrales. Cette méthode a été testée sur des spectres synthétiques et sur des données d'observations spectroscopiques. Grâce à une approche bayésienne, j'ai ensuite développé une manière de déterminer les incertitudes liées aux mesures obtenues avec la méthode LCR.

Une des applications de la méthode fut de fournir des mesures de composition élémentaire fiables dans le cadre d'une collaboration dont le but est de trouver les caractéristiques du plasma et la région source d'un jet. La propagation dans la couronne et dans le milieu héliosphérique du jet a été ensuite modélisée pour déterminer sa composition in situ et s'il a atteint 1 UA.

L'ensemble des méthodes et des outils nécessaires au travail de la thèse ont été développés avec la mission Solar Orbiter (lancée en février 2020) en tête. J'ai modélisé le bruit que nous obtiendrons dans les observations de SPICE et j'ai fourni trois ensembles de raies spectrales qui pourront être utilisés pour faire des mesures de composition. Ces trois ensembles seront utilisés pour concevoir des observations optimales de SPICE pour la production de cartes d'abondance coronales.

Maison du doctorat de l'Université Paris-Saclay
2ème étage aile ouest, Ecole normale supérieure Paris-Saclay
4 avenue des Sciences,
91190 Gif sur Yvette, France

université PARIS-SACLAY

ÉCOLE DOCTORALE
Ondes et matière
(EDOM)

Title: Spectroscopic diagnostics of the elemental composition of the solar corona

Keywords: UV spectroscopy, solar corona, data analysis

Abstract: Linking solar activity on the surface and in the corona to the inner heliosphere is one of the main goals of Solar Orbiter. Its unique combination of in-situ and remote sensing instruments can be used to shed light on this difficult task by, e.g., determining the source region of the solar wind measured in-situ at the spacecraft position. A key element in this are data on the elemental composition. Indeed, different structures on the Sun have different abundances as a consequence of the FIP (First Ionization Potential) effect. Comparing in-situ and remote sensing composition data, coupled with modeling, will allow us to trace back the source of heliospheric plasma.

During my thesis, I developed a new method for measuring relative abundances of the solar corona using UV spectroscopy, the Linear Combination Ratio (LCR) method. This method can be telemetry efficient while remaining reliable; it is based on optimized linear combinations of spectral lines. This method has been tested on synthetic spectra and on spectroscopic observation data. Using a Bayesian approach, I then developed a way to determine the uncertainties related to the measurements obtained with the LCR method.

One of the applications of the method was to provide reliable measurements of elemental composition in the framework of a collaboration whose goal is to find the characteristics of the plasma and the source region of a jet, a jet whose propagation in the corona and in the heliospheric medium will then be modeled to determine its composition in situ and whether it has reached 1 AU.

All the methods and tools necessary for the thesis work have been developed with the Solar Orbiter mission (launched in February 2020) in mind. I have modeled the noise that we will obtain in the SPICE observations and I have provided three sets of spectral lines that could in principle be used to make composition measurements and that will be used to design optimal SPICE studies for abundance maps.

Maison du doctorat de l'Université Paris-Saclay
2ème étage aile ouest, Ecole normale supérieure Paris-Saclay
4 avenue des Sciences,
91190 Gif sur Yvette, France